

1 **Interpreting the Cratering Histories of Bennu, Ryugu,**
2 **and Other Spacecraft-Explored Asteroids**

3
4 W.F. Bottke¹, D. Vokrouhlický², R.-L. Ballouz³, O. S. Barnouin⁴, H. C. Connolly Jr.^{3, 5}, C.
5 Elder⁶, S. Marchi¹, T. J. McCoy⁷, P. Michel⁸, M. C. Nolan³, B. Rizk³, D. J. Scheeres⁹, S. R.
6 Schwartz³, K. J. Walsh¹, D. S. Lauretta³

7
8 ¹Southwest Research Institute, Boulder, CO, USA (bottke@boulder.swri.edu)

9 ²Institute of Astronomy, Charles University, V Holešovičkách 2, CZ-18000, Prague 8, Czech Republic

10 ³Lunar & Planetary Laboratory, University of Arizona, Tucson, AZ, USA

11 ⁴Johns Hopkins University Applied Physics Laboratory, Laurel, MD, USA

12 ⁵Dept. Geology, Rowan University, Glassboro, NJ, USA

13 ⁶Jet Propulsion Laboratory, Caltech, Pasadena, CA, USA

14 ⁷Smithsonian National Museum of Natural History, Washington, DC, USA

15 ⁸Observatoire de la Côte d'Azur, CNRS, Laboratoire Lagrange, Nice, France

16 ⁹Smead Department of Aerospace Engineering, University of Colorado, Boulder, CO, USA

17
18
19
20

Abstract

21
22
23
24
25
26
27
28
29
30
31
32
33
34
35
36
37
38
39
40
41
42

Asteroid crater retention ages have unknown accuracy because projectile-crater scaling laws are difficult to verify. At the same time, our knowledge of asteroid and crater size-frequency distributions has increased substantially over the past few decades. These advances make it possible to empirically derive asteroid crater scaling laws by fitting model asteroid size distributions to crater size distributions from asteroids observed by spacecraft. For $D > 10$ km diameter asteroids like Ceres, Vesta, Lutetia, Mathilde, Ida, Eros, and Gaspra, the best matches occur when the ratio of crater to projectile sizes is $f \sim 10$. The same scaling law applied to $0.3 < D < 2.5$ km near-Earth asteroids such as Bennu, Ryugu, Itokawa, and Toutatis yield intriguing yet perplexing results. When applied to the largest craters on these asteroids, we obtain crater retention ages of ~ 1 billion years for Bennu, Ryugu, and Itokawa and ~ 2.5 billion years for Toutatis. These ages agree with the estimated formation ages of their source families, and could suggest that the near-Earth asteroid population is dominated by bodies that avoided disruption during their traverse across the main asteroid belt. An alternative interpretation is that $f \gg 10$, which would make their crater retention ages much younger. If true, crater scaling laws need to change in a substantial way between $D > 10$ km asteroids, where $f \sim 10$, and $0.3 < D < 2.5$ km asteroids, where $f \gg 10$.

43 I. Introduction

44

45 The target of NASA’s asteroid sample return mission OSIRIS-REx (Origins, Spectral
46 Interpretation, Resource Identification, and Security–Regolith Explorer) is the near-Earth object
47 (NEO) (101995) Bennu. Bennu has a diameter $D_{\text{ast}} \sim 0.5$ km, a 4.4% mean albedo, and a spectral
48 signature consistent with a composition similar to CM- or CI-type carbonaceous chondrite
49 meteorites (e.g., Lauretta et al., 2019; Hamilton et al., 2019). The retrieval and study of primitive
50 asteroidal materials, whose provenance may go back to the earliest times of Solar System history,
51 may allow us to glean insights into the nature of planetesimal and planet formation. Another goal
52 of the OSIRIS-REx mission is to determine whether samples from Bennu can inform us about its
53 individual evolution, as well as that of its parent body. A critical part of this analysis will be to
54 place Bennu’s samples into a geologic, geochemical, and dynamical context, and that means
55 learning as much as we can about Bennu’s history from its physical and orbital properties. As part
56 of this work, our goal in this paper is to interpret Bennu’s cratering history and what it can tell us
57 about Bennu’s trek from its formation location, presumably in the main asteroid belt, to its current
58 orbit (e.g., Bottke et al., 2015b).

59 To set the stage for our work, we first describe what has been inferred about Bennu’s
60 collisional and dynamical history to date. A plausible evolution scenario is that Bennu was created
61 in the catastrophic disruption of a main belt parent body with $D_{\text{ast}} > 100$ –200 km approximately
62 1–2 billion years (Ga) ago (e.g., Campins et al., 2010; Walsh et al., 2013; Bottke et al., 2015b).
63 Using numerical simulations, and building on earlier work by Campins et al. (2010) and Walsh et
64 al. (2013), Bottke et al. (2015b) argued that Bennu most likely came from the low-albedo Eulalia
65 asteroid family (once called the Polana family) or New Polana asteroid family (the actual family
66 associated with (142) Polana). Both have low inclinations ($i \sim 2$ – 3°) and are located in the region
67 adjacent to Jupiter’s 3:1 mean motion resonance at ~ 2.5 au. The largest remnant of the Eulalia
68 family, likely (495) Eulalia, is located at semimajor axis $a = 2.487$ au, whereas the largest remnant
69 of the New Polana family, (142) Polana, is at $a = 2.42$ au. The estimated age of the Eulalia family
70 as derived by its dynamical evolution is 830 [+370, –100] Ma, whereas the age of New Polana is
71 thought to be 1400 [+150, –150] Ma, respectively. Using suites of numerical runs, Bottke et al.
72 (2015b) also showed that the New Polana was modestly favored as a source for Bennu over Eulalia
73 by a 70 [+8, –4]% to 30 [+4, –8]% margin, a result consistent with previous work (e.g., Campins
74 et al., 2010).

75 Bennu’s orbit and spin state is affected by the non-gravitational Yarkovsky and
76 Yarkovsky–O’Keefe–Radzievskii–Paddack (YORP) thermal effects (e.g., Rubincam, 2000;
77 Bottke et al., 2006a; Vokrouhlický et al., 2015; Chesley et al., 2014, Nolan et al., 2019,
78 Hergenrother et al., 2019). The former is a small force caused by the absorption of sunlight and
79 re-emission of this energy as infrared photons (heat). The recoil produces a thrust that leads to
80 steady changes in Bennu’s semimajor axis over long timescales. The latter is a thermal torque that,
81 complemented by a torque produced by scattered sunlight, modifies Bennu’s rotation rate and
82 obliquity. Modeling results indicate that the YORP effect readily modified Bennu’s spin axis to a

83 value approaching 180° , the same value it has today, and this allowed the Yarkovsky effect to
84 drive Benu inward across in the inner main belt (e.g., Bottke et al., 2015b). Additional
85 consequences of the YORP effect on Benu’s shape and surface are discussed below.

86 After spending most of its lifetime moving inward toward the Sun across the inner main
87 belt, Benu entered into the ν_6 secular resonance that defines the innermost boundary of the main
88 asteroid belt. From there, Benu was driven onto a high eccentricity (e) orbit where it underwent
89 encounters with the terrestrial planets. One such encounter, most likely with Earth, removed it
90 from the ν_6 resonance and placed it onto an $a < 2$ au orbit. At that point, planetary encounters and
91 smaller planetary resonances moved Benu onto its current Earth-like orbit with $(a, e, i) = (1.126$
92 au, $0.204, 6.035^\circ)$.

93 At some point along the way, Benu achieved an orbit low enough in eccentricity to
94 become collisionally decoupled from the main belt. At that point, sizable collisions on Benu
95 became far less common, with the NEO population smaller by roughly a factor of 1000 than the
96 main belt (e.g., Bottke et al., 1994, 2015a). Using the population of 682 asteroids with $D_{\text{ast}} \geq 50$
97 km defined by Farinella and Davis (1992), Bottke et al. (1996) found that NEOs were largely safe
98 from striking main belt bodies when their aphelion values $Q \leq 1.6$ au (e.g., Figs. 2 and 3 of Bottke
99 et al., 1996). According to dynamical runs from Bottke et al. (2015b), we found that the median
100 timescale to go from this boundary to Benu’s current (a, e, i) orbit was 2.6 Ma. Most test bodies
101 took < 20 Ma, though 3% of them managed to avoid it for 70–140 Ma.

102 Accordingly, if Benu came from the Eulalia or New Polana families, the time spent on an
103 orbit collisionally decoupled from the main belt was probably a tiny fraction of its entire lifetime.
104 Therefore, if Benu’s largest craters date back to those times, we can deduce that they were formed
105 by main belt projectiles. For reference, comparable arguments can be made for (162173) Ryugu,
106 the 1-km-diameter carbonaceous chondrite-like target of JAXA’s Hayabusa2 sample return
107 mission (Watanabe et al. 2019), which also likely came from the Eulalia or New Polana families
108 (Bottke et al. 2015b). The net number of impacts, though, may only be part of the story,
109 particularly if Benu has experienced frequent global crater erasure events.

110 The origin of Benu’s top-like shape may also tell us about its history. Benu is a
111 gravitational aggregate made of smaller components, what is often referred to as a “rubble-pile”
112 asteroid (e.g., Barnouin et al., 2019; Scheeres et al., 2019). Michel et al. (2020) argues that Benu’s
113 shape may have been derived from the re-accretion of fragments produced when the parent body
114 disrupted. Alternatively, it may have been spun up by YORP torques into a top-like shape (e.g.,
115 Walsh and Jacobson, 2015).

116 The YORP effect is also active today. An analysis of rotation data spanning the years 1999–
117 2019 indicate that Benu is currently spinning up at a rate of $(3.63 \pm 0.52) \times 10^{-6}$ deg day $^{-2}$
118 (Lauretta et al., 2019; Nolan et al. 2019; Hergenrother et al., 2019). If these kinds of accelerations
119 were common in the past, it seems reasonable that Benu’s shape has been heavily influenced by
120 YORP spin-up processes (Scheeres et al., 2019).

121 The invocation of the YORP spin-up mechanism to explain the shape of Benu and other
122 top-shaped asteroids, however, presents us with a paradox. If YORP is actively affecting the shape

123 and surface properties of small asteroids, creating a dynamic environment where landslides, mass
124 shedding events, and satellite formation are common (e.g., Barnouin et al., 2019; Scheeres et al.,
125 2019), one would expect to see few if any craters on that surface. Instead, an analysis of images
126 from Bennu indicates that it has several tens of craters of diameters $10 \text{ m} < D_{\text{crater}} < 150 \text{ m}$ (Walsh
127 et al., 2019). The largest craters are perhaps the most unexpected, because they are likely to be the
128 oldest and the least susceptible to erasure via impact-induced seismic shaking (e.g., Richardson et
129 al., 2005) or some other process. Comparable crater signatures were also found Ryugu (Sugita et
130 al., 2019). Like Bennu, Ryugu is top-shaped and shows evidence of mass movement. Even small
131 potato-shaped asteroids imaged by spacecraft, such (4179) Toutatis, and (25143) Itokawa, which
132 have mean diameters of ~ 2.5 and ~ 0.3 km, show a plethora of craters, with several having
133 diameters $D_{\text{crater}} > 100 \text{ m}$ (Jiang et al., 2015; Marchi et al., 2015).

134 When considered together, we are left with only a few options to explain the craters on
135 these small asteroids.

136 Option 1 is that the surfaces of many small asteroids are in fact ancient. This implies that
137 some process is regulating YORP-driven mass shedding. As discussed in Bottke et al. (2015b), a
138 possible mechanism for this would be “stochastic YORP”. Statler (2009) showed that modest
139 shape changes to asteroids, produced by a variety of processes (e.g., crater formation, changes to
140 asteroid rotational angular momentum by YORP), caused asteroids’ spin rates, but not their
141 obliquities, to undergo a random walk. This mechanism could slow down how often asteroids
142 achieve YORP-driven mass shedding events. In fact, Bottke et al. (2015b) found that some
143 stochastic YORP-like process was needed to explain the orbital distribution of asteroid families
144 such as Eulalia and New Polana. Another possible process with approximately the same effect
145 would be that small asteroids achieve YORP equilibrium states from time to time, where further
146 spin-up or spin-down is minimized until some shape change takes place (e.g., cratering, boulder
147 movement; Golubov and Scheeres, 2019).

148 Option 2 would be that Bennu’s surface, and the surfaces of Ryugu, Itokawa, and Toutatis,
149 are instead relatively young. The craters found on these worlds would then need to form at a much
150 higher rate than in Option 1. One way to achieve this would be to assume that the crater-projectile
151 scaling laws for small asteroids (hereafter crater scaling laws) allow relatively small impactors to
152 make large craters on the surface of these $D_{\text{ast}} < 2.5 \text{ km}$ bodies. The crater scaling laws for Option
153 1 would instead predict that larger asteroids are needed to make the observed craters.

154 At this time, we argue that the crater scaling laws for small asteroids are not well enough
155 constrained to rule out Options 1 or 2 for Bennu. If we treat crater scaling laws as a free parameter,
156 both scenarios appear to be consistent with the observational evidence we have for Bennu thus far,
157 namely that substantial YORP accelerations have been measured (Hergenrother et al., 2019; Nolan
158 et al., 2019), evidence for landslides exist (Barnouin et al., 2019), yet numerous craters have been
159 identified (Walsh et al., 2019). Comparable arguments can be made for Ryugu, Itokawa, and
160 Toutatis.

161 What is needed is additional evidence that can tip the balance between Options 1 and 2.
162 Ultimately, this comes down to finding a way to assess crater scaling laws for asteroids.

163
164
165
166
167
168
169
170
171
172
173
174
175
176
177
178
179
180
181
182
183
184
185
186
187
188
189
190
191
192
193
194
195
196
197
198
199
200

1.2 Methodology for our Crater Production Models

In this paper, we attempt to glean insights into crater scaling laws for small asteroids like Bennu, Ryugu, Itokawa, and Toutatis by first modeling and interpreting the crater records of large main belt asteroids observed by spacecraft (i.e., diameter $D_{ast} > 10$ km). Our procedure is to create a crater production model specific to each target asteroid. This involves the calculation of several components:

1. An assessment of the size-frequency distribution (SFD) of the main asteroid belt.
2. A crater scaling law that can transform asteroid impactors from Component 1 into craters on the target asteroid.
3. A calculation of the estimated collision probabilities and impact velocities between objects in the main belt population and the target asteroid.
4. The time that a stable surface on the target asteroid (or possibly the entire target asteroid itself) has been recording craters above a threshold crater diameter. This time will be referred to in the paper as the crater retention age or surface age.

Components 1 through 3 come from models whose accuracy depends on constraints and issues that are discussed in more detail below. Component 4, the crater retention age, is an output value that is calculated from a fit between the observed crater SFD found on the surface of the target asteroid and that target’s crater production model (e.g., Marchi et al. 2015).

For each crater production model, we intend to test a range of formulations for Components 1 and 2 against the crater SFD found regionally or globally on the target asteroid. This means that for every target asteroid discussed below, there will be an envelope of model main belt SFDs, possible crater scaling laws, and estimated crater retention ages that provide good fits to the data as measured using chi-squared tests. Our preference is to let these fits tell us which combinations of components yield superior results. At the completion of our runs, a confluence of similar components across many different target asteroids, each with different physical parameters, will allow us to predict those that nature prefers.

We purposely avoid terrains that have reached saturation equilibrium or have experienced substantial crater erasure. This leads us to exclude small craters below some threshold diameter from our analysis, with the definition of “small” defined on a case-by-case basis.

Our method also makes use of a number of assumptions that the reader should understand prior to a more in-depth discussion of the components within each crater production model:

- Assumption 1. The size and shape of main belt SFD has been in steady state for billions of years (within a factor of 2 or so) for projectile sizes that make observable craters on our target asteroids.

201 As discussed in a review by Bottke et al. (2015a), the main belt is the primary source for
202 the near-Earth asteroid population, which in turn provides impactors to the Moon and other
203 terrestrial planets. The evidence suggests the lunar impact flux over the last 3 to 3.5 Ga has been
204 fairly constant (within a factor of 2 or so) over this time (e.g., Ivanov et al., 2002; Marchi et al.,
205 2009; Hiesinger et al., 2012; but see also Robbins, 2014 and Mazrouei et al. 2019). This constraint
206 suggests that the main belt SFD for asteroids smaller than 10 km or so has largely been in a steady
207 state over this time (within a factor of 2). A strongly decaying main belt SFD would produce a
208 very different lunar impact rate.

209 Results of collisional evolution models also suggest that a steady state emerged in the main
210 belt SFD over the past several billion years (e.g., Bottke et al., 2015a). Asteroid families are
211 produced from time to time in the main belt, but their fragment SFDs are much smaller than the
212 main belt background SFD, at least for impactor sizes of interest in this paper. Once a family is
213 created, the SFD begins to undergo collisional evolution via the same asteroid disruption laws that
214 affect all other asteroids. This slowly grinds the new family's SFD into the same shape as the
215 background SFD. The consequence is that the main belt is constantly replenished by new breakup
216 events, but these events are rarely substantial enough to strongly modify the overall main belt SFD.

217 A potential test of Assumption 1 is to compare the crater retention ages of target asteroids
218 in asteroid families (or the surface of a target asteroid that can be connected with the origin of an
219 asteroid family) with independent measures of the family's age. If the surface of the target asteroid
220 in question has been recording impact craters from a time almost immediately after the family-
221 forming event, we would expect all of these age constraints to be similar to one another. Examples
222 of independent chronometers are (i) estimates of asteroid family age from models that track the
223 dynamical evolution of family members and (ii) shock degassing ages of meteorite samples that
224 were reset by impact heating caused by the family-forming event.

225 A concurrence of ages may represent potential evidence that the components applied in the
226 crater production model are reasonably accurate. We will explore this issue below using data from
227 the asteroids (4) Vesta, (243) Ida, and (951) Gaspra.

- 228
- 229 • Assumption 2. Most main belt asteroids with diameter $D_{\text{ast}} > 10$ km are on reasonably stable
230 orbits and commonly have been on such orbits for billions of years.

231

232 Although the main belt was potentially affected by giant planet migration early in its
233 history (e.g., Morbidelli et al. 2015; Vokrouhlický et al. 2016; Nesvorný et al. 2017), the
234 conclusion of these titanic dynamical events left the majority of $D_{\text{ast}} > 10$ km asteroids on fairly
235 stable orbits within the main belt region. From there, new $D_{\text{ast}} > 10$ km asteroids are created from
236 time to time by family-forming events, but they are unlikely to move far from the orbits on which
237 they were placed by the ejection event itself (e.g., Nesvorný et al. 2015).

238 Evidence for this comes in a variety of forms, ranging from the calculations of asteroid
239 proper elements for larger main belt asteroids, where dynamical stability can be demonstrated (e.g.,
240 Knežević et al. 2002), to billion-year integrations of the future dynamical evolution of $D_{\text{ast}} > 10$

241 km asteroids, where only a small fraction can escape the main belt (Nesvorný and Roig 2018). All
242 main belt asteroids undergo modest oscillations in their eccentricities and inclinations from secular
243 perturbations, but the forced components of this oscillation do not modify the free components.
244 These results indicate that nearly all of our large target asteroids have been in the same approximate
245 orbits for a long enough period of time that our crater production models can be based on their
246 present-day orbits.

247

- 248 • Assumption 3. Models are currently the best option to estimate the main belt SFD at sub-km
249 sizes.

250

251 As discussed in more detail below, existing asteroid surveys are unable to detect large
252 numbers of sub-km main belt asteroids, and those sub-km bodies that have been detected have to
253 be carefully debiased to avoid selection effects (i.e., for a given absolute magnitude, a survey will
254 find more high-albedo bodies than low-albedo bodies; Morbidelli et al. 2003; Maseiro et al. 2011).
255 To sidestep this limitation, we will use model main belt SFDs calculated from collision evolution
256 models as input for our crater production models. These model main belt SFDs are constructed to
257 fit existing main belt constraints (as we understand them) and therefore are probably the best we
258 can do with what is available at this time (e.g., Bottke et al. 2015a).

259 In the next few sections, we discuss our calculations of the components discussed above,
260 starting with Component 1, the predicted main belt SFD.

261

262 **2. Deriving a Model Main Belt Size Frequency Distribution (Component 1)**

263

264 **2.1 Understanding Collisional Evolution in the Main Belt**

265

266 To understand cratering on Bennu and other main belt asteroids, our first task is to assess
267 the main belt SFD (i.e., Component 1 from Sec. 1.2). This entails modeling how the main asteroid
268 belt undergoes collisional evolution.

269 First, although the main belt has a diverse population, nearly all asteroids have orbits that
270 cross one another, especially when secular perturbations are included (Bottke et al., 1994, 1996).
271 For example, using the 682 asteroids with $D_{\text{ast}} > 50$ km located between 2 and 3.2 au (Bottke et
272 al., 1994), we find 90% and 71% of individual asteroids cross 80% and 90% of the population,
273 respectively. Even those located along the innermost edge of the main belt near 2.2 au can still be
274 struck by nearly half of all main belt asteroids. Effectively, this means there are no hiding places.
275 Accordingly, one would expect the shape of the impactor size frequency distribution (SFD) hitting
276 most target bodies should largely represent an amalgam of the main belt SFD as a whole.

277 Second, collisional evolution models indicate that the main belt SFD is in a quasi-steady
278 state with a wave-like shape driven by the shape of the asteroid disruption law (e.g., Bottke et al.,
279 2005a,b, 2015a). Assuming all asteroids disrupt in a similar manner, which impact modeling work
280 suggests is a fairly reasonable approximation (e.g., Jutzi et al., 2013), simulations that produce the

281 best match with both the main belt SFD and constraints provided by asteroid families indicate that
282 asteroid disruption scaling laws undergo a transition between strength and gravity-scaling near D
283 ~ 0.2 km (Benz and Asphaug, 1999; Bottke et al., 2005a,b, 2015a). Asteroids near this transition
284 are relatively easy to disrupt, leading to a relative deficit of bodies with $D_{\text{ast}} \sim 0.1\text{--}0.5$ km. This
285 “valley” in the SFD leads to an overabundance, or a “peak”, of multi-kilometer bodies that would
286 be destroyed by such projectiles. Collisional models suggest this peak in the main belt SFD is near
287 $D_{\text{ast}} \sim 2\text{--}3$ km (e.g., O’Brien and Greenberg, 2003; reviewed in Bottke et al., 2015a).

288 As new-fragment SFDs are input into the asteroid belt from cratering or catastrophic
289 disruption events, the individual bodies in the SFD undergo collisional evolution. As this grinding
290 proceeds, for asteroids with $D_{\text{ast}} < 10$ km, the shapes of the new-fragment SFDs take on the same
291 wavy profile as the background main belt SFD over tens to hundreds of million years (e.g., Bottke
292 et al. 2005a,b, 2015a). In this manner, the wavy shape of main belt SFD can be considered to be in a
293 quasi-steady-state.

294 Collisions may not be the only mechanism affecting asteroid sizes and the wavy shape of
295 the main belt SFD. Asteroids with diameters smaller than a few km may also be affected by mass
296 shedding events produced by YORP thermal torques, the same processes that can modify the spin
297 vectors of small asteroids (e.g., Marzari et al., 2011; Jacobson et al., 2014). The influence of YORP
298 torques on asteroid sizes and the main belt SFD itself depends on the frequency of these mass
299 shedding events (e.g., Bottke et al. 2015a). Any changes to the main belt SFD produced by YORP
300 mass shedding, however, would drive new-fragment SFDs to the same shape as the background
301 main belt SFD.

302 The consequence is that the main belt SFD likely maintains a wavy profile that stays
303 relatively constant over billions of years. The absolute number of asteroids in the inner, central,
304 and outer main belt SFDs may change as asteroids are dynamically lost or as new families are
305 formed, but modeling work suggests that these effects rarely modify the overall shape of the main
306 belt SFD as a combined whole for very long.

307

308 **2.2 Motivation for Generating a Different Main Belt Size Distribution**

309

310 With that said, there are several reasons to consider different formulations of the main belt
311 SFD than those discussed in Bottke et al. (2005b). The changes we suggest below have been driven
312 by substantial progress in small body studies over the last two decades. In that time, a plethora of
313 new data has been obtained on the shape of the present-day NEO SFD from a wide variety of
314 surveys (e.g., the Catalina Sky Survey, Lincoln Near-Earth Asteroid Research (LINEAR),
315 Panoramic Survey Telescope and Rapid Response System (Pan-STARRS), Spacewatch, the Near-
316 Earth Object Wide-field Infrared Survey Explorer (NEOWISE) survey) and on asteroid crater
317 SFDs from various missions (see Secs 3 and 4). Both components – revised asteroid SFDs and
318 new asteroid crater SFDs – suggest the SFD presented in Bottke et al. (2005a,b) may be modestly
319 inaccurate for $D_{\text{ast}} < 1$ km.

320 For example, consider Figure 2 of Bottke et al. (2015a). It shows the cumulative model
321 main belt and NEO SFDs of Bottke et al. (2005b) against recent formulations of the NEO SFD by
322 Harris and D’Abramo (2015) (see also Stokes et al., 2017). We find the shape of Harris and
323 D’Abramo (2015) NEO SFD is fairly wavy, with substantial slope changes taking place near D_{ast}
324 $\sim 0.1\text{-}0.2$ km and 2-3 km. Bottke et al. (2005b) instead predicted that (i) the smaller of the two
325 inflection points should occur at $D_{\text{ast}} \sim 0.5$ km, (ii) that a less shallow slope should occur between
326 $0.1\text{-}0.2 < D_{\text{ast}} < 2\text{-}3$ km, and (iii) a less steep SFD should occur between $0.01 < D_{\text{ast}} < 0.1$ km.
327 While features (ii) and (iii) are somewhat dependent on the removal rates of small asteroids from
328 the main belt via the Yarkovsky effect, feature (i) cannot be explained in such a manner. In general,
329 an inflection point in the SFD of a source population should also be reflected in the daughter
330 population unless removal rates are highly variable.

331 From the crater perspective, Figure 4 of Marchi et al. (2015) showed a fit between the
332 Bottke et al. (2005b) formulation of the main belt SFD and the SFD of $0.1 < D_{\text{crater}} < 10$ km craters
333 found on or near Vesta’s Rheasilvia basin. It indicated that the Marchi et al. (2015) fit, while
334 tolerable, seemed to miss a key feature and inflection point between $0.7 < D_{\text{crater}} < 2$ km. A
335 mismatch in this size range would be consistent with Bottke et al. (2005b) predicting a key
336 inflection point is at $D_{\text{ast}} \sim 0.5$ km rather than 0.1-0.2 km.

337 There are several plausible ways we could modify the main belt SFD of Bottke et al.
338 (2005b) in the size range of interest:

- 339 1. Modifying the Yarkovsky depletion rates of asteroids from the main belt.
- 340 2. Allowing YORP-driven mass shedding to strongly affect the diameters of sub-km asteroids, as
341 suggested by Marzari et al. (2011) and Jacobson et al. (2014).
- 342 3. Modify the disruption scaling law for main belt asteroids.

343 We do not favor Scenario 1. Our tests using the Bottke et al. (2005b) model indicate that
344 to move the position of a main belt inflection point from 0.5 to 0.1-0.2 km, we would need to
345 assume (i) much larger Yarkovsky-driven removal rates than in Bottke et al. (2005b), which would
346 require even more main belt disruptions to keep the NEO population resupplied, and (ii) the
347 removal process has a strong size dependence between 0.1-0.2 and 0.5 km. Such changes produce
348 strong modifications to the model NEO SFD, giving it a shape inconsistent with the observed SFD.

349 We find Scenario 2 to be more intriguing, with modeling work from Marzari et al. (2011)
350 and Jacobson et al. (2014) suggesting YORP-driven mass shedding could be a major factor in
351 decreasing the diameter of sub-km bodies and thereby changing the main belt SFD. A potential
352 concern with this hypothesis, however, is that small asteroids observed by spacecraft have a
353 number of $D_{\text{crater}} > 0.1$ km craters (e.g., Bennu, Ryugu, Itokawa, Toutatis). If the Option 1
354 interpretation turns out to be true, and these asteroids have long crater retention ages for the largest
355 craters, it would rule out substantial YORP-driven mass shedding from these worlds. Note that
356 this does not mean that YORP is unimportant; it still provides an easy way to explain the
357 obliquities, top-like shapes, the existence of satellites, and the mass shedding events seen for many

358 small asteroids (e.g., Jewitt et al, 2015). Nevertheless, it would imply that YORP’s ability to
359 influence the main belt SFD may be more limited than suggested by these models.

360 In this paper, we focus our investigation on Scenario 3. Our work indicates that it is possible
361 to modify the asteroid disruption scaling law in a manner that yields a main belt SFD consistent
362 with constraints (e.g., shape of the observed main belt SFD, number of asteroid families, asteroid
363 craters, NEO SFD, laboratory impact experiments). With that said, though, Scenario 2 might still
364 be a major player in explaining the shape of the main belt SFD in this size range.

365

366 **2.3 Modeling Collisional Evolution in the Main Asteroid Belt**

367

368 **2.3.1 Collisional and dynamical depletion evolution code (CoDDEM)**

369

370 Most of the asteroids that hit Bennu-sized bodies are a few tens of meters or smaller in
371 diameter, well below the observational limit of the asteroid belt. For reference, current surveys
372 only able detect large numbers of $\sim 1\text{--}2$ km diameter bodies (e.g., Jedicke et al., 2002; Gladman et
373 al. 2009). Accordingly, the precise nature of the impactor population making craters on most
374 asteroids observed by spacecraft is not yet known. Progress is being made, with digital tracking
375 on ground-based telescopes having great potential (e.g., Heinze et al. 2019). New data may also
376 become available within the 2020’s from both the Large Synoptic Survey Telescope and space-
377 based infrared surveys like the Near-Earth Object Surveillance Mission (formally NEOCam). Still,
378 a full observational assessment of the sub-km main belt SFD will not be available for some time.

379 Until that time arrives, it makes sense to use collisional evolution models to estimate the
380 unknown nature of the small body main belt SFD. To this end, we model the main belt SFD using
381 the self-consistent one-dimensional collisional evolution code CoDDEM (Collisional and
382 Dynamical Depletion Evolution Model). Model details and the testing procedure for CoDDEM are
383 discussed in Bottke et al. (2005a,b; see also the review in Bottke et al., 2015a). Here we provide
384 the essentials needed to understand our new results.

385 We run CoDDEM by entering an initial main belt SFD where the population (N) has been
386 binned between $0.0001 \text{ km} < D < 1000 \text{ km}$ in logarithmic intervals $d\text{Log}D = 0.1$. The particles in
387 the bins are assumed to be spherical and are set to a bulk density of 2.7 g cm^{-3} , a common asteroid
388 bulk density value. CoDDEM then computes the time rate of change in the differential population
389 N per unit volume of space over a size range between diameter D and $D + dD$ (Dohnanyi, 1969;
390 Williams and Wetherill, 1994):

391

$$\frac{\partial N}{\partial t}(D, t) = -I_{DISRUPT} + I_{FRAG} - I_{DYN} \tag{1}$$

392

393 Here $I_{DISRUPT}$ is the net number of bodies that leave between D and $D + dD$ per unit time
394 from catastrophic disruptions. The collisional lifetime of a given target body in a bin in the current
395 main belt is computed using estimates of the intrinsic collision probability and mean velocities

396 between asteroids in the main belt, defined as $P_i = 2.86 \times 10^{-18} \text{ km}^{-2} \text{ yr}^{-1}$ and $V_{\text{imp}} = 5.3 \text{ km s}^{-1}$,
 397 respectively (Bottke et al., 1994; see also Bottke et al., 2015a).

398 The projectile capable of disrupting D_{target} is defined as d_{disrupt} :
 399

$$d_{\text{disrupt}} = \left(\frac{2Q_D^*}{V_{\text{imp}}^2} \right)^{1/3} D_{\text{target}} \quad (2)$$

400
 401 We set Q_D^* as the critical impact specific energy—the energy per unit target mass needed to disrupt
 402 the target and send 50% of its mass away at escape velocity. Our functions for Q_D^* at different
 403 asteroid sizes is tested below.

404 When a body breaks up, the results go into the I_{FRAG} parameter, which describes the number
 405 of bodies entering a given size bin per unit time that were produced by a given disruption event.
 406 CoDDEM uses fragment SFDs as discussed in Bottke et al. (2005a,b). The implication is that the
 407 destruction of large asteroids serves as a source to replenish the small body population via a
 408 “collisional cascade”.

409 The I_{DYN} parameter account for the number of bodies lost from a given size bin via
 410 dynamical processes, such as asteroids being removed by planetary perturbations or an object
 411 entering into a dynamical resonance via the Yarkovsky effect and escaping into planet-crossing
 412 orbits. This component is used to create our synthetic NEO SFD from the main belt population, as
 413 described in Bottke et al. (2005b).

414 In those runs, which we exactly duplicate in our new simulations, it was assumed that the
 415 primordial main belt contained on the order of 200 times the number of objects in the existing
 416 main belt, with the vast majority of the material ejected by interactions with planetary embryos
 417 within 1–2 Myr of the formation of the first solids. The dynamical removal mechanism used in
 418 Bottke et al. (2005b) may or may not end up reflecting reality, but that is not the salient point.
 419 Their model results instead serve as a reasonable proxy for scenarios where a large population of
 420 small bodies on planet-crossing orbits early in Solar System history batters the surviving main belt
 421 population. This may include the removal of primordial main belt asteroids onto planet-crossing
 422 orbits via interactions with migrating giant planets (e.g., Walsh et al., 2011) or early giant planet
 423 instabilities (e.g., Clement et al., 2018; Nesvorný et al., 2018). It is even possible the Bottke et al.
 424 (2005b) model results are fairly consistent with a primordial low-mass asteroid belt bombarded by
 425 populations introduced into the terrestrial planet region by planet formation processes. In terms of
 426 our model results, all these small body sources provide an additional source of early collisional
 427 evolution that sets the stage to explain the current main belt SFD.

428 429 **2.3.2 Initial conditions and model constraints for CoDDEM**

430
 431 The initial main belt population entered into CoDDEM is divided into two components that
 432 are tracked simultaneously: a small component of main belt asteroids that will survive the
 433 dynamical excitation event (N_{rem}) and a much larger component that will be excited and ejected

434 from the main belt (N_{dep}). Thus, our initial population is $N = N_{\text{rem}} + N_{\text{dep}}$. We can use this procedure
 435 because we know in advance the dynamical fate of each population via the dynamics simulations
 436 described in Bottke et al. (2015b). The two populations undergo comminution with themselves
 437 and with each other. When $N_{\text{dep}} = 0$, CoDDEM tracks the collisional and dynamical evolution of
 438 N_{rem} alone for the remaining simulation time.

439 The size and shape of our initial size distribution was determined by running different
 440 initial populations through CoDDEM-like codes, then testing the results against the constraints
 441 described in Sec. 4 (Bottke et al., 2005a,b). The size distribution that provided the best fit for N_{rem}
 442 followed the observed main belt for bodies with $D_{\text{ast}} > 200$ km, an incremental power law index
 443 of -4.5 for bodies with $110 < D_{\text{ast}} < 200$ km, and an incremental power law index of -1.2 for bodies
 444 with $D_{\text{ast}} < 110$ km (Bottke et al., 2005b). The initial shape of the N_{dep} population is always the
 445 same as N_{rem} , and its size is set to $N_{\text{dep}} = 200 N_{\text{rem}}$. Additional starting condition details can be
 446 found in Bottke et al. (2005a,b).

447 For constraints in Bottke et al. (2005b), our model main belt SFD at the end of 4.6 Ga of
 448 evolution had to reproduce the wavy-shaped main belt SFD for $D_{\text{ast}} > 1$ km. To determine its value,
 449 we converted the absolute magnitude H distribution of the main belt described by Jedicke et al.
 450 (2002), who combined observations of bright main belt asteroids with renormalized results taken
 451 from the Sloan Digital Sky Survey (Ivezić et al., 2001), into a size distribution. This was
 452 accomplished using the relationship (Fowler and Chilemi, 1992; Appendix in Pravec and Harris,
 453 2007):

$$454 \quad D_{\text{ast}}(\text{km}) = 1329 \times 10^{-H/5} p_v^{-1/2} \quad (3)$$

455 and a representative visual geometric albedo $p_v = 0.092$. The shape of the main belt SFD is shown
 456 as the large dots in Fig. 1. This SFD is in general agreement with the diameter-limited survey
 457 produced by WISE (Masiero et al., 2011), though their study is only complete in the outer main
 458 belt to asteroids larger than $D_{\text{ast}} > 5$ km. It also has had some success matching crater SFDs on
 459 asteroids (e.g., Marchi et al., 2015), though we will return to this issue below.

461
 462 INCLUDE FIGURE 1 HERE

463
 464 There have been many additional attempts to estimate the shape of the main belt SFD since
 465 Bottke et al. (2005a,b). We only mention a few of these examples here. Gladman et al. (2009) used
 466 a pencil beam survey of main belt asteroids and their likely colors to generate their SFD. Test fits
 467 of their SFD against crater SFDs on Vesta, however, have not been as successful as those derived
 468 from Bottke et al. (2005a,b) (Marchi et al., 2012a). Ryan et al. (2015) used the Spitzer space
 469 telescope to target known objects, find their diameters, and eventually generate a main belt SFD.
 470 Their results are similar to Gladman et al. (2009) in many respects. Accordingly, their SFD would
 471 likely also have similar problems matching constraints.

472 A potential issue with results from Gladman et al. (2009) and Ryan et al. (2015) is how
 473 their methods treat observational selection effects near the detection limit of main belt surveys. In

474 an absolute magnitude-limited survey, it is easier to detect high-albedo S-type asteroids than low-
 475 albedo C-type asteroids. This bias is pervasive through the catalog of known main belt objects.
 476 Studies employing this catalog may be overemphasizing S-types at the expense of C-types, which
 477 are numerous in the outer main belt. This effect was demonstrated by Masiero et al. (2011), who
 478 showed that nearly all of the main belt asteroids discovered by WISE were low-albedo. Up to that
 479 point, these bodies had been missed by telescopes looking in visual wavelengths.

480 Finally, a formulation of the main belt SFD by Minton et al. (2015) indicated that it should
 481 change slope close to $D_{\text{ast}} \sim 3.5$ km. We point out that this break is discordant with the shape of
 482 the inner main belt SFD determined by the diameter-limited WISE survey, which shows no change
 483 in slope at that size (Masiero et al., 2011). We also see no change in slope at $D_{\text{ast}} \sim 3.5$ km in the
 484 observed NEO SFD (Harris and D’Abramo 2015; Stokes et al., 2017) (Fig. 1); recall that the main
 485 belt is the primary source for NEOs, so a change in slope in the parent size distribution should
 486 probably be seen in the daughter size distribution as well.

487 A second set of constraints for Bottke et al. (2005a,b) was provided by asteroids families,
 488 particularly those that are potentially too large to be dispersed by the Yarkovsky effect over the
 489 age of the Solar System. Using hydrocode simulations from Durda et al. (2007) to estimate the
 490 amount of material in families located below the observational detection limit, Bottke et al. (2005a,
 491 b) suggested that ~ 20 families have been produced by the breakup of $D_{\text{ast}} > 100$ km asteroids over
 492 the past ~ 3.5 Ga. Although there have been recent attempts to update this number (e.g., see the
 493 review of this issue in Bottke et al., 2015a), we believe the distribution used by Bottke et al.
 494 (2005b) is still reasonable. Here we adopt the same constraint; we assume that the size distribution
 495 bins centered on $D_{\text{ast}} = 123.5, 155.5, 195.7, 246.4, 310.2,$ and 390.5 km experienced 5, 5, 5, 1, 1,
 496 and 1 breakups over the past 3.5 Ga, respectively. Our testing procedure also gives us some margin,
 497 so assuming that additional large asteroids disrupted over the past 3.5 Ga can be considered
 498 reasonable as well.

499 To quantify the fit between the model and observed population, we follow the methods
 500 described in Bottke et al. (2005a,b). Our first metric compares the shape of the model main belt
 501 SFD to a small envelope of values surrounding the observed main belt SFD (defined as N_{MB}):

$$502 \quad \psi_{\text{SFD}}^2 = \sum_D \left(\frac{N_{\text{REM}}(D) - N_{\text{MB}}(D)}{0.2 N_{\text{MB}}(D)} \right)^2 \quad (4)$$

503 We assume that our model is a good fit if lies within 20% of the observed main belt between 0.98
 504 km and 390.5 km (across 27 incremental bins) as defined by Bottke et al. (2005a) (see also Jedicke
 505 et al. 2002). As discussed in Bottke et al. (2005a), the 20% value was determined experimentally
 506 via comparisons between model results and data. Tests indicate that $\psi_{\text{SFD}}^2 < 20$ provides a
 507 reasonable match between model and data, with $\psi_{\text{SFD}}^2 < 10$ indicating a very good fit. The second
 508 metric is a standard χ^2 test where the fit between the model and observed families, χ_{FAM}^2 , is better
 509 than 2σ (i.e., probability $>5\%$).

511

512 2.3.3 Testing different asteroid disruption laws

513

514 In Bottke et al. (2005b), a range of Q_D^* functions were input into CoDDEM to see which
515 ones would most consistently reproduce (i) the observed main belt SFD, (ii) the number and
516 distribution of large asteroid families, and (iii) the approximate shape of the NEO SFD known at
517 that time (Sec 2.2). Given that collisional evolution is a stochastic process, each run, defined by a
518 set of initial conditions, was tested 100 times with different random seeds. Success or failure for
519 the trials was determined by our testing metrics (Sec. 2.2).

520 This method to compare our model results to observations has limitations, in that it assumes
521 that the actual main belt SFD is a byproduct of our most successful Q_D^* function. We do not know
522 whether this is true. It is possible that the actual main belt is an outlier compared to expectations
523 from a given collisional evolution scenario, with its properties coming from a number of stochastic
524 breakup events. For this paper, we will assume that is not the case, and that our main belt is average
525 in a statistical sense. We consider this approach to be reasonable given the available information
526 that exists on the main belt.

527 The best fit Q_D^* function in Bottke et al. (2005b) was similar to the one defined by the
528 hydrocode modeling results of Benz and Asphaug (1999) and the Q_D^* function Test #1 (hereafter
529 Q_D^* #1) shown in Fig. 2 (see also Table 1). It has the shape of a hyperbola, with the Q_D^* function
530 passing through a normalization point $(Q_{D_{LAB}}^*, D_{LAB}) = (1.5 \times 10^7 \text{ erg g}^{-1}, 8 \text{ cm})$, a value determined
531 using laboratory impact experiments (e.g., Durda et al., 1998) (Fig. 2). Other Q_D^* functions in the
532 literature have approximately the same convergence point for small target sizes, namely 10^7 erg
533 g^{-1} , with materials tested ranging from hard rocks to sand to small glass micro-spheres (e.g.,
534 Holsapple and Housen 2019).

535 The minimum Q_D^* value ($Q_{D_{min}}^*$) for Q_D^* #1 was found near $1.5 \times 10^6 \text{ erg g}^{-1}$ at $D_{min} = 0.2$
536 km. This combination yielded the model main belt SFD #1 shown in Fig. 1 (hereafter model SFD
537 #1). Model SFD #1 has an inflection point near $D_{ast} = 0.5 \text{ km}$, which we will show below is
538 modestly inconsistent with asteroid crater constraints.

539

540

PLACE FIGURE 2 HERE

541

542 For our work here, we choose to modify Q_D^* #1 enough to match our new constraints
543 (asteroid craters) without sacrificing the fit we had in Bottke et al. (2005b) to our original
544 constraints (shape of the main belt SFD at large sizes, prominent asteroid families). In practice,
545 this means changing the Q_D^* #1 hyperbola by (i) lowering $Q_{D_{min}}^*$ while keeping D_{min} near 0.2 km,
546 (ii) allowing the hyperbola to recover at larger sizes so it matches Q_D^* #1 as closely as possible for
547 $D_{ast} > 100 \text{ km}$, and (iii) forcing the hyperbola to pass through the normalization point
548 $(Q_{D_{LAB}}^*, D_{LAB})$. The change in (i) will help us disrupt additional bodies of size $0.1 < D_{ast} < 0.5 \text{ km}$,
549 which in turn will slide the inflection point shown in model SFD #1 near $D_{ast} = 0.5 \text{ km}$ to smaller
550 sizes.

551

Our new Q_D^* functions are defined by the following equations:

552

$$Q_D^*(R) = aR^\alpha + bR^\beta \quad (5)$$

553

$$a = \frac{Q_{D_{LAB}}^*}{R_{LAB}^\alpha} \frac{1}{1 - \frac{\alpha}{\beta} \left(\frac{R_{LAB}}{R_{min}}\right)^{\beta-\alpha}} \quad (6)$$

554

$$b = -\frac{\alpha}{\beta} a R_{min}^{\alpha-\beta} \quad (7)$$

555

556 Here $R = D / 2$ and $R_{LAB} = D_{LAB} / 2$. The parameters for our different Q_D^* functions, and their rate
557 of success against our main belt testing metrics in Sec. 2.2, are given in Table 1.

558

559

INSERT TABLE 1 HERE

560

561 We show our model SFDs #1–8 in Fig. 1. These test runs, corresponding to Q_D^* #1–8 (Fig
562 2; Table 1), indicate that decreasing $Q_{D_{min}}^*$ helps lower the critical inflection point to smaller
563 values. Moreover, in comparison to our baseline Q_D^* #1 and model SFD #1, we find that most of
564 our new Q_D^* functions produce a comparable fraction of successful outcomes, as displayed in Table
565 1. Only Q_D^* #7 and Q_D^* #8 produce less than satisfying outcomes. They cannot be ruled out, but
566 they should not be considered the top choices.

567

568 The power law slopes of the SFDs for $D_{ast} < 0.1$ km in Fig. 1 range from $q = -2.6$
569 cumulative for SFD #1 to $q = -2.7$ for SFD #8. These outcomes match predictions from O’Brien
570 and Greenberg (2003), who show that the slope of the Q_D^* function in the strength regime, defined
571 using the α parameter in Table 1, yield these approximate values for the α range shown there (i.e.,
572 -0.35 to -0.63). Our results also match observational constraints of the main belt SFD from Heinze
573 et al. (2019), who used Dark Energy Camera observations of main belt asteroids and digital
574 tracking methods to find a slope of $-2.575 < q < -2.825$.

575

576 The cumulative power law slope between the inflection points in Fig. 1, located between
577 $D_{ast} \sim 0.2$ – 0.5 km and 2 – 3 km, is shallower than the q values above. If we measure the slope for
578 all of our model SFDs between 0.5 km and 1.5 km, we find values that go from $q = -1.5$ for SFD
579 #1 to $q = -1.2$ for SFD #8. Heinze et al. (2019) report a cumulative slope in this range of $q = -1.31$
580 ± 0.01 , a value that matches Yoshida et al. (2007) ($q = -1.29 \pm 0.02$) but disagrees with Yoshida
581 et al. (2003) ($q = -1.2$). If we assume the preferred slope in this part of the main belt SFD is indeed
582 $q = -1.3$, the best match comes from SFD #6, with $q = -1.3$.

581

582 The intriguing matches between our SFDs and observational data are necessary but not
583 sufficient proof that our Q_D^* functions reflect reality. For example, Holsapple and Housen (2019)
584 point out that asteroid disruption scaling laws with α parameters more negative than -0.5 are
inconsistent with those inferred from materials tested to date. They instead argue that slopes in the

585 strength regime of -0.2 to -0.3 provide the best matches with scaling law theory. Taken at face
586 value, the best match to α parameters of -0.2 to -0.3 comes from our baseline Q_D^* #1, which yields
587 model SFD #1 within CoDDEM. As we will show below, however, this SFD does not reproduce
588 crater SFDs on many different asteroids as well as other choices.

589 There are different ways to potentially resolve this paradox beyond simply assuming that
590 our collisional evolution model is inaccurate. The first possibility would be that YORP-spin up is
591 indeed a major factor in the disruption of small asteroids (i.e., Scenario 2 from Sec. 2.2), and that
592 the demolition of small asteroids from this effect is needed in combination with Q_D^* #1 to get the
593 correct SFD. In other words, our steeper α parameter is compensating for the lack of YORP
594 disruption in our model.

595 A second possibility is that existing impact studies have not yet accounted for the unusual
596 material properties found on some small asteroids. For example, in Hayabusa2's Small Carry-on
597 Impactor (SCI) experiment, a 2.-kg copper plate was shot into the surface of the km-sized
598 carbonaceous chondrite-like asteroid Ryugu at 2 km/s, where it made a semi-circular crater with
599 a rim to rim diameter of 17.6 ± 0.7 m (Arakawa et al. 2020). This outcome was a surprise to many
600 impact modelers, in that Ryugu's surface acted like it had the same strength as cohesionless sand
601 upon impact (i.e., the crater formed in the gravity-dominated regime). Related studies suggest that
602 the boulders on Ryuyuu have estimated porosities as large as 55% (Grott et al. 2019). Put together,
603 these results may indicate that modified asteroid disruption laws are needed to accommodate how
604 carbonaceous chondrite-like asteroids with Ryugu-like properties behave in a disruption event.

605 The stage is now set to test our eight bounding model asteroid SFDs (Fig. 1) against
606 observed crater SFDs on asteroids observed by spacecraft.

607

608 **3. Crater Scaling Laws for Asteroids (Component 2)**

609

610 To determine the crater retention age of a given asteroid surface, we need to know the
611 crater scaling law that turns projectiles into craters. Typical crater scaling laws require a range of
612 projectile quantities (e.g., size, mass, impact velocity, impact angle, composition, internal
613 structure) and target quantities (e.g., target gravity, surface composition, structure and density,
614 target interior structure and density, effects of surface and internal porosity). Unfortunately, many
615 of these quantities are unknown for observed asteroids. Our ability to calibrate crater scaling laws
616 is also somewhat limited, given that most test data come from laboratory shot experiments,
617 conventional explosions, or nuclear bomb detonations. The energies involved in making observed
618 asteroid craters is typically orders of magnitude higher than the energies used to generate our crater
619 scaling law constraints, even those from nuclear blasts.

620

621

622

623

624

625 3.1 Holsapple and Housen crater scaling law

626

627 A common crater scaling law used in asteroid studies is similar to the Holsapple and
628 Housen (2007) formulation of the Pi-group scaling law (e.g., used by Marchi et al., 2015; see also
629 Tatsumi and Sugita, 2018):

630

$$D_t = kd \left[\frac{gd}{2V_p^2} \left(\frac{\rho}{\delta} \right)^{2\nu/\mu} + \left(\frac{Y}{\rho V_p^2} \right)^{(2+\mu)/2} \left(\frac{\rho}{\delta} \right)^{\nu(2+\mu)/\mu} \right]^{-\mu/(2+\mu)} \quad (8)$$

631 Here the transient crater diameter, defined by D_t , can be found using the impactor
632 properties (impactor diameter d , velocity perpendicular to the surface V_p , bulk density δ) together
633 with the target properties (density of target material ρ , strength of target material Y , surface gravity
634 g).

635 For planets and large asteroids, the input of surface gravity g into such crater scaling law
636 equations is straightforward; the combination of their largely spherical shapes and relatively slow
637 spin rates means accelerations across their surfaces are similar. For smaller asteroids, however, the
638 calculation of an effective surface gravity can be complicated by irregular shapes and centrifugal
639 forces.

640 As an example, consider (243) Ida. Its elongated shape ($59.8 \times 25.4 \times 18.6$ km) and rapid
641 spin period ($P = 4.63$ h) leads to a wide range of surface accelerations (0.3 to 1.1 cm s⁻²) (Thomas
642 et al. 1996). Therefore, when applying this scaling law to Ida, we follow the lead of Schmedemann
643 et al. (2014) and choose a single representative g value from this range (i.e., 0.7 cm s⁻²) as input
644 into our crater scaling laws. We follow suit for the other target asteroids in this paper, whose g
645 values, along with a corresponding reference, are given in Table 2.

646

647 PLACE TABLE 2 HERE

648

649 Additional parameters (k , ν , μ) account for the nature of the target terrain (i.e., whether it
650 is hard rock, cohesive soil, or porous material). Common parameters for hard rocks are $k = 0.93$, ν
651 $= 0.4$, $\mu = 0.55$, and for cohesive soils are $k = 1.03$, $\nu = 0.4$, $\mu = 0.41$ (e.g., Marchi et al., 2011,
652 2015).

653 The yield strength Y of different asteroid target materials is unknown, but we can bracket
654 possibilities using reference values, which range from lunar regolith ($Y = 1 \times 10^5$ dynes cm⁻²; $3 \times$
655 10^5 dynes cm⁻² at 1 m depth) to dry soil ($Y = 3 \times 10^6$ dynes cm⁻²) to dry desert alluvium ($Y = 7 \times$
656 10^5 dynes cm⁻²) to soft dry rock/hard soils ($Y = 1.3 \times 10^7$ dynes cm⁻²) to hard rocks and cold ice (Y
657 $= 1.5 \times 10^8$ dynes cm⁻²) (Holsapple and Housen, 2007). In general, when yield strength increases,
658 the craters formed from projectiles are smaller, which translates into an older surface for a given
659 crater SFD.

660 We also account for the collapse of the transient crater, such that the final crater size is
 661 $D_{crater} = \lambda D_t$. The value λ is ≥ 1 and it is usually determined empirically. A common value for λ is
 662 1.2, but smaller and larger values can also be found in the literature.

663 In terms of the final crater size, our tests show that larger values for λ can be counteracted
 664 by increasing Y ; the two trade off of one another. To keep things simple when asteroid parameters
 665 are largely unknown, and to limit the amount of interpretation needed for our results, we decided
 666 to apply $\lambda = 1.2$ and vary Y for our results. Hence, we assume that

$$667 \quad D_{crater} = 1.2 D_t \quad (9)$$

668 3.2 Ivanov crater scaling law

669 Another commonly used asteroid scaling law, reformulated from Schmidt and Housen
 670 (1987), comes from Ivanov et al. (2001) (see corrected version in Schmedemann et al., 2014). It
 671 has the form:

$$672 \quad \frac{D_t}{d(\delta/\rho)^{0.43} (V_p \sin \alpha)^{0.55}} = \frac{1.21}{[(D_{SG} + D_t)g]^{0.28}} \quad (10)$$

673 Here the yield strength and related parameters from Schmidt and Housen (1987) have been
 674 substituted in favor of a term that accounts for the strength-to-gravity transition on an asteroid
 675 surface (D_{SG}). For the work here, D_{SG} is defined relative to the lunar value, with $D_{SG} =$
 676 $D_{SG}^{Moon}(g_{Moon}/g)$, $D_{SG}^{Moon} = 0.3$ km, and $g_{Moon} = 1.62$ m s⁻² (Schmedemann et al., 2014). The
 677 input values for g and D_{SG} are given in Table 2. Note that with the exception of Ceres and Vesta,
 678 whose D_{SG} values are near 2 km, all asteroids listed in Table 2 have D_{SG} values larger than the
 679 craters examined in this paper.

680 The impact angle of the projectile, α , is assumed to be 45°, the most probable impact angle
 681 for projectiles hitting a surface (Shoemaker, 1962).

682 For large craters on big asteroids like Ceres, it is assumed in the Ivanov scaling law that
 683 the craters undergo collapse following the equation:

$$684 \quad D_{crater} = \frac{D_t^{\eta+1}}{D_{SC}^{\eta}} \quad (11)$$

685 Here $\eta = 0.15$ and D_{SC} is defined as the final rim diameter where simple craters transition into
 686 complex craters, which is assumed to be 10 km on Ceres (Hiesinger et al., 2016).

687 To verify that our coded versions of Eq. 10 and 11 function correctly for the results
 688 presented below, we reproduced the lunar and asteroid crater production functions shown in Fig.
 689 3 of Schmedemann et al. (2014) (i.e., their normalized crater production curves for the Moon,
 690
 691

692 Vesta (versions 3 and 4), Lutetia, Ida, and Gaspra). In this situation, input parameters were taken
693 from their paper.

694 A general comment should also be made about this scaling law versus the Holsapple and
695 Housen (2007) formulation. Both are based on the same general Pi-scaling theory and have a
696 similar heritage (e.g., Schmidt and Housen 1987). The difference is that the Holsapple and Housen
697 (2007) scaling law as shown in Eq. 8 has free parameters for the various strength parameters that
698 can be selected to match our best understanding of asteroid materials, whereas the Ivanov et al.
699 (2001) scaling law in Eq. 10 has those parameters built in. Presumably, one could select material
700 parameters for the Holsapple and Housen (2007) scaling law to make it closer to the Ivanov et al.
701 (2001) scaling law, and one could reformulate the Ivanov et al. (2001) scaling law to have
702 additional options as well. Therefore, the differences between the scaling laws are essentially
703 choices in how asteroids are predicted to behave.

704

705 **3.3. Empirical crater scaling law**

706

707 A new element in this work is to use empirical methods to derive the appropriate asteroid
708 scaling laws. Our method can be explained using two thought experiments.

709 For the first one, we consider a cumulative projectile and crater SFD defined as “broken”
710 power laws; two power laws with different slopes that either meet at an inflection point or join
711 each other over a slow bend (often called a “knee”). For this example, we assume the projectile
712 and crater SFDs are not congruent. If one wanted to glean insights into the nature of the crater
713 scaling law, the first thing to do would be to compare the inflection points or knees between the
714 projectile and crater SFDs. Assuming that the crater scaling law is not pathological, these locations
715 must correspond to one another. Their connection yields the relationship between the diameter of
716 the projectile D_{ast} and the diameter of the final crater D_{crater} . We call this ratio

717

$$f = \frac{D_{crater}}{D_{ast}} \quad (12)$$

718 and use it throughout the paper. It is the simplest possible crater scaling law. In this example, there
719 is only one value for f , but it can still be a powerful constraint if one desires to test crater scaling
720 laws and impact models.

721 For the second thought experiment, we again assume that we have broken power laws for
722 projectile and crater SFDs but that their shapes are congruent. By mapping the shape of the
723 projectile SFD onto the crater SFD, one can empirically obtain the crater scaling law f for all sizes
724 where data exist. In our idealized situation, no other information is needed; the myriad of crater
725 scaling parameters for projectile and target properties are folded into the factor f .

726 When we started this project, we assumed that the first thought experiment was most likely
727 to be applicable. As we show below, however, the projectile and crater SFDs used here are in fact
728 excellent matches to the second thought experiment. This suggests that we can calculate empirical
729 crater scaling laws for a wide range of crater sizes on different asteroids, provided their crater

730 SFDs have a knee or that we have sufficient alternative constraints to rule out other possible scaling
731 laws. As we will show, this method leads to powerful insights about the craters formed on different
732 asteroids.

733 Using f values, one could presumably constrain more sophisticated crater scaling laws that
734 describe how a given impact outcome is affected by different projectile and target quantities. The
735 difficulty would be to overcome the degeneracy between the variables, such as the tradeoff
736 between impact velocity, projectile size, etc. We do not perform such work here, but it would be
737 an interesting follow-up project.

738

739 **4. Collision Probabilities Between Target and Main Belt Asteroids (Component 3)**

740

741 Two additional components are needed to model the collisional evolution of individual
742 asteroids and interpret their crater histories: the intrinsic collision probabilities P_i and mean impact
743 velocities V_{imp} of our target asteroids against the main belt population. There are many published
744 formalisms to calculate these parameters that yield comparable results; a short list includes Öpik
745 (1951), Wetherill (1967), Kessler (1981), Farinella and Davis (1992), Bottke et al. (1994), Vedder
746 (1998), Manley et al. (1998), Dell’Oro et al. (2001), and Vokrouhlický et al. (2012). In this paper,
747 we use the methodology of Bottke et al. (1994).

748 For cratering events, the P_i parameter can be defined as the likelihood that a given projectile
749 will hit a target with a given cross-sectional area over a unit of time. In most such cases, the size
750 of the projectile is small enough to be ignored. For each pair of bodies, it can be considered to be
751 the product of two combined probabilities:

- 752 • The probability that two orbits, with orbit angles that uniformly precess on short timescales,
753 are close enough to one another that a collision can take place. It is the calculation of the
754 volume of the intersection space of the pair of orbits.
- 755 • The probability that both bodies will be at their mutual orbital crossing location at the same
756 time.

757 Our first task is to identify an appropriate projectile population that can hit our target
758 asteroids. At that point, we compute individual P_i and V_{imp} values for all of the bodies on crossing
759 orbits with the target. The (a, e, i) values of each pair are entered into the collision probability
760 code, with the integral examining and weighting all possible orientations of the orbits, defined by
761 their longitudes of apsides and nodes. This approximation is valid because secular perturbations
762 randomize these values over $\sim 10^4$ -yr timescales.

763 The most difficult part of this task is finding the appropriate impactor population. Consider
764 that most asteroid craters observed to date have been produced by projectiles smaller than the
765 observational limit of the main belt (roughly $D_{\text{ast}} \sim 1\text{--}2$ km). Moreover, the catalog of main belt
766 objects suffers from observational selection effects, particularly as one approaches the observation
767 limit. This makes it difficult to find a completely non-biased sample of main belt bodies for
768 collision probability calculations.

769 Most asteroids discovered to date have been found by surveys limited in absolute
770 magnitude (H). In general, for a given H value, it is easier to detect high-albedo S-type asteroids
771 than low-albedo C-type asteroids. Any studies employing this catalog need to worry about
772 overemphasizing S-types at the expense of C-types, particularly in the outer main belt where C-
773 types dominate the population.

774 To mitigate against these problems, it is common to use a complete population of main belt
775 asteroids as a statistical proxy for the population of smaller projectiles. For example, Bottke et al.
776 (1994) used 682 asteroids with $D_{\text{ast}} \geq 50$ km as defined by Farinella and Davis (1992) for their
777 collision probability calculations. The use of this sample is imperfect because family SFDs may
778 be important at small asteroid sizes, but it may be the most reasonable approximation that we can
779 make at this time, as we show below.

780 As a test, we also experimented with using the WISE diameter-limited catalog of main belt
781 objects. The WISE catalog is incomplete, yet using it leads to results that are interesting in many
782 ways. Masiero et al. (2011) showed that the ratio of the number of outer to inner main belt asteroids
783 becomes larger as one goes from $D_{\text{ast}} \geq 50$ km to $D_{\text{ast}} \geq 10$ km and then decreases again as one
784 goes to $D_{\text{ast}} \geq 5$ km. The latter effect occurs because the power law slope of the inner main belt
785 between $5 < D_{\text{ast}} < 10$ km is slightly steeper than that of the outer main belt over the same size
786 range. The outer main belt appears to become observationally incomplete for $D_{\text{ast}} < 5$ km, so we
787 perform no calculations beyond this point.

788 This change in population has little effect on the collision probabilities of asteroids residing
789 in the outer main belt, but it can be important for those in the inner main belt. As a demonstration
790 of this effect, we selected (951) Gaspra for a series of P_i tests against the WISE catalog.

791 Using Gaspra's proper (a , e , i) values of (2.20974 au, 0.1462, 4.77253°) (Table 3), we
792 calculated a mean P_i value for WISE asteroids on Gaspra-crossing orbits of 5.67, 5.15, and $5.39 \times$
793 10^{-18} km⁻² yr⁻¹ for bodies of $D_{\text{ast}} \geq 50$, 10, and 5 km. Little change is seen between the values.

794 If we then fold in the population not on crossing orbits, which is needed to derive the
795 approximate impact flux on Gaspra, the values change to 2.67, 1.74, and 2.11×10^{-18} km⁻² yr⁻¹,
796 with 252 out of 535, 2289 out of 6754, and 15044 out of 38437 on crossing orbits. The low value
797 for $D_{\text{ast}} > 10$ km is notable, in that it is only 65% of the value for $D_{\text{ast}} \geq 50$ km. The mean P_i value
798 then partially recovers for $D_{\text{ast}} \geq 5$ km because the inner main belt has a steeper SFD than the outer
799 main belt. If we assume this trend holds to $D_{\text{ast}} \geq 2$ km, it seems likely that the mean P_i value for
800 Gaspra will once again approach $D_{\text{ast}} \geq 50$ km. New work on debiasing the WISE asteroid catalog
801 is needed to confirm this hypothesis.

802

803

PLACE TABLE 3 HERE

804

805 Given these trends and considerations, we argue a reasonable compromise is to continue
806 to use the 682 asteroids with $D_{\text{ast}} \geq 50$ km discussed in Farinella and Davis (1992) and Bottke et
807 al. (1994) for our collision probability calculations of main belt bodies. Table 3 shows our results

808 for all main belt asteroids observed by spacecraft. We obtained their proper (a , e , i) elements from
809 the Asteroids Dynamic Site AstDyS, which is located at <http://hamilton.dm.unipi.it/astdys/>.

810

811 **5. Results for Main Belt Asteroids and Near-Earth Asteroids Larger than 10 Kilometers**

812

813 In this section, we examine the crater histories of the following asteroids observed by
814 spacecraft: Vesta, Ceres, Lutetia, Mathilde, Ida, and Gaspra, which are all main belt asteroids, and
815 Eros, a near-Earth asteroid. All have average diameters larger than 10 km. We start with main
816 belt asteroids that have the largest size range of craters and work down to Gaspra, the smallest
817 main belt asteroid in this list. Eros is actually larger than Gaspra, but we address it last to discuss
818 the prospective relationship between Eros, Gaspra, and the Flora asteroid family.

819 While this list is long, it is not comprehensive. We avoid modeling certain asteroid terrains
820 where crater saturation is prevalent, such as those on main belt asteroid Steins and the northern
821 hemisphere of Vesta (Marchi et al., 2015; see also Marchi et al., 2012a). To be cautious, we also
822 decided to bypass sub-km craters in the crater SFD of Ceres, in part because they were potentially
823 influenced by secondary cratering. Our analysis of those terrains is left for future work.

824 Finally, there are many proposed crater counts and crater retention ages for the asteroids
825 or features discussed below. We focus here on published craters and ages that are most germane
826 to testing our scaling laws and methods. For the interested reader who wants to know more,
827 including a list of references about the craters found on these worlds, a good place to start would
828 be to examine these papers: Chapman et al. (2002), O'Brien et al. (2006), Schmedemann et al.
829 (2014), and Marchi et al. (2015).

830

831 **5.1 Rheasilvia Basin on Vesta**

832

833 (4) Vesta is the second largest main belt asteroid. It is located in the middle of the inner
834 main belt with proper orbital elements of (a , e , i) = (2.36 au, 0.099, 6.4°). NASA's Dawn spacecraft
835 imaged its surface at varying spatial resolutions and verified that Vesta had differentiated into a
836 metallic core, silicate mantle, and basaltic crust. Some key physical parameters for Vesta include
837 dimensions of 572.6 km × 557.2 km × 446.4 km, a bulk density of 3.456 ± 0.035 g cm⁻³, and a
838 surface gravity of 0.25 m s⁻² (Russell et al., 2012).

839 Here we re-examine the superposed crater SFD on or near Vesta's Rheasilvia basin, a 500-
840 km-diameter impact structure that defines the shape of Vesta's southern hemisphere (e.g., Schenk
841 et al., 2012) (Fig 3). We choose this region for our modeling work for two reasons: Rheasilvia is
842 young enough that crater saturation is not an issue, and it is broad enough that it is covered by a
843 large range of crater diameters ($0.15 < D_{\text{crater}} < 35$ km; Marchi et al., 2015).

844

845

PLACE FIGURE 3 HERE

846

847 The craters identified and used here are located on Rheasilvia’s floor and ejecta blanket;
848 their properties are reported in Marchi et al. (2015) (see also Marchi et al., 2012a for earlier
849 counts). Their work indicated that a plausible age for Rheasilvia was ~ 1 Ga (Marchi et al., 2012a).
850 Model components that went into this age include (i) the main belt SFD described by Bottke et al.
851 (2005b) (SFD #1 in Fig. 1), (ii) an intrinsic collision probability between main belt asteroids and
852 Vesta of $P_i = 2.8 \times 10^{-18} \text{ km}^{-2} \text{ yr}^{-1}$, and (iii) the Holsapple and Housen (2007) scaling law for
853 cohesive soils ($Y = 2 \times 10^7 \text{ dynes cm}^{-2}$).

854 Their estimated crater retention age for Rheasilvia is comparable to the $^{40}\text{Ar}/^{39}\text{Ar}$ ages of
855 feldspar grains in the brecciated howardite Kapoeta, which were reset by a thermal event between
856 0.6 and 1.7 Ga ago (Lindsey et al., 2015). Lindsey et al. suggested that the source of the heating
857 event was the formation of Rheasilvia basin 1.4 ± 0.3 Ga ago. They also pointed out that this age
858 is similar to other $^{40}\text{Ar}/^{39}\text{Ar}$ ages found among the HED (howardite–eucrite–diogenite) meteorites.
859 A range of ages between 0.6 and 1.7 Ga seem plausible given these data.

860 Note that $^{40}\text{Ar}/^{39}\text{Ar}$ ages between 3.5–4.1 Ga have also been identified in eucrites. These
861 ages are older than the crater retention ages found for Rheasilvia by Schenk et al. (2012) and
862 Marchi et al. (2013b). Using their own crater counts, and comparing their model to craters with a
863 more limited dynamic range than those works, Schmedemann et al. (2014) argued that Rheasilvia
864 had a crater retention age that matched those ancient values. We will address this issue below.

865 The Rheasilvia basin–forming event also ejected numerous fragments onto escape
866 trajectories, and these bodies likely comprise Vesta’s color-, spectral- and albedo-distinctive
867 asteroid family (e.g., Parker et al., 2008; Nesvorný et al., 2015; Masiero et al., 2015). Using a
868 collisional evolution model, Bottke (2014) found that the Vesta family’s steep SFD, composed of
869 bodies of $D_{\text{ast}} < 10$ km, showed no indication of a change produced by collisional grinding. On
870 this basis, they estimated that the Vesta family has an 80% probability of being < 1 Ga old. The
871 orbital distribution of the family members, and how they have likely been influenced by the
872 Yarkovsky thermal forces, also suggests an age of ~ 1 Ga (Spoto et al. 2015), though we caution
873 that the high ejection velocity of the family members makes it difficult to precisely determine the
874 family’s dynamical age (e.g., Nesvorný et al., 2015).

875 The combined crater sets of Rheasilvia presented in Marchi et al. (2015) yield 48 craters
876 between $0.15 < D_{\text{crater}} < 35$ km (Fig. 4). Two knees are seen in the crater SFD: one near $D_{\text{crater}} \sim 2$
877 km and a second near $D_{\text{crater}} \sim 20$ km. The smaller of the two knees is likely related to the inflection
878 points seen between $0.2 < D_{\text{ast}} < 0.6$ km in the main belt SFDs shown in Fig. 1. The origin of the
879 larger knee will be discussed below.

880

881

882

PLACE FIGURE 4 HERE

883 5.1.1 Empirical scaling law derived by fitting model and observed crater SFDs (Rheasilvia)

884

885 To compare the shape of Vesta’s crater SFD to the impactor SFDs shown in Fig. 4, we
886 defined two parameters: (i) the crater scaling relationship factor $f = D_{\text{crater}} / D_{\text{ast}}$ and (ii) the age of

887 the Rheasilvia surface T_{ast} . The number of model craters forming per square kilometer on the
 888 surface of the asteroid, $N_{model-crater}(> D_{crater})$, as a function of time T_{ast} is given by the equation:
 889

$$N_{model-crater}(> D_{crater}) = \frac{P_i T_{ast} N_{model-ast}(> D_{ast})}{4\pi} \quad (13)$$

890 The number of model asteroids larger than a given size D_{ast} is given by $N_{model-ast}(> D_{ast})$, which
 891 can be found in Fig. 1.

892 The quality of the fit between the observed crater SFD on Rheasilvia (Fig. 4) and those
 893 modeled is defined using chi-squared methods:

$$\chi^2 = \sum_{i=1}^M \frac{(N_{model-crater}(> D_i) - N_{obs-crater}(> D_i))^2}{N_{obs-crater}(> D_i)} \quad (14)$$

895 Here $D_i = 1, \dots, M$, stands for the diameters of observed and model craters on a given asteroid
 896 surface. To obtain normalized χ^2 values, one should divide them by the value M , yielding the
 897 value we define here as χ^2_{norm} . In this case, there were 48 Rheasilvia craters, so $M = 48$ (Table
 898 4).

900 PLACE TABLE 4 HERE

902 By creating an array of (f, T_{ast}) values $5 < f < 25$, incremented by 0.1, and $0.01 < T_{ast} < 5$
 903 Ga, incremented by 0.01 Ga, we were able to test all plausible fits between model and observed
 904 crater data. These values also allow us to calculate confidence limits of 68% (1σ) and 95% (2σ)
 905 relative to our best fit case that can be used to estimate error bars.

906 An additional issue with fitting a model SFD to a crater SFD is that the smallest craters in
 907 $N(> D_{crater})$, which have the most data and the smallest error bars but also are closest to the
 908 observation limit, tend to dominate the χ^2 values. To mitigate against this effect, we multiplied
 909 the error bars of $N(> D_{crater})$ by a function γ that increases the error bars of the smaller craters
 910 according to:

$$\gamma = (w - 1) \frac{\log_{10} \left(\frac{D_{crater}}{D_{crater}^{max}} \right)}{\log_{10} \left(\frac{D_{crater}^{min}}{D_{crater}^{max}} \right)} + 1 \quad (15)$$

912 Here we set w to 3–5 for the asteroid craters in this paper, with D_{crater}^{min} and D_{crater}^{max} defined by the
 913 minimum and maximum crater sizes in a given set, respectively.

914 Using the P_i value in Table 3, our best fit case was found for SFD #5. It yielded $\chi^2_{MB} =$
 915 22.32 (Table 4). The SFDs #4–8 yielded values within 1σ of this best fit case. Our best fit f value

916 was 9.90, with 1σ of -1.40 and $+1.00$, whereas our best fit crater retention age for Rheasilvia was
917 $T_{\text{ast}} = 0.85$ Ga, with 1σ errors of -0.23 and $+0.24$ Ga (Table 5). The visual fit to the crater data in
918 Fig. 4 is good except for $D_{\text{crater}} > 20$ km craters. It is possible that the mismatch in this range stems
919 from small number statistics.

920

921

PLACE TABLE 5 HERE

922

923 **5.1.2 Housen and Holsapple crater scaling fit (Rheasilvia)**

924

925 We also examined how our main belt SFDs compared to Rheasilvia’s superposed craters
926 using the Holsapple and Housen (2007) formulation of the Pi-group crater scaling law (Eqs. 8 and
927 9). Hereafter we call this the HH crater scaling law.

928 Following the procedure used by Marchi et al. (2015), and applying his chosen parameters
929 for Eqs. 8 and 9, we assumed that Vesta’s surface could be treated like it had the same material
930 properties as cohesive soils ($k = 1.03$, $\nu = 0.4$, $\mu = 0.41$). We assumed that the projectile density
931 was 2.5 g cm^{-3} and Vesta’s surface density was 3.0 g cm^{-3} . After some trial and error, we found
932 that the lowest χ^2_{MB} values were generated from $Y = 2 \times 10^7 \text{ dynes cm}^{-2}$. We use this value for
933 all of the asteroids discussed below. The values of P_i and V_{imp} are found in Table 3.

934 Our best fit came from SFD #7, which yielded $\chi^2_{MA} = 19.34$ (Table 4). This value indicates
935 that our fit here is modestly superior to the empirical scaling law results in Sec. 3.1.1. The reason
936 is that their f value decreases for larger projectiles, allowing SFD #7 to match Rheasilvia’s craters
937 with $D_{\text{crater}} > 20$ km.

938 Our apparent success for large crater sizes, however, may be an issue. Existing numerical
939 hydrocode simulations indicate that the 500-km Rheasilvia basin formed from the impact of a 37-
940 to 60-km-diameter projectile (Jutzi et al., 2013; Ivanov and Melosh, 2013), which corresponds to
941 $f = 8.3\text{--}13.5$. These latter values are a good match to the f values predicted by our empirical scaling
942 law results (Fig. 4, Table 4).

943 If f indeed decreases substantially for large craters, as shown by the red curve in the inset
944 figure within Fig. 4, it would imply that much larger impactors—perhaps $D_{\text{ast}} > 100$ km—would
945 be needed to make Rheasilvia. We find this to be an unlikely scenario. We discuss this issue
946 further in Sec. 3.1.4.

947 Our best fit crater retention age for this set of parameters is $T_{\text{ast}} = 1.24 [-0.06, +0.06]$ Ga
948 (Table 5). This value matches the ages of Marchi et al. (2012a) and $^{40}\text{Ar}/^{39}\text{Ar}$ ages constraints from
949 Lindsey et al. (2015), but it is modestly older than the empirical fit results in Sec. 3.1.1. The reasons
950 are that (i) this scaling law yields f values that are consistently lower than the empirical main belt
951 best fit results of $f = 9.9$, which increases the surface age, and (ii) SFD #7 is shallower at small
952 asteroid sizes and therefore has fewer small projectiles; few projectiles mean older ages.

953

954

955

956 5.1.3 Ivanov crater scaling fit (Rheasilvia)

957

958 The last scaling law investigated was that from Ivanov et al. (2001) (Eqs. 10 and 11). Our
959 input parameters for this equation were given in Sec. 3.1.2. The best fit is from SFD #8, but χ^2_{IV}
960 in this case ended up as 70.51, a value indicative of a poor fit. The reason is that this scaling law
961 produces larger f values than the others tested for impactors of $D_{ast} < 0.1$ to 0.2 km. To fit the
962 smallest craters on Rheasilvia, the production function must substantially undershoot the craters
963 with $D_{crater} > 1$ km, as shown in Fig 4.

964 The best fit crater retention age is $T_{ast} = 0.37 [-0.02, +0.01]$ Ga, a value that is considerably
965 younger than the previous two test cases. It falls outside the $^{40}\text{Ar}/^{39}\text{Ar}$ age range of the Kapoeta
966 feldspar grains (0.6–1.7 Ga; Lindsey et al., 2015). It also does not match constraints on Vesta
967 family’s age from dynamics (Spoto et al. 2015) or collisional evolution (Bottke 2014). As before,
968 the reason has to do with the large f values applied here; if smaller projectiles make larger craters,
969 the surface has to be younger.

970 Our crater retention ages are different than those of Schmedemann et al. (2014), who use
971 the same scaling law to get 3.5 ± 0.1 Ga (though some surfaces have reported ages of 1.7–1.8 Ga;
972 see their Table 6). Only a minor portion of this difference can be attributed to their use of different
973 collision probabilities or impact velocities; their values are nearly the same as the ones we show
974 in Table 3. Similarly, in our tests of their work, we find that their derived main belt SFD is similar
975 to our SFD #8 in Fig. 1.

976 The main reason that Schmedemann et al. (2014) report a different crater retention age for
977 Rheasilvia than our work is that they focus on comparing their crater production function to craters
978 sizes between several kilometers and several tens of kilometers in diameter. As our Fig. 4 shows,
979 if one ignored all craters smaller than a few km, the best fit curve for the Ivanov scaling law would
980 shift to substantially higher values, with f values that are closer to those of the HH scaling law and
981 the empirical main belt fit scaling law. These effects would in turn yield substantially older crater
982 retention ages.

983 There may be valid reasons why one should ignore fitting a crater production function
984 model to small craters on a given surface, and it is possible that one can obtain reasonable results
985 by only looking at the largest craters on a surface. Nevertheless, where practicable, it is better to
986 compare a crater model across an entire size range of craters rather than a subset. For this reason,
987 we argue that this crater scaling law does not perform as well at modeling Vesta’s crater SFD in
988 Fig. 4 as the other choices.

989

990 5.1.4. What projectile sizes make the largest basins on Vesta?

991

992 In section 3.1.2, we asserted that we favor $f \sim 10$ to make the largest basins on Vesta. One
993 reason is that these values are consistent with hydrocode simulations, where the 500-km Rheasilvia
994 basin formed from the impact of a 37- to 60-km-diameter projectile (Jutzi et al., 2013; Ivanov and
995 Melosh, 2013). A second reason is that it matches f values predicted by our empirical scaling law

996 results (Fig. 4, Table 4). A third reason comes from the following calculation (see also Bottke et
997 al., 2015a).

998 The two largest basins on Vesta are Rheasilvia and Veneneia, with diameters of ~ 500 and
999 ~ 400 km, respectively. Veneneia is partially buried by Rheasilvia, so its estimated crater retention
1000 age is > 2 Ga (Schenk et al., 2012). Both formed after the emplacement of Vesta’s basaltic crust,
1001 which solidified within a few million years of Solar System formation (e.g., Hopkins et al., 2015).

1002 In the following calculation, we will assume these basins were produced by $f = 5$, which
1003 would require impacts from $D_{\text{ast}} \geq 90$ km and 100 km bodies, or $f = 10$, which would require
1004 impacts from $D_{\text{ast}} \geq 40$ km and 50 km bodies. If we assume the main belt had approximately the
1005 same population of large asteroids over the last 4.5 Gyr as it has today, such that we can use the
1006 SFD in Fig. 1 over this interval, the population of $D_{\text{ast}} \geq 40, 50, 90,$ and 100 km asteroids in the
1007 main belt is 860, 680, 270, 220, respectively. Using $P_i = 2.8 \times 10^{-18} \text{ km}^{-2} \text{ yr}^{-1}$, the probability that
1008 these projectiles will collide with Vesta over 4.5 Gyr is 0.79, 0.65, 0.30, 0.25 for $D_{\text{ast}} \geq 40, 50, 90,$
1009 and 100 km, respectively.

1010 Accordingly, for $f = 5$, the probability that both Rheasilvia and Veneneia will form on Vesta
1011 is $0.30 \times 0.25 = 7\%$, while for $f = 10$, the probability is $0.79 \times 0.65 = 51\%$. The latter value is 7
1012 times higher than the former. This does not mean the real scaling law must be $f \sim 10$, but it is fair
1013 to say that $f \sim 10$ makes it easier to match constraints.

1014

1015 **5.1.5 Summary (Rheasilvia)**

1016

1017 Our results for Vesta allow us to make some initial observations about how to interpret
1018 crater SFDs on asteroids.

1019

- 1020 • Results for the empirical fit and HH crater scaling laws indicate that the Rheasilvia formation
1021 event probably took place between ~ 0.6 Ga and ~ 1.3 Ga ago. This result is consistent with
1022 dynamical, collisional evolution, and meteorite constraints.
- 1023 • If an asteroid’s crater SFD has a knee near $D_{\text{crater}} \sim 2$ km, it indicates that an f value near ~ 10
1024 will allow it to match the main belt SFD. If f values are substantially smaller or larger than 10,
1025 one can only fit the small craters in the SFD at the expense of missing the larger ones, or vice
1026 versa.
- 1027 • Main belt asteroid SFDs that remain shallow between $\sim 0.2\text{--}0.3 < D_{\text{ast}} < 2\text{--}3$ km, results that
1028 are represented by SFDs #4 to #8 in Fig. 1, appear to be the most successful at matching
1029 constraints on Vesta.
- 1030 • Using the Holsapple and Housen (2007) formulation of the Pi-group scaling law, we find that
1031 input parameters for cohesive soils appear to allow us to best match observations.
- 1032 • Scaling laws that have f values substantially smaller than 10 for craters of $D_{\text{crater}} \sim 20$ km on
1033 Rheasilvia are needed to match data, but an extrapolation of this trend would make it difficult
1034 to produce Rheasilvia and Veneneia basins. Our interpretation is that this may make $f \sim 10$ a
1035 reasonable choice for all of the observed crater data on or near Rheasilvia basin.

1036
1037
1038
1039
1040
1041
1042
1043
1044
1045
1046
1047
1048
1049
1050
1051
1052
1053
1054
1055
1056
1057
1058
1059
1060
1061
1062
1063
1064
1065
1066
1067
1068
1069
1070
1071
1072
1073
1074
1075

5.2 Ceres’s Kerwan Basin

(1) Ceres, with dimensions of $965.2 \pm 2.0 \text{ km} \times 961.2 \pm 2.0 \text{ km} \times 891.2 \pm 2.0 \text{ km}$, is the largest asteroid in the main belt (Park et al. 2016). It is located near the outer edge of the central main belt, with proper orbital elements of $(a, e, i) = (2.77 \text{ au}, 0.12, 9.6^\circ)$. It is classified as a C-type asteroid, and observations from the DAWN spacecraft indicate that it is a volatile-rich rocky body. Studies based on DAWN spacecraft data have provided us with many critical parameters for Ceres, including its bulk density of $2.160 \pm 0.009 \text{ g cm}^{-3}$ and a surface gravity of 0.28 m s^{-2} (Russell et al., 2016). The mineralogy and geochemistry of Ceres, as constrained by Dawn observations, appear consistent with the bulk composition of CM/CI carbonaceous chondrites (McSween et al., 2018).

The nature of the craters on Ceres suggests that its surface may be intermediate in strength between that of Vesta and Rhea, the icy satellite of Saturn (Russell et al., 2016). The lack of crater relaxation observed for smaller craters, however, indicates that the crust may be deficient in ice, and could be a mechanically strong mixture of rock, carbonates or phyllosilicates, ice, and salt and/or clathrate hydrates (Fu et al., 2017). Curiously, Ceres is missing very large craters ($D_{\text{crater}} > 280 \text{ km}$) and is highly depleted in craters of diameter 100–150 km compared to expectations from the shape of the impacting main belt SFD (Marchi et al., 2016). Their absence could suggest the viscous relaxation of long-wavelength topography, perhaps via a subsurface zone of low-viscosity weakness (Fu et al., 2017).

To glean insights into the nature of Ceres’s crust, we examine the superposed crater SFD associated with Ceres’s Kerwan basin (Fig. 5). Geologic mapping work indicates that Kerwan is the oldest, largest (undisputed) impact crater on Ceres ($D_{\text{crater}} \sim 284 \text{ km}$) (Williams et al., 2017). The derived age of the basin depends on the superposed crater counts and the crater age model used (see the crater SFDs from Williams et al., 2017), but craters counted in the smooth unit of Kerwan, which range from approximately $5 < D_{\text{crater}} < 100 \text{ km}$, yield ages of $550 \pm 90 \text{ Ma}$ and $720 \pm 100 \text{ Ma}$ (Hiesinger et al., 2016). With that said, none of the model crater SFDs shown in Fig. 8 of Hiesinger et al. (2016) appear to reproduce the shape of the crater SFD, and the above ages seem to be determined by best fits to the largest craters.

PLACE FIGURE 5 HERE

Here we compare our model crater SFDs to craters counted by co-author S. Marchi. They have approximately the same crater SFD as Hiesinger et al. (2016). The crater counts have been slightly updated and are shown in Fig. 6. The observed inflection point in these crater SFD occurs near $D_{\text{crater}} \sim 20 \text{ km}$, approximately the same size as seen for Vesta’s Rheasilvia basin (Fig. 4). Accordingly, our prediction is that the Kerwan and Rheasilvia basins should have similar crater scaling laws.

1076 PLACE FIGURE 6 HERE

1077
1078 **5.2.1 Empirical scaling law derived by fitting model and observed crater SFDs (Kerwan)**
1079

1080 Using our empirical main belt fit method, and a P_i value of $3.455 \times 10^{-18} \text{ km}^{-2} \text{ yr}^{-1}$ (Table
1081 3), we found that our best fit comes from SFD #8, which yielded $\chi^2_{MB} = 2.84$ (Table 4). Both SFD
1082 #6 and 7 yielded values within 1σ of this best fit case.

1083 Our best fit f value was $8.20 [-1.40, +1.00]$, and our best fit crater retention age was $T_{ast} =$
1084 $0.91 [-0.17, +0.17]$. The latter value is modestly higher than those in Hiesinger et al. (2016), even
1085 though our collision probability P_i value is higher than their value of $2.84 \times 10^{-18} \text{ km}^{-2} \text{ yr}^{-1}$. The
1086 reason is because SFD #8 has fewer small bodies than the SFD in Bottke et al. (2005b) (SFD #1),
1087 which was used in their “asteroid-derived” model. Visually, the empirical main belt crater model
1088 reproduces the crater data reasonably well.

1089 If we were to choose a more probable main belt SFD according to Table 1, such as SFD
1090 #6, our best fit f value is $8.8 [-1.70, +1.20]$ and our best fit crater retention age T_{ast} is $0.86 [-0.18,$
1091 $+0.18]$ Ga.

1092
1093 **5.2.2 Housen and Holsapple crater scaling fit (Kerwan)**
1094

1095 Our comparison between model and data using the Holsapple and Housen (2007)
1096 formulation of the Pi-group scaling law also produced a reasonable match with Rheasilvia craters
1097 (Fig. 4). As with our Vesta runs, we assumed that Ceres’s surface had the strength of cohesive
1098 soils ($k = 1.03$, $\nu = 0.4$, $\mu = 0.41$), with projectile and target surface density set to 2.5 and 1.5 g cm^{-}
1099 3 , respectively. The yield strength was $Y = 2 \times 10^7 \text{ dynes cm}^{-2}$, and the values of P_i and V_{imp} are
1100 found in Table 3. This scaling law yielded a best fit using SFD #8, with $\chi^2_{MA} = 4.61$, modestly
1101 higher than the empirical main belt fit of $\chi^2_{MB} = 2.84$. Here the slight mismatch stems from the
1102 model crater SFD missing the craters with $D_{crater} > 40 \text{ km}$. The best fit crater retention age in this
1103 circumstance is $T_{ast} = 0.70 [-0.02, +0.03]$ Ga, fairly close to the main belt fit result (Table 5).
1104

1105
1106 **5.2.3 Ivanov scaling law fit (Kerwan)**
1107

1108 The fit using the Ivanov crater scaling law is only modestly better than the HH scaling law
1109 case, with $\chi^2_{IV} = 9.44$. The f values are larger here across the board than the other two scaling law
1110 cases, with crater sizes increasing substantially for $D_{ast} < 1 \text{ km}$. The best fit crater retention age
1111 here is $T_{ast} = 0.47 [-0.01, +0.02]$ Ga, younger than the previous two test cases (Table 5).

1112 With this said, there are indications in other Kerwan crater databases not investigated in
1113 this paper that the slope of the observed crater SFD indeed becomes substantially steeper for craters
1114 with $D_{ast} < 1 \text{ km}$, as predicted by the Ivanov scaling law (e.g., Williams et al., 2017). If so, the
1115 crater SFD on Kerwan is radically different than the one observed in Vesta’s Rheasilvia basin. It

1116 seems unlikely that the main belt SFD changed over the timescales in question, so this mismatch
1117 between Vesta and Ceres implies that the f value function is different for sub-kilometer craters on
1118 the two worlds.

1119 Finally, we note that it is plausible that the observed difference between sub-kilometer
1120 craters on Kerwan and Rheasilvia is because secondary craters are pervasive across Ceres for D_{crater}
1121 $< 2\text{--}3$ km.

1122

1123 **5.2.4 Summary (Kerwan)**

1124

1125 As with Rheasilvia basin on Vesta, the best fit matches in Table 4 come from the empirical
1126 main belt fit and the HH scaling law fit. As before, our results favor the high-number SFDs, with
1127 the best fit coming from #8, a value that is modestly disfavored from probability studies (Table 1).
1128 If we use a more probable SFD, such as SFD #6 (Table 1), the empirical scaling law $f \sim 9$, with
1129 errors that overlap with our $f \sim 10$ solution for Rheasilvia basin (Table 5). The age of Kerwan basin
1130 favored by our results is $\sim 0.8\text{--}0.9$ Ga.

1131

1132 **5.3 Lutetia’s Achaia Region**

1133

1134 (21) Lutetia is an M-type asteroid with dimensions of 121 ± 1 km \times 101 ± 1 km \times 75 ± 13
1135 km (Sierks et al. 2011) (Fig. 7). It is located in the inner main belt and has proper orbital elements
1136 of $(a, e, i) = (2.43$ au, 0.13, $2.1^\circ)$. The flyby of Lutetia by ESA’s Rosetta mission yielded a bulk
1137 density of 3.4 ± 0.3 g cm $^{-3}$ (Sierks et al. 2011). The composition of Lutetia is unknown, though it
1138 is thought to be related to enstatite chondrites or possibly the metal-rich CH carbonaceous
1139 chondrites (Coradini et al., 2011; Moyano-Camero et al., 2016).

1140

1141 PLACE FIGURE 7 HERE

1142

1143 Marchi et al. (2012b) examined craters on the oldest observed surface imaged by Rosetta,
1144 a flat and uniform region called Achaia (Fig. 7). The craters on Achaia range in size from $\sim 1 <$
1145 $D_{\text{crater}} < 50$ km (Fig. 8), a large enough dynamic range that they potentially sample both inflection
1146 points in our main belt SFD (Fig. 1).

1147

1148 PLACE FIGURE 8 HERE

1149

1150 **5.3.1 Empirical scaling law derived by fitting model and observed crater SFDs (Achaia)**

1151

1152 Our main belt fit method, combined with a P_i value of 3.763×10^{-18} km $^{-2}$ yr $^{-1}$ (Table 3),
1153 yields a best fit for SFD #7 with $\chi^2_{MB} = 1.97$ (Table 4). This value is the best of the three scaling
1154 laws tested for this case. The SFDs #3–#8 are also yield results within 1σ of this best fit case. Our
1155 best fit f value was 10.30 [–4.90, +3.60], similar to results from Vesta and Ceres. Our best fit crater

1156 retention age is $T_{\text{ast}} = 2.57 [-2.02, +1.64]$ Ga. This mean value is lower than the ~ 3.6 -Ga age
1157 estimate from Marchi et al. (2012b) but overlaps within errors. Visually, our main belt fit curve
1158 hits both inflection points and is a good visual fit to the data.

1159

1160 **5.3.2 Housen and Holsapple crater scaling fit (Achaia)**

1161

1162 Using the HH scaling law, the same yield strength as above, P_i and V_{imp} in Table 3, and
1163 projectile and target surface densities of 2.5 and 3.0 g cm⁻³, respectively, we obtain a comparable
1164 but slightly worse fit, with $\chi^2_{MA} = 2.24$ for SFD #7. Other SFDs within 1σ of the best fit case are
1165 #5–8. The crater retention age from this fit is $T_{\text{ast}} = 3.07 [-0.41, +0.41]$ Ga, similar to the age
1166 found in Marchi et al. (2012b). The empirical main belt and HH crater scaling curves in Fig. 8 are
1167 fairly similar to one another. The difference in age is produced by modest differences in the f
1168 function, with the HH scaling curve having f values between 7 and 9, somewhat lower than the
1169 main belt fit of $f \sim 10$.

1170

1171 **5.3.3 Ivanov scaling law fit (Achaia)**

1172

1173 The Ivanov scaling law produces the poorest fit, with $\chi^2_{IV} = 4.00$ for SFD #8 (Table 4).
1174 As with the Rheasilvia region on Vesta, the typical f value near 15 for smaller projectiles is higher
1175 than those found for either of the other two scaling laws (Fig. 8). This large value causes the best
1176 fit case to undershoot crater data between $3 < D_{\text{crater}} < 15$ km. It also leads to a younger age for
1177 Achaia, with $T_{\text{ast}} = 1.24 [-0.16, +0.16]$ Ga.

1178 Schmedemann et al. (2014) report that their fit to Lutetia's large and degraded craters,
1179 which have diameters between 2 and 25 km, yields a crater retention age of 3.5 ± 0.1 Ga. We
1180 suspect the difference in age between the two calculations is caused by our use of craters between
1181 1 and 3 km in Fig. 8. These craters drive our fit. If small craters were ignored, the best fit for the
1182 Ivanov scaling law curve would slide upward, which in turn would correspond to an older age.

1183

1184 **5.3.4 Summary (Achaia)**

1185

1186 In all three cases, the best fit matches seem to come from high-number SFDs, a common
1187 theme for all of the crater SFDs discussed up to this point. The main belt fit with $f \sim 10$ and the
1188 HH scaling law fit are preferred from the chi-squared metric over the Ivanov scaling law fit,
1189 probably because the latter's model crater SFD is lower than the observed crater data for middle-
1190 sized craters in Fig. 8. The crater retention age of the Achaia region has a wide range of possible
1191 ages, but a reasonable value for this terrain is ~ 3 –4 Ga.

1192

1193

1194

1195

1196 5.4 Mathilde

1197

1198 (253) Mathilde was the first C-type asteroid imaged by spacecraft (Fig. 9). NASA’s Near
1199 Earth Asteroid Rendezvous – Shoemaker mission (NEAR) flew by it in 1997 en route to Eros. It
1200 is located in the middle of the central main belt, with proper orbital elements of $(a, e, i) = (2.65 \text{ au},$
1201 $0.22, 6.5^\circ)$. Its physical dimensions are $66 \text{ km} \times 48 \text{ km} \times 46 \text{ km}$, and it has an estimated bulk
1202 density of $1.3 \pm 0.2 \text{ g cm}^{-3}$ (Veverka et al., 1997; 1999). Mathilde is not in an asteroid family
1203 (Nesvorný et al., 2015) and thus its surface may have borne witness to the early days of main belt
1204 history.

1205

1206 PLACE FIGURE 9 HERE

1207

1208 Mathilde, Bennu, and Ryugu are all C-complex bodies and thus are thought to have
1209 physical properties similar to carbonaceous chondrite meteorites. Accordingly, the crater history
1210 of Mathilde may provide us with the most direct insights into the crater scaling laws that govern
1211 Bennu and Ryugu. There are different schools of thought about how cratering should work on
1212 Mathilde. The flyby images that we have of Mathilde are dominated by its two largest craters,
1213 Ishikari (29.3 km) and Karoo (33.4 km) (Fig. 9). There appears to be little ejecta surrounding these
1214 craters (Veverka et al., 1999; Chapman et al., 1999). Housen et al. (1999) suggested that the
1215 apparent absence of deep ejecta blankets indicates the cratering process is dominated by the effects
1216 of porous materials. In such media, craters form more by compaction than excavation, and what
1217 little ejecta is produced goes back into the central cavity (Housen and Holsapple, 2003; Housen et
1218 al., 2018).

1219 The final size of the crater made into such a target, however, is unclear. Kinetic impact
1220 energy transfer can be inefficient in a porous target, and this may result in craters that are not much
1221 larger than those formed in targets with large yield stresses. Alternatively, the low strength nature
1222 of the target may make it easy for an impact to push material out of the way (e.g., comparable to
1223 impacts into sand targets; O’Brien et al., 2006), and this could result in a larger craters per
1224 projectile diameter than those found on S-type asteroids.

1225 To glean insights into this issue, it is useful to examine Mathilde’s crater SFD. Here we
1226 adopt the cumulative crater counts and errors of O’Brien et al. (2006), who converted their data
1227 from Fig. 3 of Chapman et al. (1999) (Fig. 10). Given how far crater counting tools have advanced
1228 in two decades, Mathilde would seem to be a ripe target for a re-examination.

1229 It is plausible that the Mathilde data are in saturation at smaller crater sizes, as suggested
1230 by Chapman et al. (1999), but the cumulative power law slope of the data for $D_{\text{crater}} < 2 \text{ km}$ is close
1231 to $q = -2.6$, like those of Rheasilvia basin (Vesta) and the Achaia region (Lutetia) (Figs. 4, 8). Our
1232 expectation is that a crater SFD in saturation would instead have a cumulative slope of $q = -2$ (e.g.,
1233 Melosh 1989), a value that is possible within error bars but does not appear to be the true solution.
1234 Here we will assume that Mathilde’s observed crater SFD is not in saturation.

1235

1236 PLACE FIGURE 10 HERE
1237

1238 A relatively recent calculation of the crater retention age of Mathilde was made by O'Brien
1239 et al. (2006). They made the following assumptions: (i) the intrinsic collision probability P_i for
1240 Mathilde was $2.86 \times 10^{-18} \text{ km}^{-2} \text{ yr}^{-1}$ (a factor of 0.77 lower than our value from Table 3), (ii) the
1241 main belt SFD followed the estimate made by O'Brien and Greenberg (2005), (iii) Mathilde's
1242 craters could be produced by the Pi-group crater scaling relationship, provided that the target acted
1243 like loose sand, and (iv) sandblasting by small impactors, a potential crater erasure mechanism,
1244 was active on Mathilde (e.g., Greenberg et al. 1994; 1996). Their crater scaling law for Mathilde
1245 is shown in their Fig. 2. For their impactors of 0.1 to 1 km diameter, their value for f was
1246 approximately 20–40.

1247 O'Brien et al. (2006) report that the population of km-scale and smaller craters becomes
1248 saturated at a constant level near 1 Ga ago, but that the best crater retention age for the large craters
1249 is ~ 4 Ga. We will instead assume below that Mathilde's crater SFD follows a production
1250 population and that crater erasure mechanisms are not needed to explain observations.
1251

1252 **5.4.1 Empirical scaling law derived by fitting model and observed crater SFDs (Mathilde)**

1253

1254 Assuming $P_i = 3.723 \times 10^{-18} \text{ km}^{-2} \text{ yr}^{-1}$ (Table 3), we obtain a best fit for SFD #2 with χ^2_{MB}
1255 = 2.67 (Table 4). We find that SFDs #1–6 all have χ^2_{MB} within 1σ of this best fit case. Our best
1256 fit value for f is 10.00 [−3.40, +1.90], and best fit crater retention age was $T_{ast} = 3.70$ [−1.30, +1.52].
1257 If we were to adopt SFD #6, these values change to $f = 12.2$ [−2.0, +2.3], with T_{ast} becoming 3.61
1258 [−1.31, +0.94] Ga. Here the smaller number of projectiles in SFD #6 is compensated by having
1259 each projectile make a modestly larger crater.
1260

1261 **5.4.2. Housen and Holsapple crater scaling fit (Mathilde)**

1262

1263 The parameters listed in Holsapple and Housen (2007) for the highly porous case are
1264 essentially the same as those used for cohesive soils. It is argued in their paper that their
1265 experimental craters were governed predominantly by some compressive strength, so strength-
1266 scaled laws would apply. Accordingly, their scaling is almost identical to those used for other
1267 asteroids and assumes that compressive strength is the relevant measure.

1268 Assuming a target and projectile density of 1.3 g cm^{-3} , we obtain a best fit of $\chi^2_{MA} = 2.60$
1269 for SFD #4. The f value of the scaling law is close to $f = 12$ for the projectile sizes used here (Fig.
1270 10). The SFDs #1–#5 are 1σ of the best fit case, and they yield ages of $2.2 < T_{ast} < 3.4$ Ga. If we
1271 include error bars, the age range expands to $1.8 < T_{ast} < 4$ Ga.
1272
1273
1274
1275

1276 **5.4.3. Ivanov scaling law fit (Mathilde)**

1277

1278 The Ivanov scaling law leads to a best fit of $\chi^2_{IV} = 4.98$ for SFD #8 (Table 4). Its f values
1279 are substantially higher than the other two cases, and they yield a crater retention age of $T_{\text{ast}} = 0.85$
1280 $[-0.15, +0.15]$ Ga. This outcome shows the implications of having projectiles make much larger
1281 craters on Mathilde relative to other scaling laws; the surface age of the body becomes young
1282 enough that one needs to invoke a special event to explain why the surface is young. As stated
1283 above, Mathilde has no asteroid family, and its big craters formed apparently without damaging
1284 one another. This makes it more difficult to argue that impacts have reset the surface relatively
1285 recently (i.e., over the past billion years).

1286

1287 **5.4.4. Summary (Mathilde)**

1288

1289 The crater SFD for Mathilde is murky enough that it is difficult to identify which fits are
1290 best. Until stronger evidence becomes available, it seems reasonable to adopt the simplest
1291 solutions.

1292 Accordingly, if we apply a high-number SFD to our crater model, one that also provides a
1293 good fit to the other asteroid terrains investigated so far (i.e., SFD #6, which for Mathilde yields
1294 results that are within 1σ of the best case fit for both the empirical main belt fit case and the HH
1295 scaling law case), our results suggest that $f \sim 10\text{--}12$ provides a good solution to the entire crater
1296 SFD. In turn, those results suggest that Mathilde's crater retention ages go back to the earliest
1297 days of Solar System history. Arguments in favor of this interpretation come from Mathilde's lack
1298 of an asteroid family. Some might argue that the porous nature of C-type asteroids makes them
1299 less likely to produce families, but numerous C-type families have been identified across the main
1300 belt (e.g., Nesvorný et al. 2015; Masiero et al. 2015), including those likely to have produced
1301 Bennu and Ryugu (Bottke et al. 2015b).

1302 If our interpretation is valid, it obviates the need for crater erasure mechanisms that affect
1303 the observed craters smaller than several km (e.g., O'Brien et al. 2006). It would also argue that
1304 projectiles hitting carbonaceous chondrite-like materials do not necessarily lead to substantially
1305 larger craters than those made on other asteroids (e.g., Ceres craters; see Sec. 3.2). If Mathilde's
1306 crater scaling laws produced $f \gg 10$, it would lead to a crater retention age for Mathilde that
1307 would be younger than ~ 1 Ga. Given the lack of evidence on Mathilde for any surface reset event,
1308 we argue that a young crater retention age for Mathilde seems unlikely.

1309

1310 **5.5 Ida**

1311

1312 The second asteroid observed by the Galileo spacecraft was (243) Ida, an S-type asteroid
1313 that is also a member of the Koronis asteroid family (Fig. 11). It is located in the outer main belt,
1314 with proper orbital elements of $(a, e, i) = (2.86 \text{ au}, 0.05, 2.1^\circ)$. Its physical dimensions are 59.8
1315 $\text{km} \times 25.4 \text{ km} \times 18.6 \text{ km}$ (Belton et al., 1996). The best estimate of Ida's bulk density comes from

1316 Petit et al. (1997), who used the orbit of Ida’s satellite Dactyl to obtain a value of $2.6 \pm 0.5 \text{ g cm}^{-3}$.
1317

1318

1319

PLACE FIGURE 11 HERE

1320

1321 The age of the Koronis family, and likely that of Ida, can be computed using dynamical
1322 models. By tracking how Koronis family members have drifted in semimajor axis by the combined
1323 Yarkovsky and YORP (Yarkovsky–O’Keefe–Radzievskii–Paddack) effects, it has been estimated
1324 that the family’s age is $\sim 2\text{--}3$ Ga (Bottke et al., 2001; Brož et al., 2013; Spoto et al., 2015; see also
1325 Nesvorný et al., 2015). Error bars on this value could take it to 4 Gyr as well.

1326 There are also multiple Koronis family members (including Ida) whose spin vectors have
1327 been modified enough by the YORP effect, some to be caught in spin-orbit resonances
1328 (Vokrouhlický et al., 2003). Objects with prograde spins in so-called “Slivan states” have nearly
1329 identical periods (7.5–9.5 h), obliquities between 42° and 50° , and pole longitudes confined in a
1330 tight interval between 25° and 75° . Vokrouhlický et al. (2003) estimated that the time needed for
1331 the observed bodies with $20 < D_{\text{ast}} < 40$ km, starting with spin periods $P = 5$ hours, to reach their
1332 Slivan state status was $\sim 2\text{--}3$ Ga. Accordingly, our expectation is that Ida’s crater retention age
1333 should be close to this value.

1334 Modeling Ida’s crater history is challenging because many smaller crater sizes appear to
1335 be near or in saturation equilibrium (Chapman et al., 1996b; reviewed in Chapman et al., 2002 and
1336 Marchi et al., 2015). There are ways to deal with crater saturation using specialized codes (e.g.,
1337 Marchi et al. 2012a), but they also involve making assumptions about the nature of the saturation
1338 process; this issue will be discussed in a follow-up paper.

1339 As a work-around, we examine the crater counts provided by Fig. 5 of Chapman et al.
1340 (1996b) (Fig. 12). Their crater SFD between $0.6 < D_{\text{crater}} < 10$ km has a similar shape to those seen
1341 on Vesta and Lutetia for the same size range (Figs. 4 and 8). Only the craters with $D_{\text{crater}} < 0.6$ km
1342 seem to have the -2 cumulative power law diagnostic of saturation (e.g., Melosh 1996; see also
1343 Marchi et al. 2012a). Our main belt model will be applied to Ida’s craters with $D_{\text{crater}} > 0.6$ km.

1344

1345

PLACE FIGURE 12 HERE

1346

1347 **5.5.1 Empirical scaling law derived by fitting model and observed crater SFDs (Ida)**

1348

1349 Using a P_i value of $4.037 \times 10^{-18} \text{ km}^{-2} \text{ yr}^{-1}$ (Table 3), we obtain a best fit for SFD #8 with
1350 $\chi^2_{MB} = 1.17$ (Table 4). All of the other SFDs also fit within 1σ of this best fit case, a byproduct of
1351 the limited number of large craters in our crater SFD. As in the case for Lutetia’s Achaia region,
1352 the empirical main belt fit case is the best of the three scaling laws tested.

1353 Our best fit f value is $10.90 [-2.70, +2.90]$, and our best fit crater retention age is $T_{\text{ast}} = 2.52$
1354 $[-1.98, +0.94]$ Ga. The f value is similar to our results in previous runs, not a surprise given the
1355 location of the knee in Ida’s crater SFD at $D_{\text{crater}} \sim 2$ km. If we apply a more probable main belt

1356 SFD, such as SFD #6 (Table 1), the best fit f value moves to 10.00 [−3.40, +3.00], and our best fit
1357 crater retention age is $T_{\text{ast}} = 2.36$ [−2.36, +2.37] Ga. The lower error bar is a formal number and
1358 should not be taken literally. Both crater retention ages for Ida are consistent with the estimated
1359 dynamical ages of the Koronis family. Visually, our main belt fit curve hits both inflection points
1360 and provide a good visual match to the data.

1361

1362 **5.5.2 Housen and Holsapple crater scaling fit (Ida)**

1363

1364 For the HH scaling law case, we applied the same yield strength as before, P_i and V_{imp}
1365 values from Table 3, and projectile and target surface densities of 2.5 and 2.6 g cm^{−3}, respectively.
1366 Our best fit case was for SFD #6, which yielded $\chi^2_{MA} = 1.39$ (Table 4). As in the empirical main
1367 belt fit case, all SFDs are within 1 σ of the best fit case. The crater retention age from our best fit
1368 is $T_{\text{ast}} = 2.91$ [−0.43, +0.43] Ga, which again is a reasonable match with the dynamical age of the
1369 Koronis family. The f functions for this scaling law are slightly lower than the main belt fit, but
1370 this is balanced against a different best fit choice for the main belt SFD.

1371

1372 **5.5.3 Ivanov scaling law fit (Ida)**

1373

1374 The Ivanov scaling law yields a best fit of $\chi^2_{IV} = 1.93$ for SFD #8, which is within 1 σ of
1375 the other two scaling laws (Table 4). It produces f values near 15 for smaller projectiles, though,
1376 and this leads to a crater retention age of $T_{\text{ast}} = 1.17$ [−0.17, +0.16] Ga, much younger than from
1377 the other scaling laws. This value is outside the range estimated from dynamical models for the
1378 age of the Koronis family, though see the caveats in Sec. 3.5.1.

1379 Schmedemann et al. (2014) applied the Ivanov scaling law model and a main belt SFD
1380 similar to SFD #8 to crater counts found over a limited region of Ida. They assumed the P_i value
1381 for the impactors was 3.6×10^{-18} km^{−2} yr^{−1}, while their impact velocities were 3.3 km s^{−1}. Both
1382 values are about 90% of our values in Table 3. In this region, crater spatial densities were found
1383 to be roughly a factor of 2 higher than those in Chapman et al. (1996b) (Fig. 12). Their best fit to
1384 these craters, most of which were between 1 and 2 km in diameter, yielded an age of 3.4 to 3.6 Ga.
1385 Other surfaces with fresher craters suggested ages of ~ 2.1 Ga when their model was fit to data
1386 from craters between 0.5 and 1 km in diameter.

1387

1388 **5.5.4 Summary (Ida)**

1389

1390 The main belt fit scaling law with $f \sim 10$, along with the HH scaling law, are our preferred
1391 solutions, with main belt SFD solutions within high numbers favored from our fits. They produce
1392 mean crater retention ages of Ida near 2.5–2.9 Ga. These values are consistent with the model-
1393 derived dynamical age of the Koronis family, with Ida as a family member. The saturated crater
1394 regions on Ida do exist, however, and they could suggest an older age for Ida than 3 Ga. This
1395 would be tolerable given errors on existing family and dynamical constraints.

1396

1397 5.6 Gaspra

1398

1399 (951) Gaspra was the first asteroid ever observed by spacecraft (Fig. 11). The data returned
1400 by NASA's Galileo flyby in 1991 provided scientists with their first glimpse of what an S-type
1401 asteroid look likes up close. Gaspra has dimensions of $18.2 \text{ km} \times 10.5 \text{ km} \times 8.9 \text{ km}$ and a mean
1402 diameter of 12.2 km (Thomas et al. 1994). It is a prominent member of the Flora family that
1403 dominates the innermost region of the main asteroid belt (Nesvorný et al. 2015). The proper orbital
1404 elements of Gaspra are $(a, e, i) = (2.21 \text{ au}, 0.15, 5.1^\circ)$.

1405 Constraints on the age of Gaspra can be inferred from the evolution of the Flora family,
1406 which was formed from the catastrophic disruption of an asteroid of $D_{\text{ast}} > 150 \text{ km}$ in the orbital
1407 region adjacent to the ν_6 secular resonance (Durda et al., 2007; Vokrouhlický et al., 2017).
1408 Vokrouhlický et al. (2017) used collisional and dynamical models to track the evolution of Flora
1409 family members immediately after the family forming event. They found that test Flora family
1410 members can reproduce the observed semimajor axis, eccentricity, and inclination distributions of
1411 the real family after $1.35 \pm 0.3 \text{ Ga}$ of evolution, assuming that family members have bulk densities
1412 near $2.70 \pm 0.54 \text{ g cm}^{-3}$ (e.g., Scheeres et al., 2015; see also Dykhuis et al. 2014).

1413 This dynamical age is consistent with the $^{40}\text{Ar}/^{39}\text{Ar}$ ages of LL chondrite grains returned
1414 from (25143) Itokawa by the Hayabusa spacecraft: $1.3 \pm 0.3 \text{ Ga}$ (Nakamura et al. 2011; Park et
1415 al., 2015; see also Terada et al. 2018). Flora family members have spectra consistent with those of
1416 LL-type chondrites (Vernazza et al. 2008; de Leon et al. 2010; Dunn et al. 2013), and dynamical
1417 models indicate that Flora is perhaps the most probable source for Itokawa (Bottke et al. 2002;
1418 Granvik et al. 2016; 2018). We will discuss Itokawa in more detail below, but the correspondence
1419 of these ages suggests that Gaspra should likely have a crater retention age comparable to $1.3 \pm$
1420 0.3 Ga . In our modeling work below, we assign Gaspra a bulk density of 2.7 g cm^{-3} .

1421 The population of Gaspra's craters has been reported and modeled by several groups (e.g.,
1422 Belton et al., 1992; Greenberg et al., 1994; Chapman et al., 1996a; Chapman et al., 2002; O'Brien
1423 et al., 2006; Marchi et al., 2015). Numerous craters were identified between $0.16 < D_{\text{crater}} < 1.9 \text{ km}$
1424 that followed a cumulative power law slope of -2.6 . This size limit means Gaspra does not sample
1425 the knee in the crater SFDs observed near $D_{\text{crater}} \sim 2 \text{ km}$ on Vesta, Lutetia, Ida, and others. A
1426 possible exception may be the mysterious facets on Gaspra, one or more of which may be ancient
1427 craters with $D_{\text{crater}} > 2 \text{ km}$ (e.g., Greenberg et al., 1994; Thomas et al., 1994; O'Brien et al., 2006).
1428 None of these pseudo-craters has been verified, so we do not include them in our analysis.

1429 More recently, Gaspra's crater SFD was re-assessed using the Small Body Mapping Tool
1430 (Runyon and Barnouin, 2015; Ernst et al. 2018). The SBMT allows images to be wrapped onto an
1431 asteroid shape model, which is helpful for calculating surface areas when the body is irregular.
1432 They counted 712 craters of $0.05 < D_{\text{crater}} < 1.3 \text{ km}$ within an area of 119.6 km^2 (Fig. 13). A rollover
1433 in their counts occurs for $D_{\text{crater}} < 0.17 \text{ km}$, which they attribute to limitations of image resolution.
1434 Overall, the shape of their crater SFD was similar to that of Chapman et al. (1996a), with the power
1435 law slope of -2.6 reproduced. The normalization of the counts, however, was lower, probably

1436 because SBMT can more easily derive the irregular area of Gaspra’s observed surface. In our
1437 modeling work, we use these new counts for Gaspra.

1438

1439

PLACE FIGURE 13 HERE

1440

1441 **5.6.1 Empirical scaling law derived by fitting model and observed crater SFDs (Gaspra)**

1442

1443 Assuming $P_i = 2.635 \times 10^{-18} \text{ km}^{-2} \text{ yr}^{-1}$ (Table 3), we obtain a best fit for SFD #1 with χ^2_{MB}
1444 = 1.94 (Table 4). Although this fit appears to favor lower-number SFDs, the other SFDs all have
1445 χ^2_{MB} within 1σ of this best fit case. The reason for this behavior is that Gaspra’s observed crater
1446 SFD is effectively a power law, which is relatively easy for most models to fit. All of the main
1447 belt SFDs from Fig. 1 show power law slopes of $q \sim -2.6$ cumulative for their smallest craters,
1448 which matches the slope of Gaspra’s craters (Chapman et al. 1996a).

1449 Our best fit crater retention age for SFD #1 was $T_{ast} = 0.74 [-1.71, +0.41]$ Ga, nearly a
1450 factor of 2 lower than the Gaspra’s expected age from constraints. Negative ages when the error
1451 bars are included are not meant to be taken literally. Given the similarity of our results for the
1452 different SFDs, the fact that the other asteroids favor high-number SFDs, and that Table 1 favors
1453 SFDs #5 and #6, we find it interesting that our model results for SFDs #5 and #6 yield mean ages
1454 between $1.18 < T_{ast} < 1.38$ Ga, all very close to our constrained age for Gaspra of 1.35 ± 0.3 Ga.
1455 For these latter runs, our preferred value of f is 10.

1456

1457 **5.6.2 Housen and Holsapple crater scaling fit (Gaspra)**

1458

1459 Using the Holsapple and Housen (2007) scaling law and the same input parameters as Ida,
1460 expect for gravity, we obtain a best fit of $\chi^2_{MA} = 1.93$ for SFD #1. As before, all SFDs are within
1461 1σ of the best fit case, with SFDs #5 and #6 yielding mean ages of $1.12 < T_{ast} < 1.32$ Ga and a
1462 spread of $1.01 < T_{ast} < 1.46$ Ga when errors are included. The f value of the scaling law is near
1463 identical to the main belt fit’s estimate of $f = 10$.

1464

1465 **5.6.3 Ivanov scaling law fit (Gaspra)**

1466

1467 The Ivanov scaling law provides the best fit of the three cases, with $\chi^2_{IV} = 1.85$ for SFD
1468 #1 (Table 4). Here SFDs #2–#8 are within 1σ of the best fit. Its higher f values for smaller
1469 projectiles, however, yield an age for SFDs #5 and 6 between $0.25 < T_{ast} < 0.29$ Ga. These values
1470 are outside our age range derived from Flora and Itokawa constraints.

1471 Schmedemann et al. (2014) applied the Ivanov scaling law model and a main belt SFD
1472 similar to SFD #8 to crater counts found over a limited region of Gaspra. They assumed a P_i value
1473 for their impactors of $3.54 \times 10^{-18} \text{ km}^{-2} \text{ yr}^{-1}$, and their impact velocities were 4.69 km s^{-1} . Both
1474 values are modestly higher than our values in Table 3. They identified a steep crater SFD similar

1475 to that reported in Chapman et al. (1996a) that yielded a crater retention age of 0.27 ± 0.068 Ga.
1476 This value is similar to our prediction for the Ivanov scaling law of $0.25 < T_{\text{ast}} < 0.29$ Ga.

1477

1478 **5.6.4 Summary (Gasptra)**

1479

1480 All of our best fit models favor SFD #1, but the crater retention ages produced by our fits
1481 are substantially different than age constraints from Itokawa samples and our estimated dynamical
1482 age of the Flora family. We also argue that SFD #1 is largely disfavored according to the crater
1483 SFDs of other main belt asteroids. The higher-number SFDs, however, produce results within 1σ
1484 of this best fit case, with our preferred SFDs, namely #5 or #6, producing ages that are a good
1485 match to the Gasptra's additional age constraints (approximately 1.3 Ga). If we use those runs, our
1486 main belt scaling law fit results yield $f \sim 10$, the same values as for the asteroids discussed above.

1487

1488 **5.7 Eros**

1489

1490 We are now ready to consider the crater retention age of (433) Eros, the largest NEO
1491 observed by spacecraft. It was the primary target of NASA's NEAR mission and has a record of
1492 large craters that share commonalities with those of the main belt asteroids investigated above.

1493 Eros has dimensions of $34.4 \text{ km} \times 11.2 \text{ km} \times 11.2 \text{ km}$ and a bulk density of $2.67 \pm 0.03 \text{ g}$
1494 cm^{-3} (Thomas et al. 2002) (Fig. 14). It is classified as an S-type asteroid, and its spectral
1495 characteristics suggest that it is similar to L or LL-type ordinary chondrites (e.g., Trombka et al.,
1496 2000; Foley et al., 2006; Dunn et al., 2013; Peplowski et al., 2015; Peplowski, 2016). Recent
1497 spectral modeling work by Binzel et al. (2019) agrees with this assessment; they find probabilities
1498 of 2%, 24%, and 74% that Eros is an H, L, and LL chondrite, respectively. Their interpretation is
1499 that Eros is most likely a LL chondrite.

1500

1501 PLACE FIGURE 14 HERE

1502

1503 All of these characteristics make Eros something of a mini-Ida. Ida is an S-type with a
1504 similar bulk density and shape, but it is only half the size (Sec. 3.5). A difference between the two
1505 is Eros's orbit; it currently crosses the orbit of Mars with $(a, e, i) = (1.458 \text{ au}, 0.223, 10.83^\circ)$. This
1506 classifies it as an Amor-type NEO; it cannot currently strike the Earth, but its unstable orbit may
1507 put it in position to do so in the future (Michel et al. 1996).

1508 Objects as large as Eros have little Yarkovsky mobility (e.g., Bottke et al., 2006a). For
1509 Eros-like bodies to escape the main belt and reach an Eros-like orbit, it is helpful if they are initially
1510 located in the innermost main belt region. Here a forest of overlapping Mars and three-body
1511 resonances creates a diffusive environment for asteroids (e.g., Morbidelli and Nesvorný, 1999;
1512 Nesvorný et al., 2002; Nesvorný and Roig, 2018). Alternatively, they need to have been created
1513 by a large asteroid disruption event occurring on the brink of a prominent resonance (e.g., Zappalà
1514 et al., 1997). Either way, dynamical models suggest that Eros likely spent hundreds of millions of

1515 years to many billions of years to escape the main belt. Only the last few millions to tens of millions
1516 of Eros’s lifetime have been spent on planet-crossing orbits collisionally decoupled from the main
1517 belt population (e.g., Bottke et al. 1996; 2002). Based on this, we predict that most craters on Eros
1518 were derived from main belt impactors, and that we can model Eros’s cratering history in the same
1519 manner as the main belt asteroids discussed above.

1520 According to the NEO model of Granvik et al. (2018), Eros was derived from the Hungaria
1521 region (44%), the innermost region of the main belt (47%), or the 3:1 resonance (9%). Given that
1522 the Hungarias currently have a paucity of Eros-sized S-type asteroids, we can probably reject that
1523 region as a source for Eros. Doing so increases the probabilities that Eros came from the innermost
1524 main belt and the 3:1 resonance to 84% and 16%, respectively. These results match those of Bottke
1525 et al. (2002), whose NEO model did not include the Hungarias; they found that Eros has an 80%
1526 chance of coming from the inner main belt and 20% from the 3:1 resonance.

1527 Given that Eros likely has an LL chondrite–like composition, it is natural to once again
1528 consider the Flora family as a possible source, especially given our results for Gaspra in Sec. 3.6.
1529 Some have also postulated that Eros may be derived from the Maria asteroid family, which
1530 disrupted on the brink of the 3:1 resonance with Jupiter (Zappalà et al., 1997, 2001).

1531 Many regions on Eros appear to be close to crater saturation, with only the largest craters
1532 escaping this fate (Chapman et al., 2002; Robinson et al., 2002). The full database of Eros craters
1533 was provided to us by P. Thomas, who did the original mapping of Eros with M. Berthoud. The
1534 database is only likely to be complete for $D_{\text{crater}} > 0.2$ km (P. Thomas, personal communication).
1535 We estimate that the onset of saturation equilibrium takes place for $D_{\text{crater}} < 0.6$ km, as determined
1536 when the power law slope of the craters at small sizes moves to a $q = -2$ cumulative index value.
1537 For this reason, as with Ida, we will only examine the craters of $D_{\text{crater}} > 0.6$ km (Fig. 15).

1538

PLACE FIGURE 15 HERE

1539

1541 As an aside, we point out that seismic shaking appears to have reduced the spatial density
1542 of craters with $0.2 < D_{\text{crater}} < 0.5$ km from the vicinity of the 7.6-km Shoemaker crater (Thomas et
1543 al. 2005), and that some mechanism—perhaps impact-induced seismic shaking—also erased
1544 craters with $D_{\text{crater}} < 0.1$ km (Richardson et al. 2004). The issue of small crater erasure on asteroids
1545 is a fascinating one, but work on this topic is beyond the scope of this paper.

1546

1547 **5.7.1 Empirical scaling law derived by fitting model and observed crater SFDs (Eros)**

1548

1549 Given our limited information on the origin of Eros, we assume for now that Eros’s original
1550 orbit was in the Flora asteroid family within the inner main belt. Accordingly, we assign it a
1551 starting orbit similar to Gaspra and give it a P_i value of $2.635 \times 10^{-18} \text{ km}^{-2} \text{ yr}^{-1}$ (Table 3). Our
1552 results indicate that we obtain our best fit using SFD #2, yielding $\chi^2_{MB} = 3.72$ (Table 4). All of
1553 the other SFDs also fit within 1σ of this best fit case. Our best fit f value was $10.90 [-3.00, +3.00]$,

1554 and our best fit crater retention age is $T_{ast} = 2.03 [-2.01, +0.86]$ Ga. If we were to instead adopt
1555 SFD #5 and #6, these mean values would change to $f = 11.90$ to 12.20 and $T_{ast} = 2.32$ to 2.55 Ga.

1556

1557 **5.7.2 Housen and Holsapple crater scaling fit (Eros)**

1558

1559 Using the HH scaling law, a target density of 2.67 g cm^{-3} , and the same input parameters
1560 as for Gaspra and Ida, except for gravity, we obtain a best fit of $\chi^2_{MA} = 3.85$ for SFD #1. The
1561 SFDs #2–#7 are within 1σ of the best fit case. Collectively, they yield mean ages between $2.1 <$
1562 $T_{ast} < 4.5$ Ga. The typical f values of this scaling law are close to $f \sim 10$ for the projectile sizes used
1563 here (Fig. 15). For SFDs #5 and #6, the mean ages are between $3.34 < T_{ast} < 3.81$ Ga.

1564

1565 **5.7.3. Ivanov scaling law fit (Eros)**

1566

1567 The Ivanov scaling law provides the best fit of the three cases, with $\chi^2_{IV} = 2.27$ for SFD
1568 #8 (Table 4). Its higher f values yield an age of $T_{ast} = 1.4 [-0.19, +0.18]$ Ga (Table 5).

1569

1570 **5.7.4 Interpretation of Eros's crater record**

1571

1572 Our best fit mean crater retention ages from the main belt fit and the Marchi scaling law
1573 results are between 2.3 and 3.8 Ga. These values are substantially older than the estimated age of
1574 the Flora family (i.e., 1.35 ± 0.3 Ga; Sec. 3.6). One could dispute this, given that the best fit Ivanov
1575 scaling law's crater retention age is $T_{ast} = 1.4 [-0.19, +0.18]$ Ga. The counterarguments are that
1576 Eros has notably higher crater spatial densities than Gaspra for similar-sized craters and Gaspra is
1577 a Flora family member (Figs. 13, 15). Accordingly, we rule out Eros as a Flora family member on
1578 this basis.

1579 It has also been postulated that Eros could come from the Maria family, located adjacent
1580 to the J3:1 resonance at high inclinations (Zappalà et al., 1997, 2001). As reported above, the odds
1581 of asteroids from the J3:1 reaching an Eros-like orbit are $\sim 20\%$, less likely than the inner main belt
1582 but not unreasonably low. Several published dynamical ages for the Maria family have suggested
1583 that it is ~ 2 Ga (e.g., Spoto et al., 2015; Aljbaae et al., 2017) or possibly 3 ± 1 Ga (Brož et al.,
1584 2013). The collision probability of main belt asteroids with (170) Maria is $P_i = 2.923 \times 10^{-18} \text{ km}^{-2}$
1585 yr^{-1} , about 1.1 times the value used for the above age calculation. Multiplying our ages by this
1586 factor gives 2.2–4.1 Ga. These crater retention ages are in the same ballpark as the dynamical age
1587 estimates for Maria, given uncertainties.

1588 The problem is that the Binzel et al. (2019) spectral model predicts that (170) Maria has
1589 probabilities of 75%, 23%, and 2% of being an H, L, and LL chondrite, respectively. Given that
1590 Eros is likely a LL chondrite, it would appear that Maria can be ruled out as a candidate family on
1591 the basis of its spectral signature.

1592 Accordingly, at this time, we have no independent constraints on the age of Eros. Given
1593 the comparable qualities of the fits in Fig. 15, we cannot use its crater SFD as a measure of which
1594 crater scaling law is preferred.

1595 With that said, our crater studies above indicate that the empirical main belt and HH scaling
1596 law fits are preferred over the Ivanov scaling law fit. This suggests that the most likely scenario
1597 is that Eros was formed from the breakup of an asteroid in the inner main belt ~ 2.3 Ga to 3.8 Ga
1598 ago. The family has yet to be identified. If Eros came from a parent body that disrupted in the
1599 inner main belt, the reason that the family has not been found is plausibly because it disrupted in
1600 a highly diffusive region of this zone. Given the complicated network of resonances that exist in
1601 the inner main belt, we find it interesting but perhaps not surprising that an Eros precursor might
1602 avoid leaving behind clues to its existence after such a long time period. Less likely but still
1603 possible are that Eros came from the breakup of a body near the 3:1 resonance or from the Hungaria
1604 asteroid region. Additional work on this issue is warranted.

1605

1606 **6 Near-Earth Asteroids Smaller than 10 Kilometers**

1607

1608 Armed with the insights gleaned from Sec. 3, we now consider the crater retention ages of
1609 smaller NEOs observed by spacecraft: (25143) Itokawa, (4179) Toutatis, (101955) Bennu, and
1610 (162173) Ryugu. It is challenging to model the cratering history of any of these bodies for several
1611 reasons.

1612 First, these NEOs have experienced an erasure process that eliminated craters smaller than
1613 many tens of meters to possibly up to hundreds of meters. We do not examine erasure mechanisms
1614 in this paper, but it has been suggested that impact-induced seismic shaking or perhaps regolith
1615 mobility driven by thermal cycling may be responsible for this deficit (e.g., Richardson et al., 2004;
1616 Marchi et al., 2015). Accordingly, only the largest craters on NEOs may stretch back to deep time.

1617 To make progress in our work below, we avoid craters that may have been affected by
1618 crater erasure mechanisms. We define this as the crater diameter size range on the SFD plots
1619 discussed below where the observed and model crater SFDs diverge from one another. For
1620 Itokawa, Toutatis, Bennu, and Ryugu, this occurs for crater diameters smaller than ~ 100 m, ~ 250
1621 m, ~ 150 m, and ~ 70 - 150 m, respectively.

1622 Second, the dynamical histories of NEOs are uncertain. If we do not know where these
1623 asteroids came from in the main belt, it is difficult to predict how their collision probabilities and
1624 impact velocities varied with time. To make progress in our work below, we estimate the likely
1625 source regions and dynamical pathways followed by the bodies using our knowledge of main belt
1626 families, asteroid spectral signatures, and asteroid dynamics.

1627 Third, as discussed in the introduction, the crater scaling laws that should be employed on
1628 asteroids that are a few hundred meters to several kilometers in diameter are uncertain. For the
1629 work below, we focus our attention on two possibilities:

- 1630 • Option 1. The crater retention ages of small asteroids, based on their largest craters, are long.
1631 For NEOs, they potentially provide a record of each world's traverse from their main belt

1632 starting orbit to the resonance that pushed them onto a planet-crossing orbit (e.g., Bottke et al.,
1633 2002, 2006a). In some cases, they may even reach back to the time of their parent body's
1634 disruption event.

1635 • Option 2. The crater retention ages of small asteroids are short. For NEOs, the largest craters
1636 may only tell us about the last part of their journey in the main belt and perhaps the few millions
1637 to tens of millions of years it took to obtain their current orbits.

1638 Impact experiments and numerical hydrocode modeling work have suggested that f values
1639 for small asteroids could be much higher than those derived from our Sec. 3 work, with values of
1640 20, 40, or even 100 possible, depending on the physical properties of the target (e.g., Tatsumi and
1641 Sugita 2018).

1642 As an example, consider the recent numerical hydrocode impact experiments of Davison
1643 et al. (2019). They created a Bennu-like target with a basalt equation of state that was 20% porous
1644 and hit it with a 0.7 m diameter projectile at 7 km s^{-1} . When the strength of the target was set to
1645 0.1, 1, 10, and 100 kPa, the simulations yielded crater diameters of 37, 22, 14, and 8.9 m,
1646 respectively, which translates into f values of 53, 32, 20, and 13, respectively. The unresolved
1647 issue is what strength value is appropriate to modeling the largest craters on Bennu.

1648 If the low strength values are correct, Option 2 is preferred and our spacecraft-observed
1649 NEOs should have young crater retention ages. Option 2 might even be the expected outcome,
1650 given the estimated short timescales needed to spin small asteroids up to mass shedding via YORP.

1651 On the other hand, our modeling results above indicate that $f \sim 10$ values can explain most
1652 main belt crater SFDs on $D_{\text{ast}} > 10 \text{ km}$ asteroids (with the possible exception of $D_{\text{crater}} < 2\text{--}3 \text{ km}$
1653 craters on Ceres). This suggests that Option 1 may be viable.

1654 It is interesting to consider that craters on Vesta ($D_{\text{ast}} \sim 530 \text{ km}$) and Gaspra ($D_{\text{ast}} \sim 12 \text{ km}$)
1655 can be fit with $f \sim 10$ for $D_{\text{crater}} > 0.1$ to 0.2 km , even though they are very different in size (i.e.,
1656 the ratio of the diameter of Vesta to that of Gaspra is 44). The diameter ratio between Gaspra and
1657 our spacecraft-observed NEOs, which are $0.3 < D_{\text{ast}} < 2.5 \text{ km}$, ranges from 5 to 40. This raises the
1658 possibility that the largest NEOs in our Sec. 4 sample might follow the same trend.

1659 With all of these issues in mind, we start our investigation with Itokawa.

1660

1661 **6.1 Itokawa**

1662

1663 (25143) Itokawa, an Apollo-type S (IV)-type NEO, was the target of JAXA's Hayabusa
1664 mission (Fig. 16). Itokawa appears to be a rubble-pile asteroid, with an elongated shape
1665 (dimensions of $0.535 \text{ km} \times 0.294 \text{ km} \times 0.209 \text{ km}$) and an estimated bulk density of $1.9 \pm 0.13 \text{ g}$
1666 cm^{-3} (Fujiwara et al., 2006). It has two main components covered with rocks and boulders, and it
1667 seems likely that it was reassembled from debris produced by the disruption of the Itokawa parent
1668 body.

1669

1670

PLACE FIGURE 16 HERE

1671

1672 Hayabusa rendezvoused with Itokawa in 2005 and returned numerous grains from this
1673 body to Earth in 2010. An analysis of Itokawa samples showed this asteroid has a composition
1674 similar to LL ordinary chondrites, results that were consistent with its spectroscopic signature
1675 (Nakamura et al., 2011). Three grains yield $^{40}\text{Ar}/^{39}\text{Ar}$ shock degassing ages of 1.3 ± 0.3 Ga (Park
1676 et al., 2015), whereas seven phosphate grains dated using the U-Pb system provide reset ages of
1677 1.51 ± 0.85 Ga (Terada et al., 2018). The interpretation is that a large, possibly catastrophic impact
1678 event affected the Itokawa precursor 1.3–1.4 Ga ago.

1679 Dynamically, it can be shown that Itokawa, which currently resides on a fairly Earth-like
1680 orbit with $(a, e, i) = (1.324 \text{ au}, 0.280, 1.621^\circ)$, most likely came from the innermost region of the
1681 main belt. The NEO models of Bottke et al. (2002) and Granvik et al. (2018) suggest that the odds
1682 of Itokawa having this provenance are ~86–100%.

1683 The most prominent S-type family in the inner main belt is Flora, which formed from the
1684 catastrophic collision of a parent body larger than 150 km in diameter (e.g., Durda et al., 2007).
1685 As discussed in Sec. 3.6, dynamical models suggest that the age of the Flora family is 1.35 ± 0.3
1686 Ga (Vokrouhlický et al., 2017; see also Dykhuis et al., 2014). This age is consistent with the
1687 sample reset ages of the Itokawa samples and the inferred crater retention age of Gaspra from Sec.
1688 3.6. Finally, Itokawa is an excellent match with the LL-like spectral signature of Flora itself (e.g.,
1689 Reddy et al., 2014; Binzel et al., 2019).

1690 Putting these clues together, we predict that Itokawa was produced by the disruption of the
1691 Flora parent body, and that it was once a member of the Flora asteroid family. A likely evolution
1692 scenario is that after formation, Itokawa resided near ~ 2.2 au until it drifted inward far enough by
1693 Yarkovsky thermal forces to escape from the main belt via the v_6 secular resonance (perhaps near
1694 2.14 au).

1695 We can use this concept to calculate Itokawa’s mean collision probability and impact
1696 velocity with the rest of the main belt population. In Fig. 17, we show P_i values (and report mean
1697 V_{imp} values) for Itokawa model asteroids encountering the 682 main belt asteroids with $D_{\text{ast}} \geq 50$
1698 km discussed in Sec. 2.6. The model asteroids were assigned semimajor axes of 2.14–2.2 au and
1699 proper eccentricity and inclination values similar to Gaspra’s, a Flora family member (Table 3).
1700 They yield a mean value of $P_i = 2.401 (\pm 0.11) \times 10^{-18} \text{ km}^{-2} \text{ yr}^{-1}$ and $V_{\text{imp}} = 4.98 (\pm 0.04) \text{ km s}^{-1}$.
1701 For reference, Gaspra’s P_i value of $2.635 \times 10^{-18} \text{ km}^{-2} \text{ yr}^{-1}$ is 1.1 times that of Itokawa’s. We do
1702 not model the portion of Itokawa’s orbit where it was collisionally decoupled from the main
1703 asteroid belt; dynamical models suggest that this portion of its evolution was short compared to its
1704 journey within the main belt region (e.g., Bottke et al., 2015b).

1705

1706

PLACE FIGURE 17 HERE

1707

1708 Our prediction is that if Option 1 is correct, the largest craters in Itokawa’s crater SFDs,
1709 which are plotted per square kilometer, should lie on top of our model fit to Gaspra’s crater SFD
1710 in Fig. 13, provided we compensate for Itokawa’s slightly smaller net collision probability value
1711 (i.e., the ratio of collision probabilities for Gaspra and Itokawa is 1.1, so we need to multiply

1712 $N_{obs-crater} (> D_i)$ for Itokawa by this value). Using craters derived from the work of Hirata et
1713 al. (2009) (see also Marchi et al. 2015), we tested this idea in Fig. 18. The plot shows that Itokawa’s
1714 craters with $D_{crater} \sim 0.1$ km—those that presumably are least likely to have been affected by crater
1715 erasure—appear to be an extension of the crater SFD found on Gaspra. This result fulfills the
1716 predictions of Option 1, though it does not prove it. Given the available information at this time,
1717 it can only be considered an interesting coincidence.

1718

1719

PLACE FIGURE 18 HERE

1720

1721 For the moment, let us assume that Option 1 is true. Doing so knocks down several
1722 additional “logical dominos” and forces us to make several additional predictions that can help us
1723 interpret the other NEOs observed by spacecraft:

1724 • The crater retention age derived from the largest craters on Itokawa is the same age as the Flora
1725 family-forming event that took place approximately 1.35 ± 0.3 Ga ago.

1726 • Despite Itokawa’s small size, a crater scaling law of $f \sim 10$ allows us to reasonably estimate its
1727 crater retention age.

1728 • Given that our preferred scaling law appears to work reasonably well for asteroids larger than
1729 10 km with a variety of sizes and taxonomic types, and now appears to work for the largest
1730 craters on the smallest NEO investigated in our sample (i.e., ~ 0.3 km; Itokawa), it seems
1731 plausible that it will work in similar ways on NEOs such as Toutatis, Bennu, and Ryugu.

1732 • Despite the fact that YORP spin-up timescales are thought to be fast on Itokawa and other
1733 small worlds (see, e.g., the detected spin-up strength in Lowry et al., 2014, and Vokrouhlický
1734 et al., 2015 for other small near-Earth asteroids), the effects of YORP spin-up apparently did
1735 not lead to the erasure of craters of $D_{crater} \sim 0.1$ km.

1736 At the moment, though, all we have is an interesting coincidence, and Option 2 must still
1737 be considered viable. With these ideas in mind, we move to Toutatis, which is much closer in size
1738 to Gaspra than Itokawa.

1739

1740 6.2 Toutatis

1741

1742 (4179) Toutatis is an S-type NEO that is currently residing within the 3:1 mean motion
1743 resonance with Jupiter (Fig. 19). Its osculating orbit of $(a, e, i) = (2.53 \text{ au}, 0.63, 0.45^\circ)$ places it on
1744 an Earth-crossing orbit. The Chinese mission Chang'e-2 flew by Toutatis in 2012 and reported
1745 dimensions of $4.354 \text{ km} \times 1.835 \text{ km} \times 2.216 \text{ km}$ (Bu et al., 2015; see also Huang et al., 2013).
1746 These values largely confirmed estimates made from shape models derived using radar data (Ostro
1747 et al., 1995, 1999; Hudson et al., 2003; Takahashi et al., 2013). The estimated bulk density of
1748 Toutatis is between 2.1 and 2.5 g cm^{-3} (Ostro et al., 1999; Birlan, 2002). This value is between
1749 Itokawa’s bulk density ($1.9 \pm 0.13 \text{ g cm}^{-3}$) and that of Eros ($2.67 \pm 0.03 \text{ g cm}^{-3}$). This could mean

1750 that Toutatis has an internal structure somewhere between a classical rubble-pile (possibly like
1751 Itokawa) and a fractured or possibly shattered object with coherent fragments (i.e., Richardson et
1752 al. 2002).

1753

1754

PLACE FIGURE 19 HERE

1755

1756 The source of Toutatis is unknown. Given the available information, it is certainly possible
1757 that Toutatis is simply a background object that recently escaped the main belt. If we assume that
1758 Toutatis was once part of a prominent family, however, we can deduce a plausible parent from the
1759 available clues.

1760 We start with spectra. Reddy et al. (2012) found that the spectral signature of Toutatis is
1761 most similar to undifferentiated L-chondrites, though it lies close to various boundaries between
1762 H and L chondrites. The model described by Binzel et al. (2019) suggests a similar result, with
1763 probabilities of 46%, 46%, and 8% of Toutatis being an H, L, and LL chondrite, respectively. From
1764 these data, we can probably rule out LL chondrite source families in favor of H and L chondrite
1765 families.

1766 Next, we consider the results of dynamical models. The NEO model of Granvik et al.
1767 (2016; 2018) indicates that Toutatis has chances of 22%, 53%, 15%, and 9% of coming from the
1768 ν_6 secular resonance near 2.2 au, the 3:1 mean motion resonance with Jupiter, the 5:2 mean motion
1769 resonance with Jupiter, and being a Jupiter-family comet, respectively. There are no known
1770 Jupiter-family comets that look like S-type asteroids, so we can rule out that possibility at this
1771 time. Using the NEO model of Bottke et al. (2002), we find chances of 11%, 18%, 33%, and 39%
1772 of coming from the ν_6 secular resonance; the intermediate source Mars region, mostly in the inner
1773 main belt; the 3:1 resonance; and outer main belt sources (e.g., 5:2 resonance). These two models
1774 mostly agree with one another, though the outer main belt source is substantially higher in Bottke
1775 et al. (2002). Typically, NEOs in these models are favored to come from the inner main belt, which
1776 dominates the production of all NEOs, so the higher values found for the 3:1 and 5:2 resonances
1777 are intriguing.

1778 We are now ready to consider the observed craters on Toutatis's surface, which range from
1779 $40 < D_{\text{crater}} < 530$ m (Huang et al., 2013; Jiang et al., 2015) (Fig. 20). Craters smaller than a few
1780 hundred meters appear to have been depleted by some kind of crater erasure mechanism, like those
1781 seen on other small asteroids observed by spacecraft (e.g., Eros, Steins, Itokawa, Ryugu, Bennu;
1782 Marchi et al., 2015; Sugita et al., 2019; Walsh et al., 2019). If we only consider the largest craters,
1783 we find that their spatial densities are comparable to those on Ida or Eros (Figs. 12, 15).
1784 Accordingly, depending on the assumed collision probability P_i , and assuming Option 1 is valid,
1785 the crater retention age of Toutatis based on the largest craters is likely to be on the order of several
1786 billion years.

1787

1788

PLACE FIGURE 20 HERE

1789

1790 This result helps our deductive process because there are not many prominent S-type
1791 families in the main belt that are old enough to be plausible sources for Toutatis. If we only
1792 consider age as a discriminant, the candidate families include Flora, Maria, Eunomia, and Koronis.
1793 Flora can be eliminated because it has an LL-type composition. The Maria family is a possibility;
1794 as discussed above, it is adjacent to the 3:1 resonance, it may be > 2 Ga old, and the Binzel et al.
1795 (2019) model suggests that (170) Maria is most likely to resemble an H chondrite. The Eunomia
1796 family appears to be in the LL camp, though L chondrites cannot be ruled out (Verzazza et al.,
1797 2014). It is also adjacent to the 3:1 resonance. Finally, there is the Koronis family located next to
1798 the 5:2 resonance. The Binzel et al. (2019) model indicates that (158) Koronis, like Toutatis, has
1799 comparable odds of being an H or L chondrite. This apparent similarity could indicate that the
1800 Koronis family is a good spectral match with Toutatis.

1801 Additional clues to the origin of Toutatis may come from its inclination, which is very low
1802 (0.45°). In general, asteroids evolving into the 3:1 resonance from high-inclination sources such
1803 as the Maria or Eunomia families (proper inclinations $> 12^\circ$) have difficulty reaching such low
1804 inclinations. Instead, it is much easier to reach a low inclination orbit by starting with a low
1805 inclination source such as the Koronis family (proper inclinations $\sim 1\text{--}3^\circ$). However, Koronis
1806 family members evolving into the powerful 5:2 resonance at 2.8 au are less likely to obtain a
1807 Toutatis-like semimajor axis unless they are perturbed by the Earth during an encounter. This result
1808 is reflected in the dynamical results above. Still, the fact that Toutatis is currently on the Earth-
1809 crossing line may be a hint that such an event or events took place.

1810 To further quantify our dynamical arguments, we used results from the Granvik et al.
1811 (2018) numerical runs to determine how often test asteroids from the Maria/Eunomia and Koronis
1812 families reach the (a, e, i) orbit of Toutatis. For the former, we examined the evolution of 1759
1813 test asteroids that reached the 3:1 resonance from starting orbits of $a > 2.5$ au, $0.05 < e < 0.18$, and
1814 $11^\circ < i < 16^\circ$. These objects reached resonance in the simulation via Yarkovsky drift forces. We
1815 found that 17 of these bodies passed within $\Delta a = 0.03$ au, $\Delta e = 0.03$, and $\Delta i = 1^\circ$ of the (a, e, i)
1816 orbit of Toutatis (i.e., 2.53 au, 0.63, 0.45°).

1817 For the Koronis family, we tracked the evolution of 274 test asteroids that entered into the
1818 5:2 resonance from starting orbits of $a > 2.5$ au, $0.0 < e < 0.10$, and $0^\circ < i < 3^\circ$. Here 9 test asteroids
1819 met our threshold. If we assume that the strength of the two sources above was equal, and we
1820 normalize the results by the number of test asteroids used, we find that the ratio favoring Koronis
1821 as a source for Toutatis over Maria/Eunomia is 3.4 (i.e., $1759 / 274 \times 9 / 17$).

1822 Finally, we return to our cratering results in Fig. 20 and compare craters on Toutatis to
1823 Koronis family member Ida. We find it appealing that Toutatis crater counts are a good match to
1824 an extrapolation of the model crater SFD from Ida, though we cannot rule out a coincidence.

1825 Putting the evidence together, we postulate that on the basis of spectral, dynamical, and
1826 cratering evidence, Toutatis is a lost member of the Koronis family. If Option 1 is correct, the
1827 crater retention age of Toutatis based on its largest craters should be the same as Ida, approximately
1828 2–3 Ga.

1829

1830 6.3 Bennu and Ryugu

1831

1832 For our final test, we examine the crater histories of the NEOs Bennu and Ryugu, the targets
1833 of the OSIRIS-REx and Hayabusa2 sample return missions, respectively. They share a number of
1834 similarities, so we discuss them in tandem. The constraints discussed below mainly come from
1835 Lauretta et al. (2019), Hamilton et al. (2019), Sugita et al. (2019), and Watanabe et al. (2019):

1836 • They both have top-like shapes. Ryugu’s dimensions are $1.04 \times 1.02 \times 0.88$ km, while those of
1837 Bennu are $0.506 \times 0.492 \times 0.457$ km. This makes Ryugu about twice and eight times as large
1838 as Bennu from a diameter and volume perspective, respectively.

1839 • Both asteroids have a composition similar to primitive carbonaceous chondrites (e.g., CM or
1840 CI chondrites). The bodies are spectrally different, but in modest ways: Bennu is taxonomically
1841 classified as a B-type asteroid, whereas Ryugu is considered a Cb-type asteroid. Bennu’s
1842 composition is akin to aqueously altered CM-type carbonaceous chondrites, whereas Ryugu’s
1843 spectral signature is consistent with thermally and/or shock-metamorphosed CMs.

1844 • They have the same bulk densities and geometric albedos: 1.19 g cm^{-3} and $\sim 4.5\%$, respectively.

1845 • Both Bennu and Ryugu appear to be rubble-pile asteroids, with the definition given by
1846 Richardson et al. (2002). Their surfaces are a jumble of rocks and boulders that were likely
1847 produced in the aftermath of a family-forming event.

1848 • Their orbital parameters are similar to those of Earth and each other: Bennu’s (a, e, i) is (1.126
1849 au, 0.204, 6.035°), and Ryugu’s is (1.190 au, 0.1902, 5.884°).

1850 • The most likely candidate families to produce these bodies are Eulalia and New Polana, located
1851 in the inner main belt at low inclinations near the 3:1 mean motion resonance with Jupiter
1852 (J3:1) at 2.5 au (e.g., Campins et al., 2010; Walsh et al., 2013; Bottke et al., 2015b). Bottke et
1853 al. (2015b) argues that the New Polana and Eulalia families having an approximate $\sim 70\%$ and
1854 $\sim 30\%$ probability of producing Bennu and Ryugu, respectively. The dynamical ages of the
1855 New Polana and Eulalia families are modestly different from one another; the former is 1400
1856 $[+150, -150]$ Ma, whereas the latter is 830 $[+370, -100]$ Ma (Bottke et al., 2015b).

1857 • Both Bennu and Ryugu have obliquities that are nearly 180° ; Bennu’s is 177.6° , and Ryugu’s
1858 is 171.64° . This orientation, a probable outcome of YORP evolution (e.g., Bottke et al., 2006a;
1859 Vokrouhlický et al., 2015), indicates that both objects were migrating inward via the
1860 Yarkovsky effect when they escaped the main belt (e.g., Bottke et al., 2015b).

1861 • Given the location of the New Polana and Eulalia families between ~ 2.4 – 2.49 au, the strongest
1862 likelihood is that both Bennu and Ryugu drifted inward across the inner main belt from these
1863 starting orbits. A likely departure zone from the main belt was through the v_6 secular resonance
1864 that defines the innermost boundary of the inner main belt. At low inclinations, the v_6 resonance
1865 escape zone is near 2.15–2.2 au (Bottke et al., 2002). From there, they reached their current
1866 orbits via planetary encounters and interactions with resonances. Given the short lifetime of

1867 most NEOs (e.g., a few million to a few tens of millions of years; Bottke et al., 2002; Granvik
1868 et al., 2018), Bottke et al. (2015b) predicted both Bennu and Ryugu escaped the main belt
1869 relatively recently compared to their long transit across the inner main belt.

1870 To glean insights into the crater retention ages of Bennu and Ryugu, it is useful to compare
1871 their crater SFDs to an asteroid whose age and crater history are arguably well constrained. Here
1872 we choose Gaspra, a member of the Flora family, as our reference surface (Sec. 3.6; Figs. 11 and
1873 13). The reasons why are as follows: Gaspra is located near the likely escape route of Bennu and
1874 Ryugu from the main belt, and Gaspra's crater retention age of 1.3 ± 0.3 Ga is both close to the
1875 estimated family ages of Eulalia and New Polana and is arguably well defined (i.e., it is consistent
1876 with sample ages from Itokawa and the likely age of the Flora family; see Secs. 3.6 and 4.1). Here
1877 we will superpose the crater SFDs of Bennu and Ryugu on Gaspra's and examine the similarities
1878 and differences.

1879 For the comparison to be meaningful, we will assume that the crater scaling laws for Bennu
1880 and Ryugu are the approximately the same as that of Gaspra. This may be incorrect, with the
1881 worlds having different diameters (0.5 and 1.0 km vs. 12.2 km) and compositions (primitive
1882 carbonaceous chondrite vs. LL chondrite), but for the moment we accept this premise. We return
1883 to this issue in Sec. 5.

1884 Second, we need to scale the Bennu-Ryugu crater SFDs for the different collision
1885 probabilities that they experienced compared to Gaspra over their orbital histories. As discussed
1886 above, Bennu and Ryugu probably came from the low-inclination Eulalia or New Polana families.
1887 Accordingly, Bennu and Ryugu probably started with semimajor axes of $2.4 < a < 2.48$ au and
1888 inclinations $i \sim 2-3^\circ$. Next, they would have slowly migrated inward across the inner main belt
1889 until escaping out of the ν_6 resonance. To account for this evolution, we ran collision probability
1890 simulations of test asteroids with $(a, e, i) = (2.14 \text{ to } 2.48 \text{ au}, 0.1, 3^\circ)$ against our asteroid population
1891 with $D_{\text{ast}} > 50$ km using the methodology discussed in Bottke et al. (1994) (Fig. 17). We ignore
1892 the small portion of time that Bennu and Ryugu were on planet-crossing orbits. If we assume that
1893 Bennu and Ryugu had a starting orbit in the Eulalia family, the mean P_i value for their evolution
1894 is $(3.3 \pm 0.46) \times 10^{-18} \text{ km}^{-2} \text{ yr}^{-1}$. If we instead assume that they started in the New Polana family
1895 at 2.4 au, the mean P_i for their evolution is $(3.1 \pm 0.39) \times 10^{-18} \text{ km}^{-2} \text{ yr}^{-1}$.

1896 The collision probability of Gaspra, $P_i = 2.635 \times 10^{-18} \text{ km}^{-2} \text{ yr}^{-1}$, is 0.8 to 0.85 times that
1897 of Bennu/Ryugu. If we want to compare the crater SFD of Gaspra to those of Bennu and Ryugu,
1898 we need to multiply $N_{\text{obs-crater}} (> D_i)$ for Bennu and Ryugu by one of these values. This will
1899 allow us to visually determine whether Bennu and Ryugu are younger or older than Gaspra in a
1900 relative sense. If Bennu and Ryugu's crater SFD is lower on a cumulative plot than Gaspra's, its
1901 crater retention age is younger than 1.3 ± 0.3 Ga, whereas if it is higher, it is older. Our results are
1902 shown in Figs. 21 and 22.

1903

1904

PLACE FIGURE 21 HERE

1905

1906

PLACE FIGURE 22 HERE

1907

1908 We find that Ryugu’s craters with $D_{\text{crater}} > 0.15$ km (Sugita et al. (2019) appear to be a good
1909 fit with Gaspra’s craters and the model production crater population (Fig. 21). Taken at face value,
1910 this would suggest that Ryugu’s retention age for these craters is in the range of 1.3 ± 0.3 Ga. This
1911 result is interesting because the dynamical ages of Ryugu’s postulated source families, New Polana
1912 and Eulalia, also match these values (i.e., 1400 [+150, -150] Ma, 830 [+370, -100] Ma,
1913 respectively; Bottke et al. 2015b).

1914 Benu’s largest craters (Walsh et al. 2019) also appear to produce a comparable fit, though
1915 there is room for interpretation based on the SFD of craters with $D_{\text{crater}} > 0.05$ km (Fig. 22). Many
1916 of Benu’s proposed craters in this size range have subdued topography, which makes it difficult
1917 to know whether all of them are valid. In addition, the crater counts from Walsh et al. (2019) are
1918 based on data acquired early in the Benu encounter. Since then, the asteroid has been imaged and
1919 the topography measured via lidar to much higher resolution. Additional work on this issue is
1920 needed as the crater population is updated using these more recent data.

1921

1922 6.5 Summary

1923

1924 Our results suggest that Option 1 may be valid, and that the crater retention ages of NEOs,
1925 based on their largest craters, could be surprisingly old. The largest craters on Itokawa, a possible
1926 member of the Flora family whose age is ~ 1.3 Ga, appear to line up with the crater SFD found on
1927 Gaspra, a confirmed member of the Flora family. The same can be said for Toutatis, a possible
1928 member of the Koronis family (~ 2 to 3 Ga), and Ida, a confirmed member of the Koronis family.
1929 The largest craters on Benu and Ryugu also appear to be as ancient as those found on Gaspra,
1930 once we account for the different collision probabilities of the impacting population. For each
1931 one, this could suggest that some aspects of their surfaces go back as far as the family-forming
1932 event that made them. It may be possible to check Option 1 by analyzing the samples returned by
1933 the OSIRIS-REx and Hayabusa2 missions.

1934 In Sec. 7, we will discuss the implications of our findings and whether they make sense
1935 given what we know about other modeling and observational data.

1936

1937 7. Discussion

1938

1939 In this paper, we use a new formulation of the main belt size distribution to examine the
1940 crater histories of asteroids observed by spacecraft. Some of the key takeaways from our work are
1941 as follows.

1942

- 1943 1. We have used a disruption scaling law that allows asteroids of $D_{\text{ast}} \sim 0.2$ km to break up more
1944 easily than with the scaling law used by Bottke et al. (2005b) (or Benz and Asphaug, 1999). It
1945 is capable of producing a main belt size distribution that is more consistent with crater

1946 constraints than previous work. We find our best results for Q_D^* functions that are higher in
1947 number, with #5 and #6 favored when Table 1 probabilities are also considered.

1948
1949 A question that emerges from our research is whether our new asteroid disruption law
1950 reflects reality. Unfortunately, it is difficult to assess this issue here without obtaining additional
1951 main belt and asteroid constraints. The mismatch between our scaling law and those derived using
1952 hydrocode simulations, such as in Benz and Asphaug (1999), may be a clue that our methodology
1953 is missing something, previous scaling laws are missing something, or that everyone is missing
1954 something.

1955 In addition to possible issues with methodologies, there may be an issue of how the
1956 problem we are investigating is framed. For example, it has been argued that the spin-up of small
1957 asteroids by the YORP thermal torques produce frequent mass shedding events, and that this extra
1958 source of disruption acts to make the power law slope of the main belt size distribution more
1959 shallow than expected between $0.2 < D_{\text{ast}} < 2$ km (Marzari et al., 2011; Jacobson et al., 2014; Penco
1960 et al., 2004; see discussion in Bottke et al., 2015a). If true, the new asteroid scaling law would
1961 essentially replace YORP disruption with impact disruption. From the physics perspective, this
1962 works against our collisional evolution model, which does not include this effect, but from the
1963 frame of trying to model crater size distributions on asteroids, it may not matter if the two methods
1964 yield the same main belt SFD.

1965 It is also conceivable that both processes work together. Laboratory experiments indicate
1966 that asteroids spinning near their rotational breakup limit are much easier to disrupt by impact than
1967 slow-spinning bodies (e.g., Holsapple 2007). This effect was recently studied by Ševeček et al.
1968 (2019), who performed a large number of numerical impact simulations with rotating targets using
1969 a smoothed particle hydrodynamics code coupled to an N -body code (e.g., see Durda et al. 2004).
1970 They found that the critical energy needed to disrupt a target (i.e., the Q_D^* function) changed rapidly
1971 when one approaches the critical spin rate of an asteroid. Unfortunately, their study was limited to
1972 bodies 10 to 100 km in diameter, substantially larger than the ~ 0.2 -km bodies whose disruption
1973 threshold changes the most in Fig. 2. Future work on this issue is needed.

1974 For the moment, let us assume that the YORP effect drives a modest fraction of rubble-pile
1975 asteroids with $0.2 < D_{\text{ast}} < 2$ km to spin near their disruption limit (e.g., Pravec et al., 2008, 2010),
1976 and that this makes them easier to break up by impacts. From a one-dimensional collisional
1977 modeling perspective, when their short collisional lifetimes are combined with longer ones from
1978 slow rotators, the net effect is that these asteroids are easier to disrupt on average than before. In
1979 effect, this rationale can explain the shape of our new asteroid disruption law, even if our purely
1980 collisional model does not account for the physics producing it.

1981 New work will be needed to see how our asteroid disruption law holds up when new
1982 constraints become available, more is known about how asteroids disrupt via YORP spin-up, or
1983 more is known about the impacts and YORP spin-up working in tandem.

1984

1985 2. Our favored main belt size distribution (#5 or #6) can be successfully fit to the observed crater
1986 size distributions found on Ceres (Kerwan basin), Vesta (Rheasilvia basin), Lutetia, Mathilde,
1987 Ida, Gaspra, and Eros. Our results indicate that the ratio of crater diameter to projectile diameter
1988 f for craters with $D_{\text{crater}} > 0.1$ km on these worlds is ~ 10 . The only exception found so far may
1989 be craters smaller than a few km on the 930-km-diameter asteroid Ceres.

1990

1991 Our fits between model and crater data indicate that a simple relationship exists between
1992 projectiles and crater sizes on asteroids of $D_{\text{ast}} > 10$ km. Our test set includes a wide range of
1993 asteroid sizes and compositions. Our results also appear broadly consistent with the crater scaling
1994 laws of Holsapple and Housen (2007), provided we use certain input parameters (i.e., those
1995 suggested by Marchi et al. (2012b) for stony asteroids).

1996 With this said, we add some cautionary notes on this interpretation. The size distribution
1997 of craters smaller than a few km on Ceres appears to differ from those on Vesta, with the Ceres
1998 SFD having a much steeper power law slope. If this is not a byproduct of secondary craters, the
1999 easiest explanation is that these craters on Ceres are a byproduct of an increasing f value and
2000 possibly different material properties for the terrains in question.

2001 It should also be said that our $f \sim 10$ solution for Mathilde's crater SFD is (i) not unique, (ii)
2002 based on limited crater data, and (iii) fit to craters that are close to saturation. This situation is
2003 unfortunate because Mathilde is the only carbonaceous chondrite-like asteroid imaged by
2004 spacecraft to date that is larger than Ryugu (0.9 km) and smaller than Ceres (930 km). Still, we
2005 consider our solution reasonable because $f \gg 10$ scenarios would require some kind of surface
2006 reset event within the past billion years that so far lack supporting evidence. The fact that Mathilde
2007 has no observed family (Nesvorný et al., 2015) is an argument against the occurrence of such a
2008 reset event.

2009 The reasons why the $f \sim 10$ scaling law works as well as it does for many different asteroid
2010 sizes and compositions will require additional study, but certain factors probably play a role:

- 2011 • Most of the asteroids investigated to date probably have comparable material strengths, at least
2012 against impact events. They can be considered fractured or shattered versions of the stony
2013 meteorites in our collection.
- 2014 • The collision velocities between asteroids in the main belt does not vary strongly from world
2015 to world, with typically mean velocities near ~ 5 km s⁻¹ (Bottke et al., 1994).
- 2016 • The surface histories of the asteroids investigated here have been dominated by impacts from
2017 a main belt SFD whose shape has been in quasi-steady state for billions of years. Although
2018 different asteroids disrupt over time, the broad-scale properties of the main belt population
2019 have not changed substantially from a collisional evolution perspective over that interval.

2020 The influence of impactors embedded in the early main belt population (e.g., comets
2021 implanted in the primordial asteroid belt; Levison et al., 2009; Vokrouhlický et al., 2016) has yet
2022 to be detected in the crater histories of main belt asteroids. The reason is probably because few if
2023 any of the surfaces investigated in this paper go back to the primordial days of the main belt. To

2024 explore earlier bombardment eras, we would need to examine the most ancient surfaces on Vesta
2025 or other as-of-yet unobserved large asteroids. This remains a fascinating topic for future work.

2026

2027 3. Our derived main belt size distribution, combined with a crater scaling law of $f \sim 10$, can be fit
2028 to the largest craters on Itokawa, Toutatis, Bennu, and Ryugu. All of these asteroids are smaller
2029 than Gaspra. The match yields a crater retention age on the order of ~ 1 Ga for Itokawa, Bennu,
2030 and Ryugu and ~ 2.5 Ga for Toutatis. These values are consistent with the computed formation
2031 ages of their source families (Itokawa from the Flora family, Bennu and Ryugu from the Eulalia
2032 or New Polana families, Toutatis from the Koronis family), though that does not prove they
2033 actually have these surface ages.

2034

2035 The possibility that the largest craters on these asteroids are ancient matches modeling
2036 work (e.g., Walsh et al. 2019) but we still consider it something of a surprise. Therefore, we will
2037 discuss this topic further below. Our work shows four out of four examples where the crater
2038 retention ages of small asteroids match their predicted family ages. If this is merely a coincidence,
2039 it is a good one. With that said, there are other factors to consider here, and they may suggest that
2040 the crater retention age of Itokawa, Toutatis, Bennu, and Ryugu are younger than postulated. We
2041 present the arguments and their possible counters below.

2042

2043 **7.1 Factor 1. Does Spin Up from YORP Reset the Surfaces of Most Small NEOs?**

2044

2045 Over the past decade, it has become increasingly apparent that the YORP thermal torques
2046 modify the spin rates and obliquities of asteroids smaller than Gaspra (e.g., reviewed in Bottke et
2047 al. 2002, 2006a; Vokrouhlický et al. 2015). They provide the easiest way to explain the spin rate
2048 distribution of NEOs and MBAs—which include numerous bodies spinning near fission speeds
2049 and other bodies that have almost no rotational angular momentum (e.g., Pravec et al., 2008)—
2050 and their obliquity distribution, with small MBAs having preferentially extreme obliquity values
2051 (e.g., Hanuš et al., 2013; Ďurech et al., 2018) and many NEOs having values near $\sim 180^\circ$ (e.g., La
2052 Spina et al., 2004; Farnocchia et al. 2013). They may also provide a ready explanation for the
2053 spinning top–like shapes of Bennu, Ryugu, and many other asteroids (e.g., Walsh and Jacobson,
2054 2015).

2055 Direct measurement of YORP accelerations indicate that they should frequently cause
2056 asteroids to undergo mass shedding events (e.g., Pravec et al., 2010; Jewitt et al. 2015). As a second
2057 example, in situ studies of Bennu indicate that its rotation rate is currently accelerating at a rate of
2058 $(3.63 \pm 0.52) \times 10^{-6}$ deg day⁻², enough to double Bennu’s rotation rate in 1.5 Myr (e.g.,
2059 Hergenrother et al., 2019; Scheeres et al. 2019), and a similar acceleration was detected for a
2060 number of other small NEAs (reviewed in Vokrouhlický et al., 2015).

2061 The implication of these results is that small asteroids can be quite dynamic places. Many
2062 should undergo surface changes on timescales that are short compared to our estimated crater
2063 retention ages for small NEOs.

2064 A caveat is so-called stochastic YORP, namely that asteroid shape changes driven by mass
2065 movement, craters, and mass shedding can cause an asteroid’s spin acceleration to undergo a
2066 random walk (Statler, 2009; Bottke et al., 2015b). This effect may prevent some asteroids from
2067 reaching the kinds of rotation speeds that allow for frequent mass shedding events, or at least
2068 considerably delay it, whereas others may enter into mass shedding events again and again.
2069 Another intriguing possibility is that YORP self-regulates itself into a long-lived equilibrium states
2070 for the surviving population of bodies, or at least a sub-population, weakening considerably the
2071 YORP effects (e.g., Golubov and Scheeres, 2019).

2072 Until this process is better understood, we must leave open the possibility that Itokawa,
2073 Toutatis, Benu, and Ryugu fall into the former class of objects, and that their largest craters are
2074 indeed ancient.

2075 There is also the possibility that some top shapes are formed in the family-forming event,
2076 with small objects growing by the gravitational reaccumulation of debris (Michel et al, 2019). In
2077 this scenario, ejected material grows by the gravitational accretion of nearby bodies, and this leads
2078 to more mass being accreted near the equator of the growing rubble-pile asteroid than near the
2079 pole. If true, the shapes of Benu and Ryugu may indeed be ancient, which would lend credence
2080 to the idea that they have old retention ages for their largest craters.

2081

2082 **7.2 Factor 2. Are Near-Earth Objects Preferentially Long-Lived Asteroids?**

2083

2084 Our CoDDEM model results allow us to make predictions of the typical collisional lifetime
2085 of asteroids based on a choice of our asteroid disruption law (Q_D^*). We find that the sizes of the
2086 smallest asteroids in our sample, Itokawa and Benu, are relatively close to the minimum in the
2087 Q_D^* function shown in Fig. 2. Accordingly, these bodies should be easier to disrupt on an energy
2088 per mass scale by impact events than asteroids that are considerably smaller or larger.

2089 There are feedbacks here, however, with the shallow slope of the main belt SFD between
2090 0.2 and 2 km leading to fewer projectiles for $D_{\text{ast}} < 0.2$ km than estimated by Bottke et al. (2005b).
2091 This leads to an average collisional lifetime for Itokawa- and Benu-sized asteroids on the order
2092 of one hundred to a few hundred Myr, comparable to the values estimated in Bottke et al. (2005b).
2093 Regardless, these intervals are much shorter than the estimated crater retention ages of Itokawa
2094 and Benu. This mismatch is a potential argument that the crater retention ages of the largest
2095 craters are not the order of 1 Ga, but instead are much younger.

2096 The counter to this argument is to consider how Itokawa- and Benu-sized asteroids from
2097 a given family escape the main belt after a family-forming event. As a useful example, we refer
2098 the reader to the model results from Bottke et al. (2015b). They used numerical simulations to
2099 track how Benu-sized asteroids from the Eulalia, New Polana, and Erigone families evolved in
2100 semimajor axis by the coupled Yarkovsky/YORP effects. Their work accounted for the likely
2101 collisional lifetime of their model asteroids; those that disrupted were removed from the
2102 simulation. Their goal was to reproduce the distribution of these families in semimajor axis-
2103 absolute magnitude (a, H) space, where the observed families make a quasi-“V”-shape.

2104 The setup for the Bottke et al. (2015b) simulations were as follows. They assumed a large
2105 breakup event created a size distribution of asteroids representing the Eulalia, New Polana, and
2106 Erigone families. As shorthand, we classify 0.3- to 1-km bodies as “small”, 1- to 4-km bodies as
2107 “modest-sized”, and objects larger than 4 km as “big”. All of these bodies begin to drift inward or
2108 outward towards resonances via the Yarkovsky and YORP effects. YORP torques cause the
2109 obliquities of the bodies to evolve toward 0° or 180° , where they obtain their maximum semimajor
2110 axis drift velocities from the Yarkovsky effect. The smaller fragments migrate more quickly than
2111 the modest-sized ones, which in turn move faster than the big ones. This creates a V-shape in (*a*,
2112 *H*) space, with smaller objects evacuated from the middle of the family (e.g., Fig. 18 of Bottke et
2113 al. 2015b). We refer to the two sides of the V-shape as “ears”.

2114 As small and modest- sized bodies disrupt, according to their assumed collisional lifetimes,
2115 attrition takes its toll on the leading edge of each ear. Only a fraction live long enough to make it
2116 to an “escape hatch” resonance that will take them out of the main belt. Some of these bodies also
2117 go through YORP cycles, where their obliquity values are reset by various processes. The small
2118 bodies have the shortest timescale to undergo YORP cycles, and it causes them to undergo a
2119 random walk in semimajor axis, slowing their progress toward an escape hatch resonance.

2120 Eventually, though, this wave of surviving bodies reaches an escape hatch resonance. A
2121 specific example is shown in Fig. 19 of Bottke et al. (2015b), where Bennu-sized bodies from
2122 Eulalia and New Polana reached various inner main belt resonances over timescales of 0.1 to > 2
2123 Gyr after the family forming event. The expected flux of these escaping bodies at the estimated
2124 ages of the families was found to be consistent with the available constraints.

2125 Taken together, these results indicate that the NEO population might be dominated by
2126 “lucky” asteroids that are long-lived survivors. An analogy might be World War I soldiers running
2127 across no man’s land to reach the trenches of their enemy; most soldiers fall during the assault, but
2128 a few make it. If this scenario is accurate, Itokawa, Toutatis, Bennu, and Ryugu would be survivors
2129 of this gauntlet, which would make their putative ancient large craters less surprising and more of
2130 a selection effect. On the other hand, a small asteroid can survive and still not have an ancient
2131 crater retention age. The takeaway is that it may not be straightforward to interpret the surfaces of
2132 these small asteroids.

2133 It is also possible that Itokawa, Toutatis, Bennu, and Ryugu are second-generation family
2134 members, but we predict that is unlikely. When big family members disrupt, they will create some
2135 modest-sized bodies and lots of small bodies, all which can now drift more rapidly. The starting
2136 location of these fragments, however, will often be closer to the center of the family than at great
2137 distances from the center. The initial second-generation population will also be in smaller in
2138 numbers than the initial first-generation population, and they experience the same attrition factors
2139 as first-generation bodies. All of this suggests that the second-generation bodies that escape the
2140 main belt are unlikely to outnumber the first-generation bodies for a considerable time after the
2141 family-forming event.

2142
2143

2144 **7.3 Factor 3. What Crater Scaling Laws are Applicable to Small Asteroids?**

2145

2146 There is considerable debate about the projectile sizes needed to make small craters on
2147 asteroids, primarily because the strength of the surface materials is unknown. Estimates in the
2148 literature differ by many orders of magnitude, and this can change f values from 10 to 40 or more
2149 (e.g., O’Brien et al. 2006; Tatsumi and Sugita 2018).

2150 An innovative way to glean insights into this issue was through the Small Carry-on
2151 Impactor (SCI) experiment carried by JAXA’s Hayabusa2 mission to Ryugu. The SCI consisted
2152 of a 30-cm disk impactor made of copper that was accelerated by an explosion to an impact speed
2153 with Ryugu of 2 km s^{-1} . The impact produced a cone-shaped debris curtain and a crater-like feature
2154 that was approximately $17.6 \pm 0.7 \text{ m}$ in diameter rim to rim (Arakawa et al. 2020). This value is
2155 so large that the Hayabusa2 team suggested that Ryugu’s surface acts like it has the same strength
2156 as cohesionless sand upon impact, corresponding to $f \gg 10$. If so, and if we can assume this result
2157 is applicable to all Ryugu craters, it would imply that Ryugu’s crater retention age is considerably
2158 younger than 1 Ga.

2159 The caveat that we can provide at this time is that the creation of craters with $D_{\text{crater}} > 100$
2160 m on Ryugu may be different than the formation of much smaller craters a few tens of meters
2161 across. If true, different projectile sizes are sensitive to how the terrains can change as they become
2162 larger (e.g., boulder concentrations per unit area, etc.).

2163

2164 **7.4 Factor 4. Do Scaling Laws Change the Size Distributions of Small Craters?**

2165

2166 Assuming that the crater retention ages for Itokawa, Toutatis, Bennu, and Ryugu are young
2167 carries its own implications. For example, it means that crater scaling laws must change between
2168 Eros- and Gaspra-sized and larger objects ($D_{\text{ast}} > 10 \text{ km}$), which have $f \sim 10$, and smaller asteroids,
2169 where presumably $f \gg 10$. From our work above, it is not yet clear how one would tell the
2170 difference between the two.

2171 As an example, consider two asteroids with the same age, a large one where $f \sim 10$ and a
2172 small one where $f \sim 50$. Our model main belt SFD in Fig. 1 shows that the slope of $< 0.1\text{-km}$
2173 asteroids follows a Dohnanyi-like power law slope of -2.6 (e.g., O’Brien and Greenberg, 2003;
2174 Bottke et al., 2015a). If we assume that projectiles striking from this portion of the SFD will create
2175 a crater SFD on these two bodies with the same slope, the only outward difference between the
2176 two would be in crater spatial densities.

2177 The hope would be to find a transitional target body where large craters follow $f \sim 10$ and
2178 smaller craters follow $f \gg 10$. This would produce a change in the slope of the crater SFD that
2179 would be observable. The issue is that crater erasure on small bodies makes such signatures rare
2180 or hard to interpret. We speculate that crater erasure may even be a byproduct of this change in f ;
2181 models indicate that increasing f for small craters might make them more effective at crater erasure.
2182 This scenario warrants further work.

2183 The prevalence of a Dohnanyi-like power law slope of -2.6 at small asteroid sizes may
2184 also help explain the coincidence of why the largest craters on Itokawa, Toutatis, Bennu, and
2185 Ryugu have the same crater retention age as their putative source families. For every target body,
2186 there must be a largest crater than can form; asteroids striking a surface that are larger than a critical
2187 threshold will produce an asteroid-wide surface resetting event and/or disruption. Our work
2188 indicates that f values near 10 or $\gg 10$ will be drawn from the same -2.6 slope in the main belt
2189 SFD. If $f \gg 10$, we can expect a young crater retention age, with the largest possible crater
2190 forming relatively quickly compared to the formation age of the asteroid.

2191 If this logic holds, it could be rare for the surface of a small asteroid to be caught between
2192 a reset event and the formation of its largest crater. This would make the true crater retention ages
2193 of Itokawa, Toutatis, Bennu, and Ryugu much younger than suggested.

2194 One way to test this hypothesis is to determine the shock resetting (e.g., Ar-Ar) and surface
2195 (cosmic ray exposure) ages of samples returned from Bennu and Ryugu. We might expect to find
2196 the formation age of the family in the samples, as was attempted for Itokawa (e.g., Park et al.,
2197 2015), but there may also be evidence of other impact events. If they skew toward younger ages,
2198 this may be evidence that impacts only affected those rocks that had been brought to the surface
2199 over relatively recent times. On the other hand, finding numerous impact ages could tell us that
2200 (i) the surface is indeed ancient or (ii) there have been a multitude of resetting events, with the
2201 samples recording impacts back to the formation of the target asteroid.

2202

2203 **8. Future Work**

2204

2205 Future work promises to increase the fidelity of the four components of our crater
2206 production models presented in Sec 2.1. For example, one way to improve our calculation of
2207 Component 1 (assessment of main belt SFD) is for new surveys of main belt asteroids to come
2208 online that can more easily detect sub-km asteroids. A present-day example of this comes from
2209 Heinze et al. (2019), who discussed how Dark Energy Camera observations have probed the small
2210 body size distribution of the main belt. It is also expected that future wide field surveys such as
2211 the Vera C. Rubin Observatory, previously referred to as the Large Synoptic Survey Telescope
2212 (LSST), and NASA's Near-Earth Object Surveillance Mission will be able to detect numerous
2213 main belt bodies in the sub-km range across the main belt.

2214 These surveys will also give us increased knowledge of the nature of the km- and sub-km
2215 main belt populations. This information is needed to calculate improved collision probabilities
2216 and impact velocities between our target asteroids and a representative population of main belt
2217 asteroids (Component 3).

2218 In terms of crater scaling laws for small asteroids (Component 2), new data will be provided
2219 by NASA's Double Asteroid Redirection Test (DART) mission (Cheng et al. 2018) and ESA's
2220 Hera mission (Michel et al. 2018). DART is a kinetic impactor that will hit the 160 m moon of
2221 Didymos, a 780-m-diameter near-Earth asteroid. This event will make a crater and change the
2222 angular momentum of the system. Hera will follow-up the DART mission with a detailed post-

2223 impact survey of the Didymos system. From Hera, we will gain new insights into the projectile
2224 sizes needed to make small craters on asteroids, and this will translate into new constraints for
2225 crater scaling laws.

2226 Finally, we predict that new dynamical modeling work and meteorite/sample analysis may
2227 lead to additional constraints for Component 4, the crater retention age of target asteroids. For
2228 example, future work may help us identify the likely source family of Eros. If that happens, we
2229 can use dynamical models to determine the age of the family-forming event and compare that age
2230 to the predicted crater retention age of Eros (i.e., as discussed in Sec. 5.7, we modestly favor a
2231 crater retention age of ~ 2.3 to 3.8 Ga, but that is based on an assumed starting location and
2232 evolutionary history for Eros). In addition, new work on the shock degassing ages of meteorites
2233 may allow us to pin down the starting location of certain asteroids and refine our predicted crater
2234 retention ages. We look forward to an analysis of the samples return from Bennu by the OSIRIS-
2235 REx spacecraft and from Ryugu by the Hayabusa2 spacecraft. They may retain a record of the
2236 family-forming event that created them.

2237

2238 9. Conclusions

2239

2240 Here we summarize the main conclusions of our paper.

2241 We have derived a new formulation of the main belt SFD that is modestly different from
2242 the one proposed by Bottke et al. (2005b) (Sec. 3). We have successfully fit it to numerous asteroid
2243 crater SFDs observed by spacecraft. Our results for Ceres (multi-km craters only), Vesta, Lutetia,
2244 Mathilde, Ida, Eros, and Gaspra yield a crater scaling law where the ratio of crater sizes to
2245 projectile sizes is a factor $f \sim 10$ (Sec. 5).

2246 From a probability standpoint, our results favor the main belt SFDs #5 and #6 (Fig. 1; see
2247 also Fig. 2). They are likely to reproduce main belt SFD and family constraints as well as
2248 constraints from asteroid craters (Sec. 5).

2249 Our derived empirical scaling law largely match the results produced by the crater scaling
2250 law of Holsapple and Housen (2007), provided certain parameters are used (i.e., we assume that
2251 the surface material acts like cohesive soils, and that the yield strength of most asteroids is on the
2252 order of $Y \sim 2 \times 10^7$ dynes cm^{-2} . Typical values from our input parameters yield $f \sim 10$ (Sec. 3).

2253 Conversely, the scaling law of Ivanov (2004) yields poorer fits than the other tested scaling
2254 laws for large asteroids, mainly because its parameter choices yield $f \gg 10$ for target asteroids
2255 that are $D_{\text{ast}} > 10$ km. The $f \gg 10$ values also produce crater retention ages on asteroids that are
2256 inconsistent with independent ages derived using dynamical methods and/or sample evidence (Sec.
2257 5).

2258 For the spacecraft-observed asteroids and surfaces tested in this paper, we summarize our
2259 findings below and in Table 6.

2260

2261

PLACE TABLE 6 HERE

2262

2263 Vesta (Rheasilvia Basin). We find that the crater retention age of the ~500-km Rheasilvia
2264 basin on Vesta is probably younger than 1.3 Ga, with a plausible value near ~1 Ga. These ages
2265 are consistent with the $^{40}\text{Ar}/^{39}\text{Ar}$ ages found in feldspar grains taken from eucrite meteorites, which
2266 range between 0.6 and 1.7 Ga (Lindsey et al., 2015) (Sec. 5.1).

2267 Ceres (Kerwan Basin). We predict that the crater retention age of the ~280-km Kerwan
2268 basin on Ceres, based on fits to the multi-km and larger craters, is approximately 0.8 to 0.9 Ga.
2269 Our preferred model of $f \sim 10$, however, may not fit the crater SFD for $D_{\text{crater}} < 2$ km. The
2270 inconsistency in the power law slopes of sub-km craters on Ceres and Vesta could suggest that (i)
2271 secondary craters dominate the crater SFD of small craters on Ceres or (ii) the physical properties
2272 of Ceres's surface are so different from that of Vesta that they allow $f \gg 10$ for small craters (Sec.
2273 5.2).

2274 Lutetia (Achaia Region). The crater retention age of the oldest surface on M-type asteroid
2275 Lutetia (Achaia) is the order of 2.5 to 3.5 Ga, though error bars indicate it could also be as old as
2276 the formation of Lutetia itself (Sec. 5.3).

2277 Mathilde. The crater retention age of Mathilde, a carbonaceous chondrite asteroid that is
2278 larger than Bennu and Ryugu and smaller than Ceres, appears to be somewhere between 2.2 Ga
2279 and the formation age of the body itself, which could go back to the planetesimal formation era.
2280 Our interpretation is that $f \sim 10$ for this body makes the most sense; $f \gg 10$ would yield crater
2281 retention ages so young that we would expect to see a family associated with Mathilde (Sec. 5.4).

2282 Ida. The crater retention age of S-type asteroid Ida, a member of the Koronis family,
2283 appears to be between 2–3 Ga, though it could be older depending on the cratered surface analyzed.
2284 This age is consistent with the expected dynamical age of the Koronis family (Sec 5.5).

2285 Gaspra. The crater retention age of S-type asteroid Gaspra, a member of the Flora family,
2286 appears to be ~ 1.3 Ga. This age is consistent with the expected dynamical age of the Flora family.
2287 It also matches the $^{40}\text{Ar}/^{39}\text{Ar}$ ages of LL chondrite grains returned from Itokawa by the Hayabusa
2288 spacecraft: 1.3 ± 0.3 Ga (Park et al., 2015). We predict that Itokawa is very likely to have been a
2289 Flora family member prior to becoming an NEO (Sec. 5.6).

2290 Eros. The crater retention age of S-type asteroid Eros is between ~2.3 to 3.8 Ga. Although
2291 Eros is an NEO with a likely LL chondrite composition, it does not appear to be a lost member of
2292 the Flora family. The origin of Eros is currently an unsolved problem (Sec. 5.7).

2293 Itokawa. Itokawa is a small S-type NEO that was likely to have once part of the Flora
2294 family (see Gaspra above). If we limit our analysis to its largest craters, we find that Itokawa's
2295 crater spatial densities match those found on Gaspra, another Flora family member. Moreover, if
2296 these large craters formed with $f \sim 10$, they suggest that components of Itokawa's crater history
2297 tell the story of the billion-year interval between the formation of the Flora family and the present
2298 day (Sec. 6.1). On the other hand, the crater retention age based on the largest craters could be
2299 young if $f \gg 10$.

2300 Toutatis. Based on the results of dynamical models and spectroscopic interpretation, we
2301 predict that the 2.5-km S-type NEO Toutatis was once part of the Koronis family. We find that
2302 the crater spatial densities of its largest craters match trends in the SFD of Ida, a Koronis family

2303 member. If these large craters formed with $f \sim 10$, components of the observed surface on Toutatis
2304 could be as old as the Koronis family-forming event (Sec. 6.2).

2305 Bennu and Ryugu. Bennu and Ryugu are 0.5- and 0.9-km carbonaceous chondrite
2306 asteroids, respectively. The crater spatial densities of their largest craters were found to be
2307 comparable to the crater SFD found on Gaspra, whose surface is the order of 1.3 Ga old. If these
2308 large craters formed with $f \sim 10$, both worlds could have observed surface features as old as the
2309 predicted source families for these worlds, Eulalia and New Polana, which are nearly 1 Ga old
2310 (Sec. 6.3).

2311 The largest craters on Itokawa, Toutatis, Bennu, and Ryugu yield ages of $\sim 1, 2.5, 1,$ and 1
2312 Ga, respectively, provided $f \sim 10$. There are some reasons to think it could be illusionary, with the
2313 reality being that the largest craters on these worlds formed with $f \gg 10$, but we are unable to
2314 dismiss these ancient ages out of hand.

2315 If the largest craters on these worlds are indeed old, all four of these NEOs, and in fact
2316 most NEOs, are probably likely the fortunate survivors of collisional evolution within the main
2317 belt region. Tracking the collisional and dynamical evolution of individual main belt bodies across
2318 the main belt, and accounting for the possibility of a collisional cascade that allows breakup event
2319 to produce daughter fragments, can potentially be simulated by the next generation of numerical
2320 models (Sec. 7).

2321 On the other hand, if the largest craters on these four NEOs are instead relatively young, f
2322 either had to go from a value of 10 for Eros/Gaspra/larger bodies to $f \gg 10$ for only slightly smaller
2323 bodies or it had to change on the surfaces of the four NEOs themselves. In the latter case, the
2324 evidence for this change would be found by modeling the SFD of the smaller craters that have
2325 been strongly affected by crater erasure. Finding evidence of how and why this happens could
2326 lead us to a better understanding of the physical nature of asteroids and how they are affected by
2327 collisions (Sec. 7).

2328

2329 **Acknowledgements**

2330

2331 We thank Kevin Housen for his comments that helped us to better understand the nature of
2332 how asteroids might disrupt as they are spun up to high speeds, as well as the constructive
2333 comments from our referees. We also thank Peter Thomas and Mark Robinson for the use of their
2334 Eros crater database. The data generated in this work are reported in the text and figures. The work
2335 in this paper was supported by NASA's OSIRIS-REx mission through NASA Contract
2336 NNM10AA11C issued through the New Frontiers Program and grant no. 80NSSC18K0226 as part
2337 of the OSIRIS-REx Participating Scientist Program. The work of David Vokrouhlický was
2338 partially funded by a grant 18-06083S of the Czech Science Foundation.

2339

2340

2341

2342 **References**

- 2343 Aljbaae, S., Carruba, V., Masiero, J.R., Domingos, R.C., Huaman, M., 2017. The Maria Asteroid
2344 family. *Mon. Not. Roy. Astron. Soc.* 471, 4820-4826.
- 2345
2346 Arakawa, M. et al., 2020. An artificial impact on the asteroid 162173 Ryugu formed a crater in the
2347 gravity-dominated regime. *Science* 10.1126/science.aaz1701
- 2348
2349 Barnouin, O.S., et al., 2019. Shape of (101955) Bennu indicative of a rubble pile with internal
2350 stiffness. *Nature Geoscience* 12, 247-252.
- 2351
2352 Belton, M.J.S., et al., 1992. Galileo encounter with 951 Gaspra: First pictures of an asteroid.
2353 *Science* 257, 1647-1652.
- 2354
2355 Belton, M.J.S., et al., 1996. Galileo's encounter with 243 Ida: An overview of the imaging
2356 experiment. *Icarus* 120, 1-19.
- 2357
2358 Benz, W., Asphaug, E., 1999. Catastrophic disruptions revisited. *Icarus* 142, 5–20.
- 2359
2360 Birlan, M., 2002. Dynamic and physical considerations on the asteroids density. *Earth, Moon and*
2361 *Planets* 88, 1-10.
- 2362
2363 Binzel, R. P., and 22 colleagues 2019. Compositional distributions and evolutionary processes for the
2364 near-Earth object population: Results from the MIT-Hawaii Near-Earth Object Spectroscopic Survey
2365 (MITHNEOS). *Icarus* 324, 41-76.
- 2366
2367 Bottke, W.F., Nolan, M.C., Kolvoord, R.A., Greenberg, R., 1994. Velocity distribution among
2368 colliding asteroids. *Icarus* 107, 255-268.
- 2369
2370 Bottke, W.F., Nolan, M.C., Melosh, H.J., Vickery, A.M., Greenberg, R., 1996. Origin of the
2371 Spacewatch small Earth-approaching asteroids. *Icarus* 122, 406-427.
- 2372
2373 Bottke, W.F., Morbidelli, A., Jedicke, R., Petit, J.-M., Levison, H., Michel, P., Metcalfe, T. S., 2002.
2374 Debaised orbital and size distributions of the near-Earth objects. *Icarus* 156, 399-433.
- 2375
2376 Bottke, W.F., Vokrouhlický, D., Brož, M., Nesvorný, D., Morbidelli, A., 2001. Dynamical spreading
2377 of asteroid families via the Yarkovsky effect: The Koronis family and beyond. *Science* 294, 1693-
2378 1696.
- 2379
2380 Bottke, W.F., Durda, D.D., Nesvorný, D., Jedicke, R., Morbidelli, A., Vokrouhlický, D., Levison, H.,
2381 2005a. The fossilized size distribution of the main asteroid belt. *Icarus* 175, 111-140.
- 2382
2383 Bottke, W.F., Durda, D.D., Nesvorný, D., Jedicke, R., Morbidelli, A., Vokrouhlický, D., Levison, H.
2384 F., 2005b. Linking the collisional history of the main asteroid belt to its dynamical excitation and
2385 depletion. *Icarus* 179, 63-94.
- 2386
2387 Bottke, W.F., Vokrouhlický, D., Rubincam, D.P., Nesvorný, D., 2006a. The Yarkovsky and YORP
2388 effects: Implications for asteroid dynamics. *Ann. Rev. Earth Planet. Sci.* 34, 157-191.

2388
2389 Bottke, W.F., Nesvorný, D., Grimm, R.E., Morbidelli, A., O'Brien, D.P., 2006b. Iron meteorites
2390 as remnants of planetesimals formed in the terrestrial planet region. *Nature* 439, 821–824.
2391
2392 Bottke, W. F. 2014. On the Origin and Evolution of Vesta and the V-Type Asteroids. *Vesta in the*
2393 *Light of Dawn: First Exploration of a Protoplanet in the Asteroid Belt*, 2024.
2394
2395 Bottke, W.F., Brož, M., O'Brien, D.P., Campo Bagatin, A., Morbidelli, A., Marchi, S., 2015a. The
2396 collisional evolution of the asteroid belt. In *Asteroids IV*, ed. P. Michel, F. DeMeo, and W. F.
2397 Bottke (Tucson, AZ, U. Arizona Press), 701-724.
2398
2399 Bottke, W.F., et al., 2015b. In search of the source of asteroid (101955) Bennu: Applications of
the stochastic YORP model. *Icarus* 247, 191-271.
2400
2401 Brož, M., Morbidelli, A., Bottke, W.F., Rozehnal, J., Vokrouhlický, D., Nesvorný, D., 2013.
2402 Constraining the cometary flux through the asteroid belt during the Late Heavy Bombardment.
Astron. Astrophys. 551, A117.
2403
2404 Bu, Y., et al., 2015. New insights of asteroid 4179 Toutatis using China Chang'e-2 close flyby
optical measurements. *Astron. J.* 149, 21.
2405
2406 Campins, H., Morbidelli, A., Tsiganis, K., de León, J., Licandro, J., Lauretta, D., 2010. The origin
of asteroid 101955 (1999 RQ36). *Astrophys. J.* 721, L53–L57.
2407
2408 Campins, H., et al., 2013. The origin of Asteroid 162173 (1999 JU3). *Astron. J.* 146, 26.
2409
2410 Chapman, C.R., 2002. Cratering on asteroids from Galileo and NEAR Shoemaker. (W. F. Bottke,
2411 A. Cellino, P. Paolicchi and R.P. Binzel, Eds). U. Arizona Press, 315-329.
2412
2413 Chapman, C.R., Veverka, J., Belton, M.J.S., Neukum, G., Morrison, D., 1996a. Cratering on
2414 Gaspra. *Icarus* 120, 231-245.
2415
2416 Chapman, C.R., et al., 1996b. Cratering on Ida. *Icarus* 120, 77-86.
2417
2418 Chapman, C.R., Merline, W.J., Thomas, P., 1999. Cratering on Mathilde. *Icarus* 140, 28-33.
2419
2420 Clement, M.S., Kaib, N.A., Raymond, S.N., Walsh, K.J., 2018. Mars' growth stunted by an early
2421 giant planet instability. *Icarus* 311, 340-356.
2422
2423 Cheng, A. F., et al., 2018. AIDA DART asteroid deflection test: Planetary defense and science
objectives *Planet. Sp. Sci.* 157, 104.
2424
2425 Chesley, S. R., et al., 2014. Orbit and bulk density of the OSIRIS-REx target Asteroid (101955)
2426 Bennu. *Icarus* 235, 5-22.
2427
2428 Coradini, A., et al., 2011. The surface composition and temperature of asteroid 21 Lutetia as
2429 observed by Rosetta/VIRTIS. *Science* 334, 492-494.
2430
2431
2432

- 2423 Davison, T. M., Raducan, S. D., Collins, G. S., Bland, P. A. 2019. Collisional Histories of Small
2424 Planetesimals: Implications for Constraining the Age of the Surface of OSIRIS-REx Target,
2425 Bennu. Lunar and Planetary Science Conference 2385.
- 2426 de Leon, J., Licandro, J., Serra-Ricart, M., Pinilla-Alonso, N., Campins, H. 2010. Observations,
2427 compositional, and physical characterization of near-Earth and Mars-crosser asteroids from a
2428 spectroscopic survey. *Astron. Astrophys.* 517, A23.
- 2429 Dohnanyi, J.S., 1969. Collisional model of asteroids and their debris. *J. Geophys. Res.* 74, 2531-
2430 2554.
- 2431 Dell’Oro, A., Marzari, F., Paolicchi, P., Vazani, V., 2001. Updated collisional probabilities of
2432 minor body populations. *Astron. Astrophys.* 366, 1053-1060.
- 2433 Dunn, T.L., Burbine, T.H., Bottke, W.F., Clark, J.P., 2013. Mineralogies and source regions of
2434 near-Earth asteroids. *Icarus* 222, 273-282.
- 2435 Durda, D.D., Greenberg, R., Jedicke, R., 1998. Collisional models and scaling laws: A new
2436 interpretation of the shape of the main-belt asteroid size distribution. *Icarus* 135, 431-440.
- 2437 Durda, D.D., Bottke, W.F., Nesvorný, D., Encke, B.L., Merline, W.J., Asphaug, E., Richardson,
2438 D.C., 2007. Size-frequency distributions of fragments from SPH/ N-body simulations of asteroid
2439 impacts: Comparison with observed asteroid families. *Icarus* 186, 498-516
- 2440 Ďurech, J., Hanuš, J., Alí-Lagoa, V., 2018. Asteroid models reconstructed from the Lowell
2441 Photometric Database and WISE data. *Astron. Astrophys.* 617, A57.
- 2442 Dykhuis, M., Molnar, L., Van Kooten, S.J., Greenberg, R., 2014. Defining the Flora family:
2443 Orbital properties, reflectance properties and age. *Icarus* 243, 111-128.
- 2444 Ernst, C. M., Barnouin, O. S., Daly, R. T., Small Body Mapping Tool Team. 2018. The Small
2445 Body Mapping Tool (SBMT) for Accessing, Visualizing, and Analyzing Spacecraft Data in Three
2446 Dimensions. Lunar and Planetary Science Conference 1043.
- 2447 Farinella, P., Davis, D.R., 1992. Collision rates and impact velocities in the main asteroid belt.
2448 *Icarus* 97, 111-123.
- 2449 Farnocchia, D., D. Vokrouhlický, A. Milani, F. Spoto, W. F. Bottke. 2013. Near Earth Asteroids
2450 with measurable Yarkovsky effect. *Icarus* 224, 1-13.
- 2451 Foley, C.N., Nittler, L.R., McCoy, T.J., Lim, L.F., Brown, M.R.M., Starr, R.D., Trombka, J.I.,
2452 2006. Minor element evidence that Asteroid 433 Eros is a space-weathered ordinary chondrite
2453 parent body. *Icarus* 184, 338-343.
- 2454 Fowler, J.W., Chillemi, J.R., 1992. IRAS asteroid data processing. In: Tedesco, E.F. (Ed.), The
2455 IRAS Minor Planet Survey, Tech. Report PLTR-92-2049. Phillips Laboratory, Hanscom Air Force
2456 Base, Massachusetts, pp. 17–43.
- 2457 Fu, R.R., et al., 2017. The interior structure of Ceres as revealed by surface topography. *Earth
2458 Planet. Sci. Lett.* 476, 153-164.

2459 Fujiwara, A., et al., 2006. The rubble-pile asteroid Itokawa as observed by Hayabusa. *Science* 312,
2460 1330-1334.

2461 Gladman, B.J., et al., 2009. On the asteroid belt's orbital and size distribution. *Icarus* 202, 104-
2462 118.

2463 Golubov, O., Scheeres, D.J., 2019. Systematic structure and sinks in the YORP effect. *Astron. J.*
2464 157, 105.

2465 Granvik, M., Morbidelli, A., Jedicke, R., Bolin, B., Bottke, W.F., Beshore, E., Vokrouhlický, D.,
2466 Delbó, M., Michel, P., 2016. Super-catastrophic disruption of asteroids at small perihelion
2467 distances. *Nature* 530, 303-306.

2468

2469 Granvik, M., Morbidelli, A., Jedicke, R., Bolin, B., Bottke, W.F., Vokrouhlický, D., Nesvorný,
2470 D., Michel, P., 2018. Debaised orbit and absolute-magnitude distributions for near-Earth objects.
2471 *Icarus* 312, 181-207.

2472

2473 Grott, M., et al., 2019. Low thermal conductivity boulder with high porosity identified on C-type
2474 asteroid (162173) Ryugu. *Nature Astronomy* 3, 971.

2475

2476 Greenberg, R., Nolan, M.C., Bottke, W.F., Kolvoord, R.A., Veverka, J., 1994. Collisional history
2477 of Gaspra. *Icarus* 107, 84-97.

2478

2479 Hanuš, J., et al., 2013. Asteroids' physical models from combined dense and sparse photometry
2480 and scaling of the YORP effect by the observed obliquity distribution. *Astron. Astrophys.* 551,
2481 A67.

2482

2483 Harris, A.W., D'Abramo, G., 2015. The population of near-Earth asteroids. *Icarus* 257, 302–312.
2484

2485 Hamilton, V.E., et al., 2019. Evidence for widespread hydrated minerals on asteroid (101955)
2486 Bennu. *Nature Astronomy* 3, 332-340.

2487

2488 Heinze, A. N., J. Trollo and S. Metchev. 2019. The Flux Distribution and Sky Density of 25th
2489 Magnitude Main Belt Asteroids. *Astron. J.*, in press. <https://arxiv.org/abs/1910.13015>

2490

2491 Hergenrother, C.W., et al., 2019. The operational environment and rotational acceleration of
2492 asteroid (101955) Bennu from OSIRIS-REx observations. *Nature Communications* 10, 1291.

2493

2494 Hiesinger, H., et al., 2012. How old are young lunar craters? *Journal of Geophysical Research*
2495 (Planets) 117, E00H10.

2496

2497 Hiesinger, H., et al., 2016. Cratering on Ceres: Implications for its crust and evolution. *Science*
2498 353, 4759.

2499

2500 Holsapple, K. A. 2007. Spin limits of Solar System bodies: From the small fast-rotators to 2003
2501 EL61. *Icarus* 187, 500.

2502

2503 Hopkins, M. D., S. J. Mojzsis, W. F. Bottke, O. Abramov. 2015. Micrometer-scale U–Pb age
2504 domains in eucrite zircons, impact re-setting, and the thermal history of the HED parent body.
2505 *Icarus* 245, 367-378.

2506

2507 Housen, K.J., Holsapple, K.A., 2003. Impact cratering on porous asteroids. *Icarus* 163, 102-119.
2508

2509 Holsapple, K. A., Housen, K. R. 2019. The catastrophic disruptions of asteroids: History, features,
2510 new constraints and interpretations. *Planet. Sp. Sci.* 179, 104724.

2511

2512 Housen, K.J., Holsapple, K.A., Voss, M.E., 1999. Compaction as the origin of the unusual craters
2513 on the asteroid Mathilde. *Nature* 402, 155-157.

2514

2515 Housen, K.J., Sweet, W.J., Holsapple, K.A., 2018. Impacts into porous asteroids. *Icarus* 300, 72-
2516 96.

2517

2518 Huang, J., et al., 2013. The Ginger-shaped asteroid 4179 Toutatis: New observations from a
2519 successful flyby of Chang'e-2. *Scientific Reports* 3, 3411.

2520

2521 Hudson, R.S., Ostro, S.J., Scheeres, D.J., 2003. High-resolution model of asteroid 4179 Toutatis.
2522 *Icarus* 161, 346-355.

2523

2524 Ivanov, B.A., Melosh, H.J., 2013. Two-dimensional numerical modeling of the Rheasilvia impact
2525 formation. *J. Geophys. Res.* 118, 1545-1557.

2526

2527 Ivanov, B.A., Neukum, G., Wagner, R., 2001. Size-frequency distributions of planetary impact
2528 craters and asteroids. *Astrophysics and Space Science Library* 261, 1-34.

2529

2530 Ivanov, B. A., G. Neukum, W. F. Bottke, and W. K. Hartmann. 2002. The comparison of size-
2531 frequency distributions of impact craters and asteroids and the planetary cratering rate. In
2532 *Asteroids III* (W. F. Bottke, A. Cellino, P. Paolicchi, R. Binzel, Eds). U. Arizona Press, 89-101.

2533

2534 Ivezić, Ž., et al., 2001. Solar system objects observed in the Sloan Digital Sky Survey
2535 commissioning data. *Astron. J.* 122, 2749-2784.

2536

2537 Jacobson, S.A., Marzari, F., Rossi, A., Scheeres, D.J., Davis, D.R., 2014. Effect of rotational
2538 disruption on the size frequency distribution of the main belt asteroid population. *Mon. Not. R.*
2539 *Astron. Soc.* 439, L95-L99.

2540

2541 Jedicke, R., Larsen, J., Spahr, T., 2002. Observational selection effects in asteroid surveys. In
2542 *Asteroids III*, ed. W. F. Bottke, A. Cellino, P. Paolicchi and R.P. Binzel (Tucson, AZ, U. Arizona
2543 Press), 71-87.

2544

2545 Jewitt D., Hsieh H. H., Agarwal J. 2015. The active asteroids. In *Asteroids III*, ed. W. F. Bottke,
2546 A. Cellino, P. Paolicchi and R.P. Binzel (Tucson, AZ, U. Arizona Press), 221–241.

2547

2548 Jiang, Y., Ji, J., Huang, J., Marchi, S., Li, Y., Ip, W.-H., 2015. Boulders on asteroid Toutatis as
2549 observed by Chang'e-2. *Scientific Reports* 5, 16029.
2550

2551 Jutzi, M., Asphaug, E., Gillet, P., Barrat, J.-A., Benz, W., 2013. The structure of the asteroid 4 Vesta
2552 as revealed by models of planet-scale collisions. *Nature* 494, 207-210.
2553

2554 Kessler, D.J., 1981. Derivation of the collision probability between orbiting objects: the lifetimes of
2555 Jupiter's outer moons. *Icarus* 48, 39-48.
2556

2557 Knežević, Z., Lemaitre, A., Milani, A. 2002. The Determination of Asteroid Proper Elements. . In
2558 *Asteroids III*, ed. W. F. Bottke, A. Cellino, P. Paolicchi and R.P. Binzel (Tucson, AZ, U. Arizona
2559 Press), 603.
2560

2561 La Spina, A., Paolicchi, P., Kryszczyńska, A., Pravec, P., 2004. Retrograde spins of near-Earth
2562 asteroids from the Yarkovsky effect. *Nature* 428, 400-401.
2563

2564 Lauretta, D.S., et al., 2019. The unexpected surface of asteroid (101955) Bennu. *Nature* 568, 55-
2565 60.
2566

2567 Levison, H.F., Bottke, W.F., Gounelle, M., Morbidelli, A., Nesvorný, D., Tsiganis, K., 2009.
2568 Contamination of the asteroid belt by primordial trans-Neptunian objects. *Nature* 460, 364-366.
2569

2570 Lindsay, F. N., Delaney, J. S., Herzog, G.~F., Turrin, B.~D., Park, J., Swisher, C. C. 2015.
2571 Rheasilvia provenance of the Kapoeta howardite inferred from 1 Ga $^{40}\text{Ar}/^{39}\text{Ar}$ feldspar ages.
2572 *Earth and Planetary Science Letters* 413, 208.
2573

2574 Lowry, S., et al., 2014. The internal structure of asteroid (25143) Itokawa as revealed by detection
2575 of YORP spin-up. *Astron. Astrophys.* 562, A48.
2576

2577 Manley, S.P., Migliorini, F., Bailey, M.E., 1998. An algorithm for determining collision
2578 probabilities between small solar system bodies. *Astron. Astrophys. Supp.* 133, 437-444.
2579

2580 Marchi, S., et al., 2009. A New Chronology for the Moon and Mercury. *Astron. J.* 137, 4936.
2581

2582 Marchi, S., et al., 2012a. The violent collisional history of asteroid 4 Vesta. *Science* 336, 690-693.
2583

2584 Marchi, S., et al., 2012b. The cratering history of asteroid (21) Lutetia. *Planet. Sp. Sci.* 66, 87-95.
2585

2586 Marchi, S., Bottke, W. F., O'Brien, D. P., Schenk, P., Mottola, S., De Sanctis, M. C., Kring, D. A.,
2587 Williams, D. A., Raymond, C. A., Russell, C. T. 2013a. Small crater populations on Vesta. *Planet.*
2588 *Space. Sci.*, 103, 96-103.
2589

2590 Marchi, S., W. F. Bottke, B. A. Cohen, K. Wünnemann, D. A. Kring, H. Y. McSween, M. C. De
2591 Sanctis, D. P. O'Brien, P. Schenk, C. A. Raymond, and C. T. Russell. 2013b. High-velocity
2592 collisions from the lunar cataclysm recorded in asteroidal meteorites. *Nature Geosciences* 6, 303-
2593 307.
2594

2595 Marchi, S., Chapman, C.R., Barnouin, O.S., Richardson, J.E., Vincent, J.-B., 2015. Cratering on
2596 asteroids. In *Asteroids IV* (P. Michel, F. DeMeo, and W. F. Bottke, Eds). U. Arizona Press, 725-744.
2597

2598 Marchi, S., et al., 2016. The missing large impact craters on Ceres. *Nature Communications* 7,
2599 12257.
2600

2601 Masiero, J., et al., 2011. Main belt asteroids with WISE/NEOWISE I: Preliminary albedos and
2602 diameters. *Astrophys. J.* 741, 68.
2603

2604 Masiero, J.R., DeMeo, F.E., Kasuga, T., Parker, A.H., 2015. Asteroid family physical properties.
2605 In *Asteroids IV* (P. Michel, F. DeMeo, and W. F. Bottke, Eds). U. Arizona Press, 323-340.
2606

2607 Marzari, F., Rossi, A., Scheeres, D.J., 2011. Combined effect of YORP and collisions on the
2608 rotation rate of small Main Belt asteroids. *Icarus* 214, 622-631.
2609

2610 Massironi, M., et al. 2012. Geological map and stratigraphy of asteroid 21 Lutetia. *Planet. Sp. Sci.*
2611 66, 125.
2612

2613 Mazrouei, S., et al., 2019. Earth and Moon impact flux increased at the end of the Paleozoic.
2614 *Science* 363, 253-257.
2615

2616 McSween, H.Y., et al., 2018. Carbonaceous chondrites as analogs for the composition and
2617 alteration of Ceres. *Meteor. Planet. Sci.* 53, 1793-1804.
2618

2619 Michel, P., Farinella, P., Froeschle, C. 1996. The orbital evolution of the asteroid Eros and
2620 implications for collision with the Earth. *Nature* 380, 689.
2621

2622 Michel, P., Kueppers, M., Cheng, A., Carnelli, I. 2018. The Hera Mission: European Component
2623 of the Asteroid Impact and Deflection Assessment (AIDA) Mission to a Binary Asteroid. *Lunar
2624 and Planetary Science Conference* 1144.
2625

2626 Michel, P., et al. 2019. Disruption and Reaccumulation as the Possible Origin of Ryugu and Bennu
2627 Top Shapes. *Lunar and Planetary Science Conference* 1659.
2628

2629 Minton, D., Richardson, J.E., Fassett, C.I., 2015. Re-examining the main asteroid belt as the
2630 primary source of ancient lunar craters. *Icarus* 247, 172-190.
2631

2632 Morbidelli, A., Nesvorný, D., 1999. Numerous weak resonances drive asteroids toward terrestrial
2633 planets orbits. *Icarus* 139, 295-308.
2634

2635 Morbidelli, A., et al., 2003. The shallow magnitude distribution of asteroid families. *Icarus* 162,
2636 328-336.
2637

2638 Morbidelli, A., et al., 2015. The Dynamical Evolution of the Asteroid Belt. In *Asteroids IV* (P.
2639 Michel, F. DeMeo, and W. F. Bottke, Eds). U. Arizona Press, 493-508.
2640

2641 Moyano-Cambero, C.E., Trigo-Rodríguez, J.M., Llorca, J., Fornasier, S., Barucci, M.A., Rimola,
2642 A., 2016. A plausible link between the asteroid 21 Lutetia and CH carbonaceous chondrites.
2643 Meteor. Planet. Sci. 51, 1795-1812.
2644

2645 Nakamura, T., et al., 2011. Itokawa dust particles: A direct link between S-type asteroids and
2646 ordinary chondrites. Science 333, 1113-1116.
2647

2648 Nesvorný, D., Roig, F., 2018. Dynamical origin and terrestrial impact flux of large near-Earth
2649 asteroids. Astron. J. 155, 42.
2650

2651 Nesvorný, D., Morbidelli, A., Vokrouhlický, D., Bottke, W.F., Brož, M., 2002. The Flora family:
2652 a case of the dynamically dispersed collisional swarm? Icarus 157, 155-172.
2653

2654 Nesvorný, D., Brož, M., Carruba, V., 2015. Identification and dynamical properties of asteroid
2655 families. In Asteroids IV (P. Michel, F. DeMeo, and W. F. Bottke, Eds). U. Arizona Press, 297-321.
2656

2657 Nesvorný, D., F. Roig, W. F. Bottke. 2017. Modeling the historical flux of planetary impactors. Astron.
2658 J. 153, 103.
2659

2660 Nesvorný, D., Vokrouhlický, D., Bottke, W.F., Levison, H.F., 2018. Evidence for very early
2661 migration of the Solar System planets from the Patroclus-Menoetius binary Jupiter Trojan. Nature
2662 Astronomy 2, 878-882.
2663

2664 Nolan, M.C. et al. (2019). Detection of Rotational Acceleration of Bennu Using HST Light Curve
2665 Observations. Geophys. Res. Lett. 46, 1956–1962.
2666

2667 O'Brien, D.P., Greenberg, R., 2003. Steady-state size distributions for collisional populations:
2668 Analytical solution with size dependent strength. Icarus, 164, 334–345.
2669

2670 O'Brien, D. P., Greenberg, R. 2005. The collisional and dynamical evolution of the main-belt and
2671 NEA size distributions. Icarus 178, 179.
2672

2673 O'Brien, D.P., Greenberg, R., Richardson, J.E., 2006. Craters on asteroids: Reconciling diverse
2674 impact records with a common impacting population. Icarus 183, 79-92.
2675

2676 Ostro, S., et al., 1995. Radar images of asteroid 4179 Toutatis. Science 270, 80-83.
2677

2678 Ostro, S., et al., 1999. Asteroid 4179 Toutatis: 1996 radar observations. Icarus 137, 122-139.
2679

2680 Öpik, E., 1951. Collision probability with the planets and the distribution of planetary matter. Proc.
2681 R. Irish Acad. 54, 165-199.
2682

2683 Park, J., et al., 2015. $^{40}\text{Ar}/^{39}\text{Ar}$ age of material returned from asteroid 25143 Itokawa. Meteor.
2684 Planet. Sci. 50, 2087-2098.
2685

2686 Park, R. S., and 13 colleagues 2016. A partially differentiated interior for (1) Ceres deduced from
2687 its gravity field and shape. Nature 537, 515-518

2688
2689 Parker, A.H., Ivezić, Ž., Jurić, M., Lupton, R., Sekora, M.D., Kowalski, A., 2008. The size
2690 distributions of asteroid families in the SDSS Moving Object Catalog 4. *Icarus* 198, 138-155.
2691
2692 Patzold, M., et al., 2011. Asteroid 21 Lutetia: Low mass, high density. *Science* 334, 491.
2693
2694 Penco U., Dell’Oro A., Paolicchi P., Campo Bagatin A., La Spina A., and Cellino A. 2004.
2695 Yarkovsky depletion and asteroid collisional evolution. *Planet. Sp. Sci.*, 52, 1087–1091.
2696
2697 Peplowski, P.N., 2016. The global elemental composition of 433 Eros: First results from the NEAR
2698 gamma-ray spectrometer orbital dataset. *Planet. Sp. Sci.* 134, 36-51.
2699
2700 Peplowski, P.N., Bazell, D., Evans, L.G., Goldsten, J.O., Lawrence, D.J., Nittler, L.R., 2015.
2701 Hydrogen and major element concentrations on 433 Eros: Evidence for an L- or LL-chondrite-like
2702 surface composition. *Meteor. Planet. Sci.* 50, 353-367.
2703
2704 Petit, J.-M., Durda, D.D., Greenberg, R., Hurford, T.A., Geissler, P.E., 1997. The long-term
2705 dynamics of Dactyl's orbit. *Icarus* 130, 177-197.
2706
2707 Pravec, P., Harris, A.W., 2007. Binary asteroid population. 1. Angular momentum content. *Icarus*
2708 190, 250-259.
2709
2710 Pravec, P., et al., 2008. Spin rate distribution of small asteroids. *Icarus* 197, 497-504.
2711
2712 Pravec, P., et al., 2010. Formation of asteroid pairs by rotational fission. *Nature* 466, 1085-1088.
2713
2714 Reddy, V., Sanchez, J.A., Gaffey, M.J., Abell, P.A., Le Corre, L., Hardersen, P.S., 2012.
2715 Composition of near-Earth asteroid (4179) Toutatis. *Icarus* 221, 1177-1179.
2716
2717 Reddy, V., et al., 2014. Chelyabinsk meteorite explains unusual spectral properties of Baptistina
2718 Asteroid Family. *Icarus* 237, 116-130.
2719
2720 Richardson, D.C., Leinhardt, Z.M., Melosh, H.J., Bottke, W.F., Asphaug, E., 2002. Gravitational
2721 aggregates: Evidence and evolution. In *Asteroids III*, ed. W. F. Bottke, A. Cellino, P. Paolicchi
2722 and R.P. Binzel (Tucson, AZ, U. Arizona Press), 501-515.
2723
2724 Richardson, J. E., Melosh, H. J., Greenberg, R. 2004. Impact-Induced Seismic Activity on Asteroid
2725 433 Eros: A Surface Modification Process. *Science* 306, 1526.
2726
2727 Richardson, J.E., Melosh, H.J., Greenberg, R.J., O'Brien, D.P., 2005. The global effects of impact-
2728 induced seismic activity on fractured asteroid surface morphology. *Icarus* 179, 325-349.
2729
2730 Robbins, S. J. 2014. New crater calibrations for the lunar crater-age chronology. *Earth and Planetary*
2731 *Science Letters* 403, 188.
2732
2733 Robinson, M.S., Thomas, P.C., Veverka, J., Murchie, S.L., Wilcox, B.B., 2002. The geology of 433
2734 Eros. *Meteor. Planet. Sci.* 37, 1651-1684.

2735
2736 Rubincam, D.P., 2000. Radiative spin-up and spin-down of small asteroids. *Icarus* 148, 2-11.
2737
2738 Runyon, K.D., Barnouin, O.S., 2015. Gaspra's craters: Implications for production functions and
2739 surface processes. 46th LPSC conference, p. 2869.
2740
2741 Russell, C.T., et al., 2012. Dawn at Vesta: Testing the protoplanetary paradigm. *Science* 336, 684-686.
2742
2743 Russell, C.T., et al., 2016. Dawn arrives at Ceres: Exploration of a small, volatile-rich world. *Science*
2744 353, 1008-1010.
2745
2746 Ryan, E.L., et al., 2015. The kilometer-sized Main Belt asteroid population revealed by Spitzer. *Astron.*
2747 *Astrophys.* 578, A42.
2748
2749 Scheeres, D.J., Britt, D., Carry, B., Holsapple, K.A., 2015. Asteroid interiors and morphology. In
2750 *Asteroids IV*, ed. P. Michel, F. DeMeo, and W. F. Bottke (Tucson, AZ, U. Arizona Press), 745-766.
2751
2752 Scheeres, D.J., et al., 2019. The dynamic geophysical environment of (101955) Bennu based on
2753 OSIRIS-REx measurements. *Nature Astronomy* 3, 352-361.
2754
2755 Schenk, P., et al., 2012. The geologically recent giant impact basins at Vesta's south pole. *Science*
2756 336, 694-697.
2757
2758 Schmedemann, N., et al., 2014. The cratering record, chronology and surface ages of (4) Vesta in
2759 comparison to smaller asteroids and the ages of HED meteorites. *Planet. Sp. Sci.* 103, 104-130.
2760
2761 Schmidt, R.M., Housen, K.R. 1987. Some recent advances in the scaling of impact and explosion
2762 cratering. *International Journal of Impact Engineering* 5, 543-560.
2763
2764 Ševeček, P., Brož, M., Jutzi, M. 2019. Impacts into rotating targets: angular momentum draining and
2765 efficient formation of synthetic families. *Astron. Astrophys.* 629, A122.
2766
2767 Shoemaker, E.M. 1962. Interpretation of lunar craters. In *Physics and Astronomy of the Moon* (Z.
2768 Kopal, ed.), pp. 283-359. Academic Press, New York, New York.
2769
2770 Sierks, H., et al. 2011. Images of Asteroid 21 Lutetia: A Remnant Planetesimal from the Early Solar
2771 System. *Science* 334, 487.
2772
2773 Spoto, F., Milani, A., Knežević, Z., 2015. Asteroid family ages. *Icarus* 257, 275-289.
2774
2775 Statler, T.S., 2009. Extreme sensitivity of the YORP effect to small-scale topography. *Icarus* 202, 502–
2776 513.
2777
2778 Stokes, G., et al., 2017. Update to Determine the Feasibility of Enhancing the Search and
2779 Characterization of NEOs. Report of the Near-Earth Object Science Definition Team. Prepared at the
2780 request of NASA, Science Mission Directorate, Planetary Science Division, September 2017.
2781

2782 Takahashi, Yu., Busch, M.W., Scheeres, D.J., 2013. Spin state and moment of inertia characterization
2783 of 4179 Toutatis. *Astron. J.* 146, 95.
2784

2785 Tatsumi, E., Sugita, S., 2018. Cratering efficiency on coarse-grain targets: Implications for the
2786 dynamical evolution of asteroid 25143 Itokawa. *Icarus* 300, 227-248.
2787

2788 Terada, K., et al., 2018. Thermal and impact histories of 25143 Itokawa recorded in Hayabusa
2789 particles. *Scientific Reports* 8, 11806.
2790

2791 Thomas, P. C., Robinson, M. S. 2005. Seismic resurfacing by a single impact on the asteroid 433
2792 Eros. *Nature* 436, 366.
2793

2794 Thomas, P. C., et al., 1994. The shape of Gaspra. *Icarus* 107, 23.
2795

2796 Thomas, P. C., et al., 1996. The shape of Ida. *Icarus* 120, 20.
2797

2798 Thomas, P. C., et al., 1999. Mathilde: Size, shape, and geology. *Icarus* 140, 17.
2799

2800 Thomas, P. C., et al., 2002. Eros: Shape, topography, and slope processes. *Icarus* 155, 18.
2801

2802 Thomas, N., et al. 2012. The geomorphology of (21) Lutetia: Results from the OSIRIS imaging
2803 system onboard ESA's Rosetta spacecraft. *Planet. Sp. Sci.* 66, 96.
2804

2805 Trombka, J.I., et al., 2000. The elemental composition of asteroid 433 Eros: Results of the NEAR-
2806 Shoemaker X-ray spectrometer. *Science* 289, 2101-2105.
2807

2808 Veverka, J.D., 1998. Main belt asteroid collision probabilities and impact velocities. *Icarus* 131,
2809 283-290.
2810

2811 Vernazza, P., et al. 2008. Compositional differences between meteorites and near-Earth asteroids.
2812 *Nature* 454, 858.
2813

2814 Vernazza, P., et al., 2014. Multiple and fast: The accretion of ordinary chondrite parent bodies.
2815 *Astrophys. J.* 791, 120.
2816

2817 Veverka, J., et al., 1997. NEAR's flyby of 253 Mathilde: Images of a C asteroid. *Science* 278,
2818 2109-2114.
2819

2820 Veverka, J., et al., 1999. NEAR encounter with asteroid 253 Mathilde: Overview. *Icarus* 140, 3-
2821 16.
2822

2823 Vokrouhlický, D., Nesvorný, D., Bottke, W.F., 2003. The vector alignments of asteroid spins by
2824 thermal torques. *Nature* 425, 147-151.
2825

2826 Vokrouhlický, D., Pokorný, P., Nesvorný, D., 2012. Öpik-type collision probability for high-
2827 inclination orbits. *Icarus* 219, 150-160.
2828

2829 Vokrouhlický, D., Bottke, W.F., Nesvorný, D., 2016. Capture of trans-Neptunian planetesimals in the
2830 main asteroid belt. *Astron. J.* 152, 39.
2831
2832 Vokrouhlický, D., Bottke, W.F., Nesvorný, D., 2017. Forming the Flora family: Implications for the
2833 near-Earth asteroid population and large terrestrial planet impactors. *Astron. J.* 153, 172
2834
2835 Vokrouhlický, D., Bottke, W.F., Chesley, S.R., Scheeres, D.J., Statler, T.S., 2015. The Yarkovsky and
2836 YORP effects. In *Asteroids IV*, ed. P. Michel, F. DeMeo, and W. F. Bottke (Tucson, AZ, U. Arizona
2837 Press), 509-532.
2838
2839 Walsh, K.J., Jacobson, S.A., 2015. Formation and evolution of binary asteroids. In *Asteroids IV*, ed.
2840 P. Michel, F. DeMeo, and W. F. Bottke (Tucson, AZ, U. Arizona Press), 375-393.
2841
2842 Walsh, K.J., Morbidelli, A., Raymond, S.N., O'Brien, D.P., Mandell, A.M., 2011. A low mass for
2843 Mars from Jupiter's early gas-driven migration. *Nature* 475, 206-209.
2844
2845 Walsh, K.J., Delbó, M., Bottke, W.F., Vokrouhlický, D., Lauretta, D.S., 2013. Introducing the Eulalia
2846 and new Polana asteroid families: Re-assessing primitive asteroid families in the inner Main Belt.
2847 *Icarus* 225, 283-297.
2848
2849 Walsh, K. J., et al., 2019. Craters, boulders and regolith of (101955) Bennu indicative of an old and
2850 dynamic surface. *Nature Geoscience* 12, 242-246.
2851
2852 Watanabe, S., et al. 2019. Hayabusa2 arrives at the carbonaceous asteroid 162173 Ryugu -- A spinning
2853 top-shaped rubble pile. *Science* 364, 268.
2854
2855 Wetherill, G., 1967. Collisions in the asteroid belt. *J. Geophys. Res.* 72, 2429-2444.
2856
2857 Williams, D.R., Wetherill, G.W., 1994. Size distribution of collisionally-evolved asteroidal
2858 populations. Analytical solution for self-similar collision cascades. *Icarus* 107, 117-128.
2859
2860 Williams, D., et al. 2018. The geology of the Kerwan quadrangle of dwarf planet Ceres: Investigating
2861 Ceres' oldest, largest impact basin. *Icarus* 316, 99-113.
2862
2863 Zappalà, V., Cellino, A., Dell'Oro, A., 2001. A search for the collisional parent bodies of large NEAs.
2864 *Icarus* 157, 280-296.
2865
2866 Zappalà, V., Cellino, A., Di Martino, M., Migliorini, F., Paolicchi, P., 1997. Maria's family: Physical
2867 structure and possible implications for the origin of giant NEAs. *Icarus* 129, 1-20.
2868
2869

2870
2871

Test #	D_{\min} (km)	α	β	% trials with $\psi_{SFD}^2 < 20$ and $\chi_{FAM}^2 > 2\sigma$	% trials with $\psi_{SFD}^2 < 10$ and $\chi_{FAM}^2 > 2\sigma$
1	0.2	-0.35	1.33	37	21
2	0.2	-0.385	1.35	36	30
3	0.2	-0.42	1.37	41	28
4	0.2	-0.455	1.405	47	26
5	0.21	-0.49	1.44	34	23
6	0.21	-0.535	1.465	33	22
7	0.2	-0.58	1.49	20	2
8	0.2	-0.625	1.53	12	0

2872 **Table 1.** The parameters used to define the eight Q_D^* asteroid disruption functions tested in this
 2873 paper, as well as how they fared against constraints. The parameters in columns 2 to 4 are D_{\min} ,
 2874 defined as the location of the minimum Q_D^* value ($Q_{D_{\min}}^*$), and the two variables α and β , which
 2875 are applied in Eq. 5, 6, and 7 to derive Q_D^* . Columns 5 and 6 describe the number of trials out of
 2876 100 test runs that match both of our main belt constraints. The metric ψ_{SFD}^2 , defined by Eq. 4,
 2877 describes how well the model main belt SFD compares to the observed main belt SFD. The metric
 2878 χ_{FAM}^2 is a χ^2 test where the fit between the model and observed families (for parent bodies $D_{\text{ast}} >$
 2879 100 km) is better than 2σ (i.e., probability $>5\%$).

2880

Asteroid/Region Name	Effective surface gravity (cm s^{-2})	Strength to gravity transition diameter D_{SG} (km)	Reference
Ceres (Kerwan Basin)	28	1.75	Hiesinger et al. (2016)
Vesta (Rheasilvia Basin)	25	1.94	Russell et al. (2012)
Lutetia (Achaia Region)	4.7	49	Patzold et al. (2011)
Mathilde	0.96	51	Thomas et al. (1999)
Ida	0.7	69	Thomas et al. (1996)
Gaspra	0.5	97	Thomas et al. (1994)
Eros	0.4	120	Thomas et al. (2002)

2881 **Table 2.** Compilation of asteroid surface gravities and strength to gravity transition diameter value
 2882 used for the crater scaling laws in this paper.

2883

2884

2885

2886

2887

2888

Ast. #	Asteroid/Region Name	Proper a (AU)	Proper e	Proper i (deg)	N_{cross}	P_i (10^{-18} km 2 yr $^{-1}$)	V_{imp} (km s $^{-1}$)
1	Ceres (Kerwan Basin)	2.7670963	0.1161977	9.6474113	642 (out of 681)	3.455	4.860
4	Vesta (Rheasilvia Basin)	2.3615127	0.0987580	6.3923416	372 (out of 681)	2.878	4.710
21	Lutetia (Achaia Region)	2.4352603	0.1292457	2.1461887	491 (out of 681)	3.763	4.379
243	Ida	2.8616140	0.0456271	2.0883834	582 (out of 682)	4.037	3.720
253	Mathilde	2.6477821	0.2189155	6.5350556	666 (out of 681)	3.723	5.237
951	Gaspra	2.2097211	0.1475680	5.0786877	327 (out of 682)	2.635	4.924
2867	Steins	2.3635361	0.1082622	9.3526096	392 (out of 682)	2.785	5.154

2889 **Table 3.** The intrinsic collision probabilities (P_i) and impact velocities (V_{imp}) for main belt
2890 asteroids observed by spacecraft. The first column is the asteroid number. The second column is
2891 the name of the asteroid, with the name of the region examined in parentheses where applicable.
2892 The proper semimajor axis a , eccentricity e , and inclination i values were taken from the Asteroids
2893 Dynamic Site AstDyS (<https://newton.spacedys.com/astdys/>). The comparison population of 682
2894 asteroids with $D_{\text{ast}} \geq 50$ km was taken from Farinella and Davis (1992), and N_{cross} describes the
2895 number of these bodies on crossing orbits with the target asteroid.

2896

2897

Asteroid Name	M (# Crater Data Points)	Empirical Fit: Best Fit SFD	χ_{MB}^2 Best Fit	SFDs That Fit Within 1σ	HH Scaling: Best Fit SFD	χ_{MA}^2 Best Fit	SFDs That Fit Within 1σ	Ivanov Scaling: Best Fit SFD	χ_{IV}^2 Best Fit	SFDs That Fit Within 1σ
Ceres-KB	22	8	2.84	6-7	8	4.61	7	8	9.44	-
Vesta-RB	48	5	22.32	4,6-8	7	19.34	6	8	70.51	-
Lutetia-AR	17	7	1.97	3-6, 8	7	2.24	5-6, 8	8	4.00	7
Mathilde	12	2	2.67	1,3-6	4	2.60	1-3,5	8	4.98	3-7
Ida	16	8	1.17	1-7	6	1.39	1-5, 7-8	8	1.93	1-7
Gaspra	14	1	1.94	2-8	1	1.93	2-8	1	1.85	2-8
Eros	12	2	3.72	1,3-8	1	3.85	2-7	8	2.27	1-8

2898 **Table 4.** Compilation of results where model and observed crater SFDs were compared to one
2899 another. The index numbers 1-8 corresponds to the eight Q_D^* asteroid disruption functions and eight
2900 model main belt SFDs (Figs. 1-2; Table 1). The results are given for the three different crater
2901 scaling laws discussed in Sec. 2.5. The second column is M , the number of crater data points on
2902 the asteroid/region in question (see Eq. 14).

2903

2904

2905

2906

2907
2908
2909
2910

Asteroid Name	Empirical fit factor f	Empirical Fit: Age for Best Fit (Ga)	HH Scaling: Age for Best Fit (Ga)	Ivanov Scaling: Age for Best Fit (Ga)
Ceres-KB	8.20 [-1.40, +1.00]	0.91 [-0.17, +0.17]	0.70 [-0.02, +0.03]	0.47 [-0.01, +0.02]
Vesta-RB	9.90 [-1.40, +1.00]	0.85 [-0.23, +0.24]	1.24 [-0.06, +0.06]	0.37 [-0.02, +0.01]
Lutetia-AR	10.30 [-4.90, +3.60]	2.57 [-2.02, +1.64]	3.07 [-0.41, +0.41]	1.24 [-0.16, +0.16]
Mathilde	10.00 [-3.40, +1.90]	3.70 [-1.30, +1.52]	2.85 [-0.50, +0.50]	0.85 [-0.15, +0.15]
Ida	10.90 [-2.70, +2.90]	2.52 [-1.98, +0.94]	2.91 [-0.43, +0.43]	1.17 [-0.17, +0.16]
Gaspra	10.10 [-3.70, +3.80]	0.74 [-1.74, +0.41]	0.73 [-0.07, +0.07]	0.17 [-0.01, +0.01]
Eros	10.90 [-3.00, +3.00]	2.03 [-2.01, +0.86]	2.10 [-0.29, +0.28]	1.40 [-0.19, +0.18]

2911 **Table 5.** Best fit empirical scaling law fit values for f (Eq. 12) and crater retention ages for different
2912 main belt asteroid surfaces using different crater scaling laws. The ages in the last three columns
2913 are given in units of billions of years (Ga). These values correspond to the best fit cases, but other
2914 fits may be within 1σ of these results (Table 4). The main text gives the preferred values, which
2915 take into account additional constraints.

2916

Asteroid/Region Name	Tax	Asteroid Size (km)	Family	Comments	Sec.
Ceres (Kerwan Basin)	Cb	965.2 × 961.2 × 891.2	None	Probable crater retention age of ~0.8-0.9 Ga based on model fit with craters larger than 2 km	5.2
Vesta (Rheasilvia Basin)	V	572.6 × 557.2 × 446.4	Vesta	Probable crater retention age < 1.3 Ga. Age of ~1 Ga consistent with sample, family constraints	5.1
Lutetia (Achaia Region)	M	121 × 101 × 75	None	Probable crater retention age ~2.5-3.5 Ga, but surface could be as old as main belt itself	5.3
Mathilde	C	66 × 48 × 46	None	Probable crater retention age between ~2.2 Ga and age of the main belt itself.	5.4
Ida	S	59.8 × 25.4 × 18.6	Koronis	Probable crater retention age of ~2-3 Ga. Consistent with likely dynamical age of Koronis family.	5.5
Gaspra	S	18.2 × 10.5 × 8.9	Flora	Probable crater retention age of ~1.3 Ga. Consistent with likely dynamical age of Flora family and sample ages from Itokawa.	5.6
Eros	S	34.4 × 11.2 × 11.2	Unknown	Probable crater retention age between ~2.3 to ~3.8 Ga. No family has yet been identified as source.	5.7
Itokawa	S	0.535 × 0.294 × 0.209	Flora	Crater retention age of largest craters matches those of Gaspra and Itokawa sample ages, provided $f \sim 10$.	6.1
Toutatis	S	4.354 × 1.835 × 2.216	Koronis	Crater retention age of largest craters matches those of Ida and likely dynamical age of the Koronis family, provided $f \sim 10$.	6.2
Ryugu	Cb	1.04 × 1.02 × 0.88	Eulalia or New Polana	Crater retention age of largest craters ~ 1 Ga, provided $f \sim 10$.	6.3
Bennu	B	0.506 × 0.492 × 0.457	Eulalia or New Polana	Crater retention age of largest craters ~ 1 Ga, provided $f \sim 10$.	6.3

2917

2918 **Table 6.** Summary of results for asteroids investigated in this paper. For each asteroid, we list the
2919 taxonomic type, its dimensions, its association with a given asteroid family, comments on its
2920 probable crater retention age and the age match with auxiliary constraints, and the section of the
2921 paper where the asteroid is discussed.

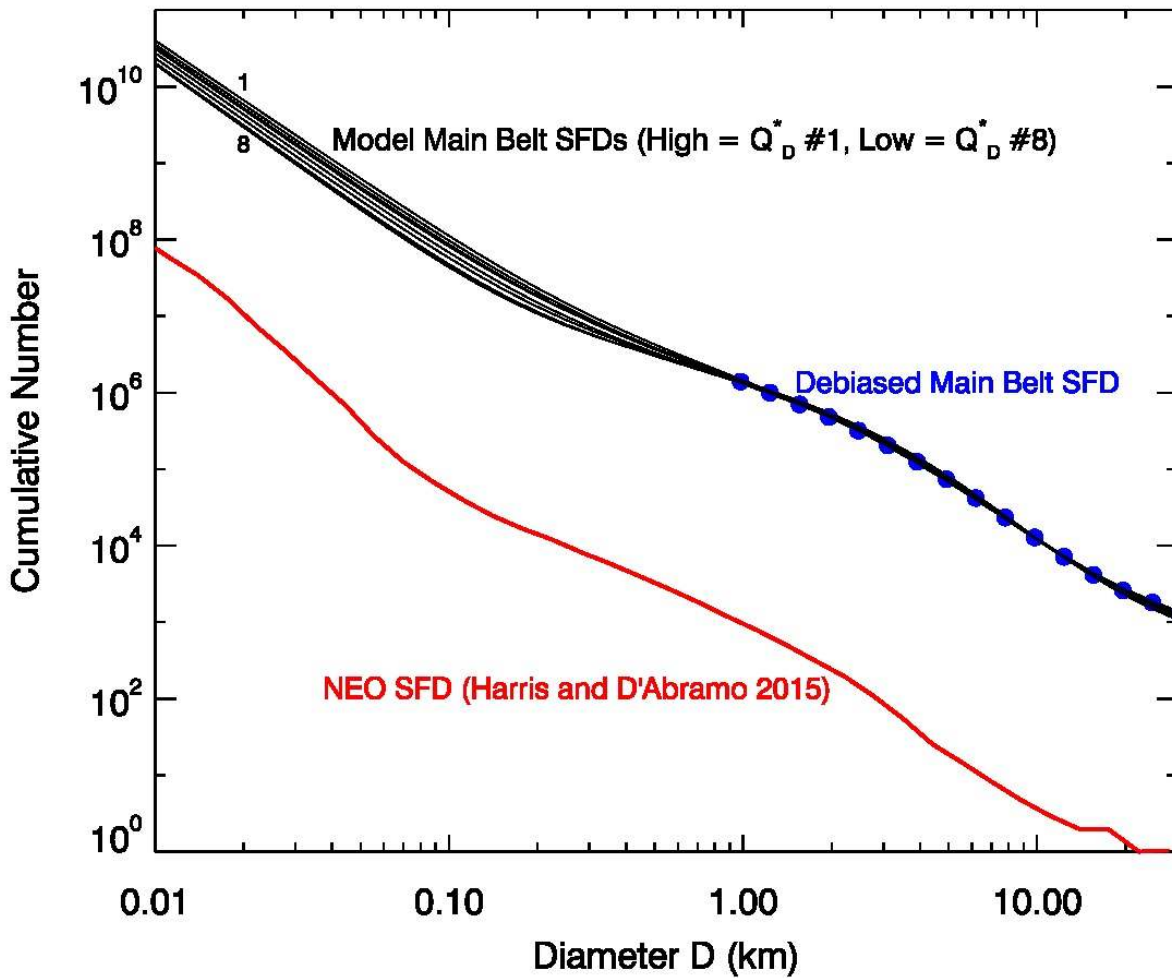


Figure 1. Collisional evolution model results for the main asteroid belt, based on the assumptions and model results of Bottke et al. (2005b). The model SFDs #1–8 are assigned an index number corresponding to the asteroid disruption laws Q_D^* #1–8 shown in Fig. 2 (i.e., SFD #1 was produced by Q_D^* #1, and so on). SFD #1 was designed to match the one used in Bottke et al. (2005b). The blue dots represent the debiased main belt SFD as discussed in Bottke et al. (2005a, b). For reference, the red line shows the NEO SFD as defined by Harris and D’Abramo (2015). As shown in Fig. 2, the higher index numbers correspond to lower minimum values for Q_D^* . This allows more asteroids to disrupt between $0.1 < D_{\text{ast}} < 1$ km, which in turn means the power law slope of the SFD becomes shallower in that range. The upturn in slope occurs at larger sizes for low index numbers (~ 0.5 km for #1) and smaller sizes for high index numbers (~ 0.2 km for #8).

2922
 2923
 2924
 2925

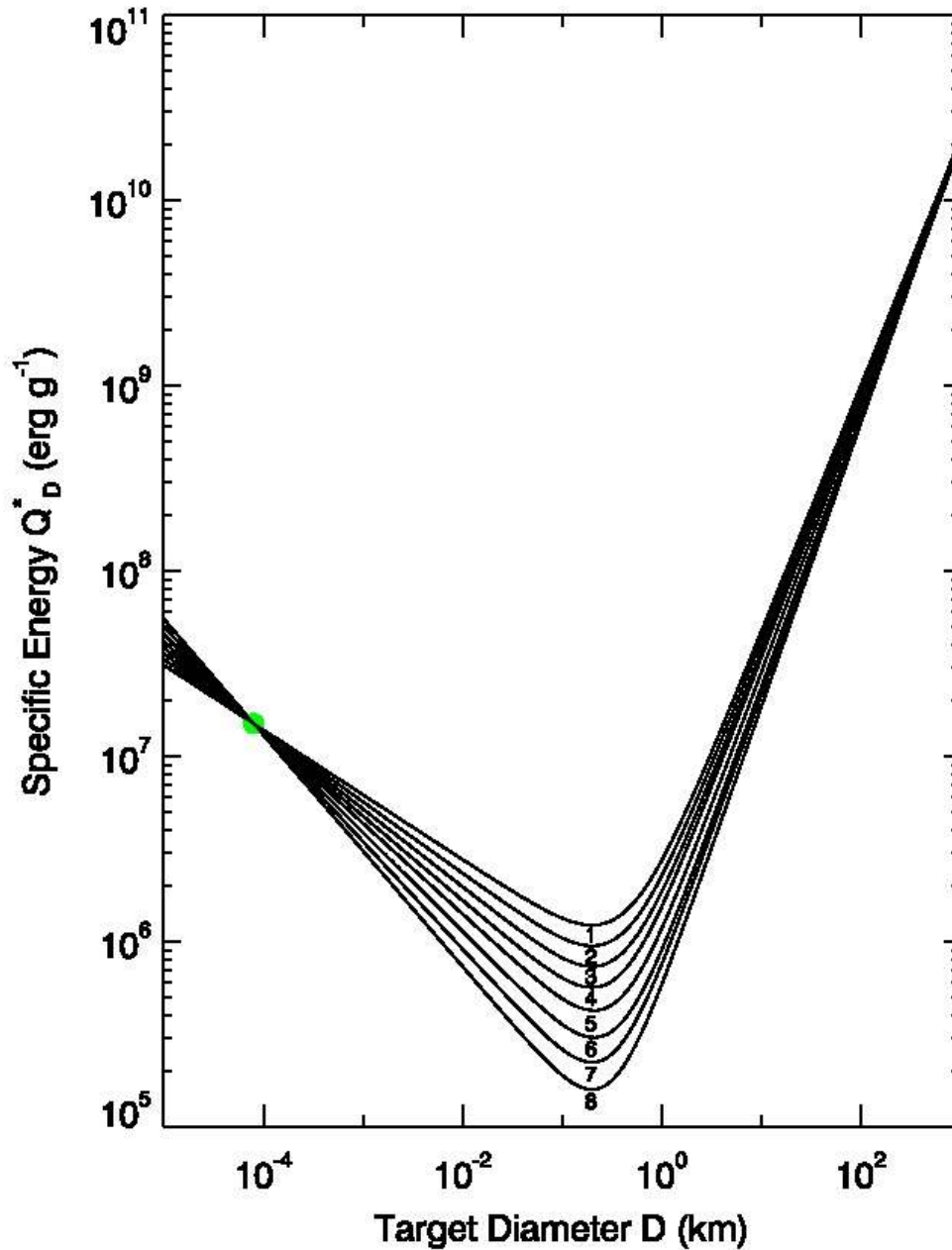


Figure 2. The asteroid disruption laws used in our collisional evolution model runs. Each disruption law Q_D^* is assigned an index number #1–8, and they produce the model main belt SFDs shown in Fig. 1 (i.e., SFD #1 was produced by Q_D^* #1, and so on). The parameters needed to generate the curves can be found in Table 1. Disruption law Q_D^* #1 matches the one used in Bottke et al. (2005b). The green dot is a normalization point determined from laboratory impact experiments. It is defined as $(Q_{D_{LAB}}^*, D_{LAB}) = (1.5 \times 10^7 \text{ erg g}^{-1}, 8 \text{ cm})$ (e.g., Durda et al., 1998). The minimum Q_D^* value ($Q_{D_{min}}^*$) for all of the functions is near $D_{min} = 0.2 \text{ km}$.

2926

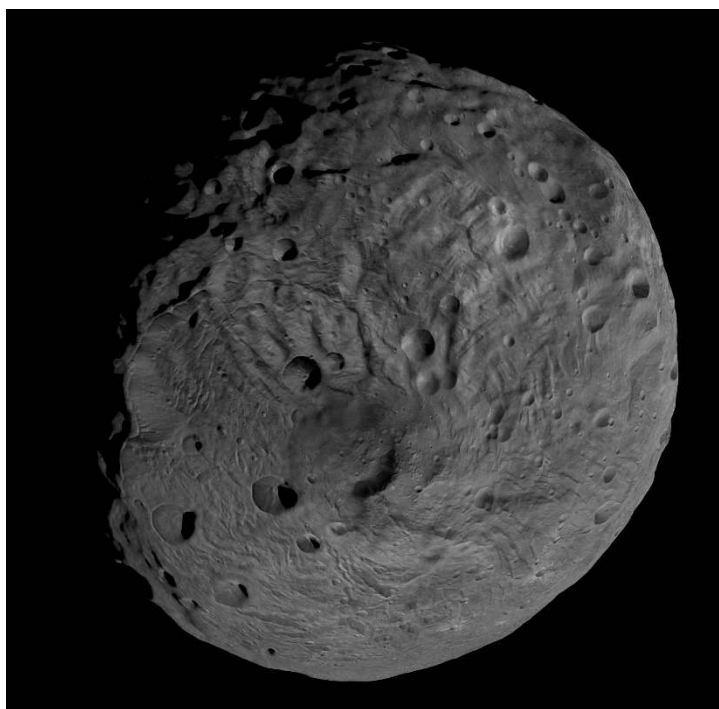


Figure 3. The south pole of the V-type asteroid Vesta, which is dominated by the 505-km diameter basin Rheasilvia. The image was obtained by the framing camera on NASA's Dawn spacecraft a distance of about 1,700 miles (2,700 km). The feature at the lower center of the image contains Rheasilvia's central peak. The image resolution is about 260 m per pixel. Craters between a few kilometers to tens of kilometers can be seen superposed on Rheasilvia's surface. Courtesy NASA/JPL-Caltech.

2927

2928

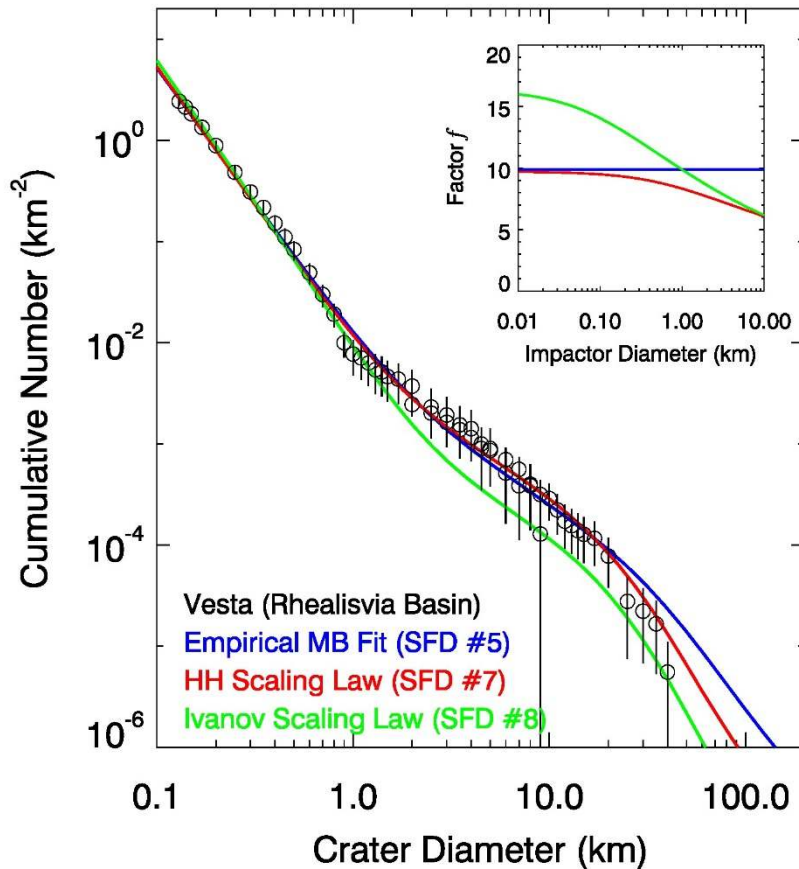


Figure 4. A comparison between the observed crater SFDs found on the floor and ejecta blanket of Vesta’s Rheasilvia basin and various crater models. The observed crater counts are from Marchi et al. (2015). The best fit model crater SFDs for three different crater scaling laws are shown with the colored lines: the main belt empirical fit in blue (Sec. 3.1.1), the HH crater scaling law fit in red (Sec. 3.1.2), and the Ivanov crater scaling law in green (Sec. 3.1.3). The numbers in parentheses correspond to the index number of the model main belt SFD applied to produce the model crater SFD (Fig. 1). See Sec. 3.1.1 for discussion of error bars. The inset figure shows the ratio $f = D_{\text{crater}} / D_{\text{ast}}$ for the different crater scaling laws as a function of the impacting asteroid’s diameter. The best fit model crater SFDs is the HH scaling fit, though the main belt empirical fit matches everything but the very largest craters. The Ivanov scaling fit produces a model crater SFD that is lower than the observed data for $D_{\text{crater}} > 1.5$ km.



Figure 5. The largest crater on C-type asteroid Ceres is Kerwan basin. It is ~284 km in diameter (Williams et al., 2017) and has a relaxed polygonal shape. The center of the basin is located at 10.8° south latitude and 123.9° east longitude. The image was taken during Dawn's Survey phase from an altitude of 4,400 km. Courtesy NASA/JPL-Caltech.

2930

2931

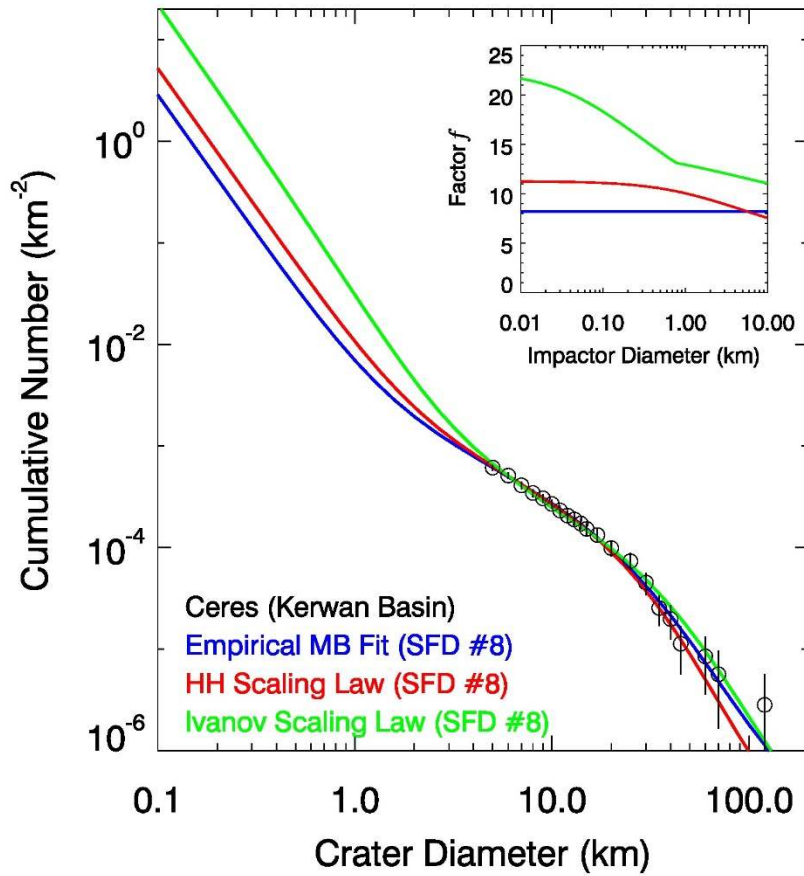


Figure 6. A comparison between the observed crater SFDs found on or near the Kerwan basin on Ceres and various crater models. The observed crater counts are from Hiesinger et al. (2016) with updates from this study. Plot components are as in Fig. 4. The best fit model crater SFD is the empirical main belt fit (Table 3). The predicted ages for Kerwan basin are $\sim 0.8\text{--}0.9$ Ga from the empirical main belt fit and the HH scaling law. The Ivanov scaling law predicts an age of ~ 0.5 Ga, smaller than the other two scaling laws because its f values in the inset figure are much higher.

2932
 2933
 2934
 2935
 2936
 2937
 2938

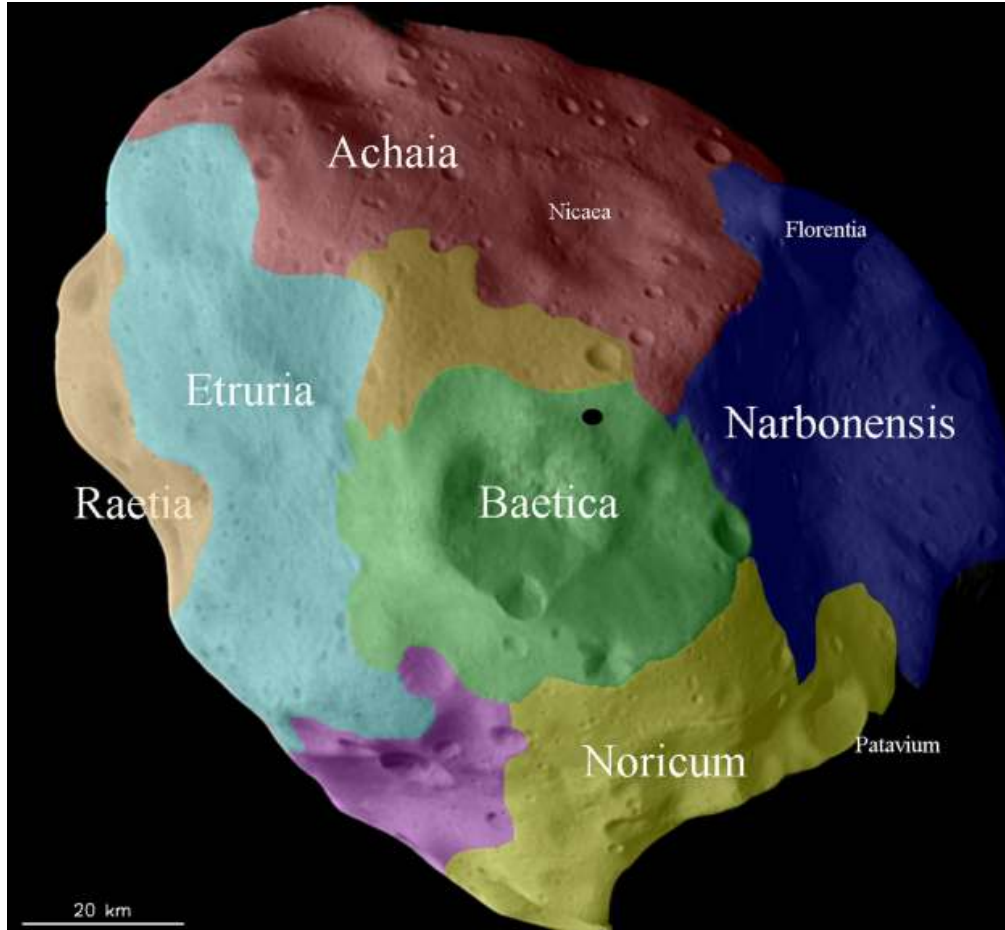


Figure 7. ESA’s Rosetta mission observed the M-type asteroid Lutetia during a flyby. The colors represent different regions of Lutetia as defined by geologic mapping. The oldest part of the asteroid, and the one investigated in the paper, is the heavily cratered Achaia region. This image was published in Thomas et al. (2012), who adapted it from Massironi et al., (2012). Copyright Elsevier.

2939

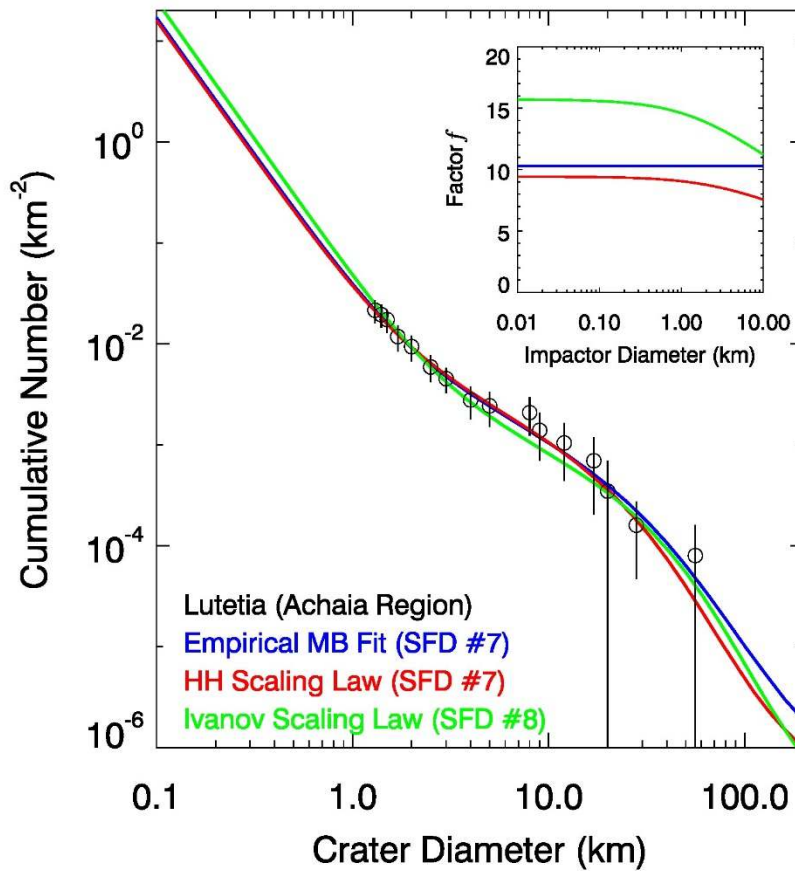


Figure 8. A comparison between the observed crater SFDs found on the Achaia region of Lutetia and various crater models. The observed crater counts are from Marchi et al. (2012b). Plot components are as in Fig. 4. The best fit model crater SFD is the empirical main belt fit and the HH scaling law (Table 3), both of which have f values near 9 or 10 for the majority of observed craters. The predicted mean age of the Achaia region from the empirical main belt fit and HH scaling law model is $\sim 2.5\text{--}3.5$ Ga.

2940
 2941
 2942
 2943
 2944



Figure 9. Mathilde is a large C-type main belt asteroid. The part of the asteroid shown is 59 by 47 km across. It was imaged by the NEAR spacecraft from a distance of 2,400 km. The surface exhibits many large craters, some which are partially shadowed. Courtesy NASA/JPL/JHUAPL.

2945
2946
2947
2948
2949
2950
2951
2952
2953
2954

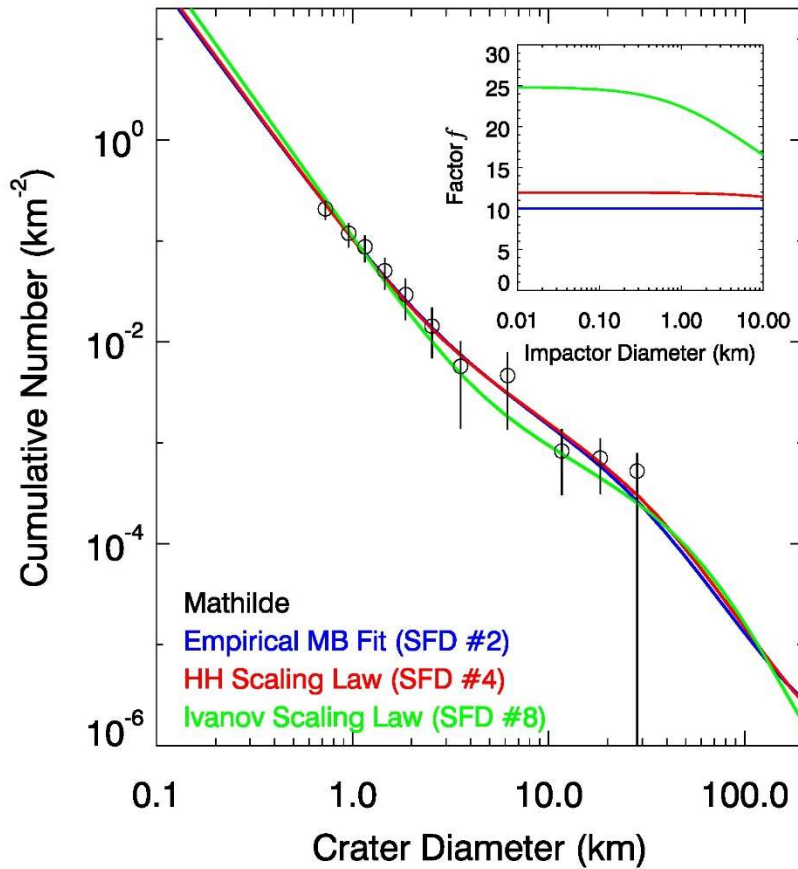


Figure 10. A comparison between the observed crater SFDs found on C-type asteroid Mathilde and various crater models. The observed crater counts are from O’Brien et al. (2005), who reformulated them from Chapman et al. (1996). Plot components are as in Fig. 4. The HH crater scaling law fit in red largely overlaps the main belt empirical fit in blue. The best fit model crater SFDs are the empirical main belt fit and the HH scaling law (Table 3). They both yield f values near 10–12 for the majority of observed craters and crater retention ages of ~ 2 to > 4 Ga. Many other SFDs fit the data within 1σ of the best fit cases (Table 3). If we apply higher-number SFDs to make our model crater SFD, the crater retention ages derived from the empirical main belt fit and the HH scaling law approach the age of the Solar System.

2955
 2956
 2957
 2958
 2959
 2960

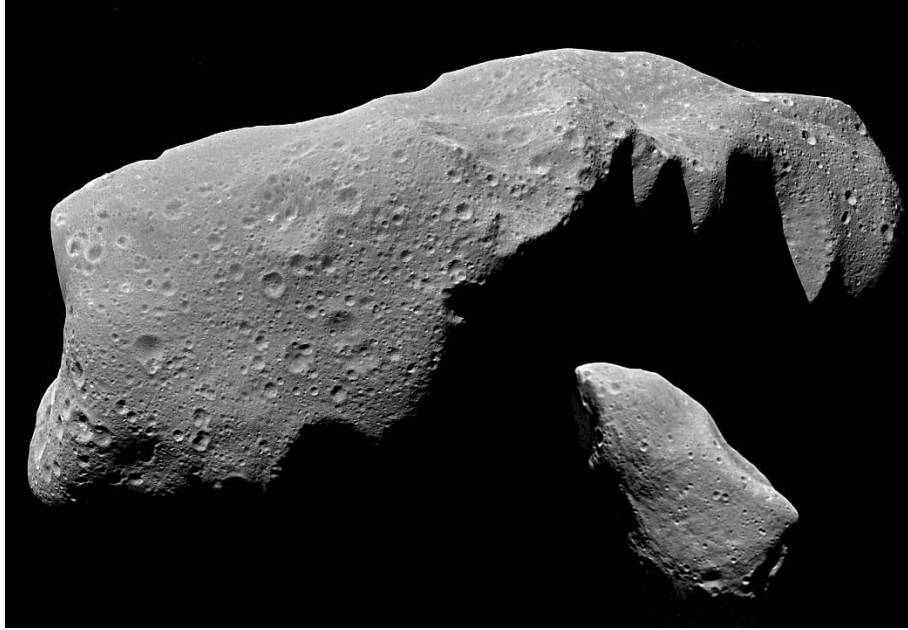


Figure 11. Ida and Gaspra to the same scale. Gaspra (right) was imaged at a range of 5,300 km, and Ida (left) was imaged from 3,000 to 3,800 km, both by the Galileo spacecraft. Gaspra's dimensions are 18.2 km \times 10.5 km \times 8.9 km, and Ida's are 59.8 km \times 25.4 km \times 18.6 km (Belton et al. 1992; 1996). Both bodies are S-type asteroids that are members of asteroid families: Gaspra is part of the Flora family, which may be 1.3 Ga old, and Ida is part of the Koronis family, which is 2–3 Ga old (Bottke et al., 2001; Vokrouhlický et al. 2003; 2017; Brož et al., 2013; Nesvorný et al. 2015; Spoto et al., 2015). Courtesy NASA/JPL/USGS.

2961

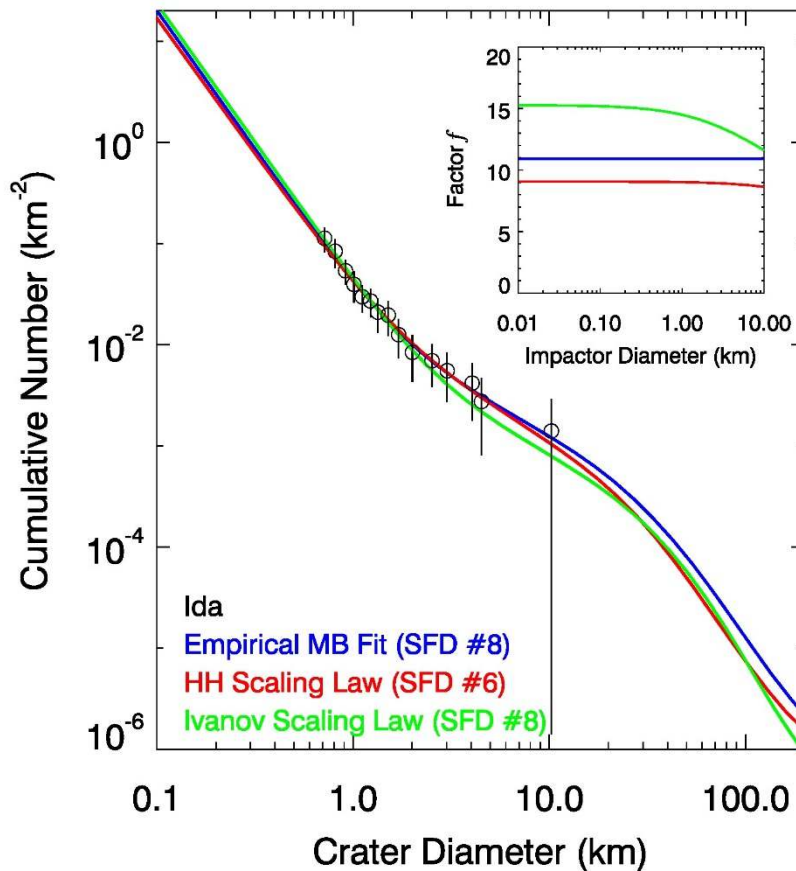


Figure 12. A comparison between the observed crater SFDs found on S-type asteroid Ida, a member of the Koronis family, and various crater models. The observed crater counts are from Fig. 5 of Chapman et al. (1996). Plot components are as in Fig. 4. The best fit model crater SFD is the empirical main belt fit, but both the HH scaling law and the Ivanov scaling law yield comparable fits (Table 3). The empirical main belt fit scaling law and the HH scaling law are our preferred solutions, with the inset showing that both have $f \sim 9-11$.

2962
 2963
 2964
 2965
 2966
 2967
 2968
 2969

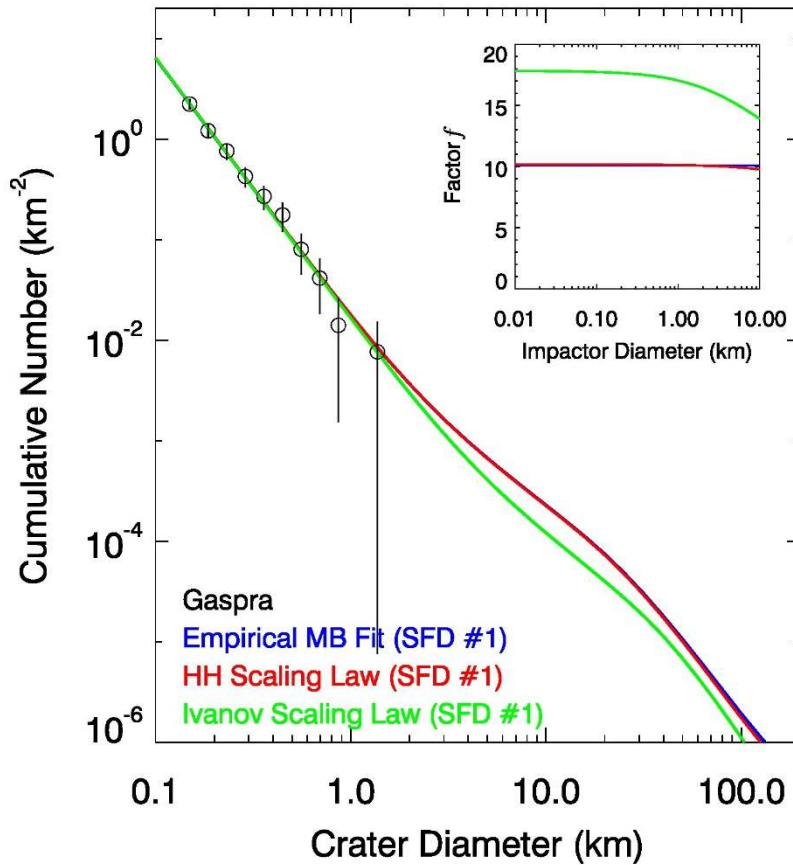


Figure 13. A comparison between the observed crater SFDs found on S-type asteroid Gaspra, a member of the Flora family, and various crater models. The observed crater counts are from Runyon and Barnouin (2015). Plot components are as in Fig. 4. The HH crater scaling law fit in red overlaps the main belt empirical fit in blue. All of our best fit models favor SFD #1 (Table 3), but all yield crater retention ages that are substantially lower than the age constraints from Itokawa samples and our estimated dynamical age of the Flora family. We prefer SFD #5 or #6, which yield results within 1σ of the best fit case, yet yield mean crater retention ages between ~ 1.1 and ~ 1.4 Ga, values that are close to Gaspra's estimated age of 1.35 ± 0.3 Ga from additional constraints (Fig. 18). For these latter runs, our preferred value of f is ~ 10 .

2970
 2971
 2972

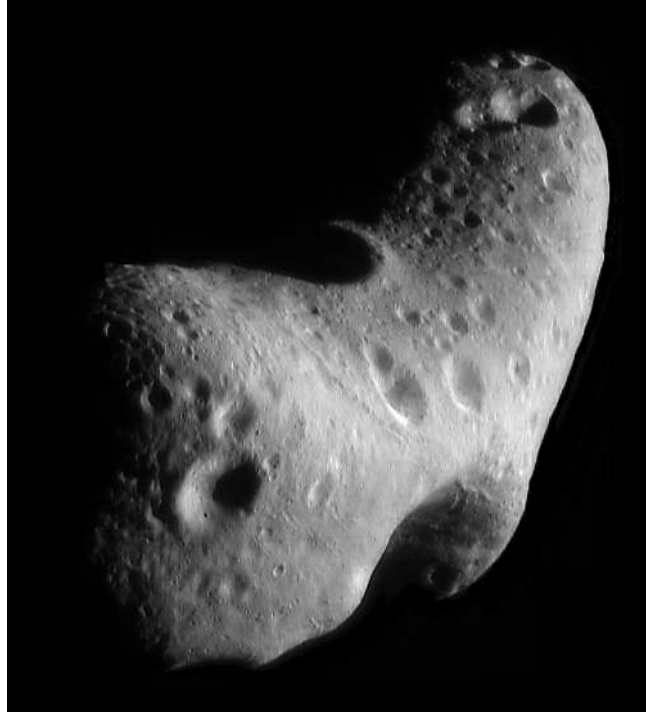


Figure 14. Eros is an S-type near-Earth asteroid. It has dimensions of $34.4 \text{ km} \times 11.2 \text{ km} \times 11.2 \text{ km}$ (Thomas et al. 2002). This view of Eros's northern hemisphere is a mosaic of six NEAR spacecraft images taken from an orbital altitude of about 200 km. Psyche crater (5.3 km across) is located at the 12 o'clock position in the middle of the saddle-shaped region, and Himeros crater (11 km) can be seen on the opposite side of Eros at the 5 o'clock position. Courtesy NASA/JPL/JHUAPL.

2973

2974

2975

2976

2977

2978

2979

2980

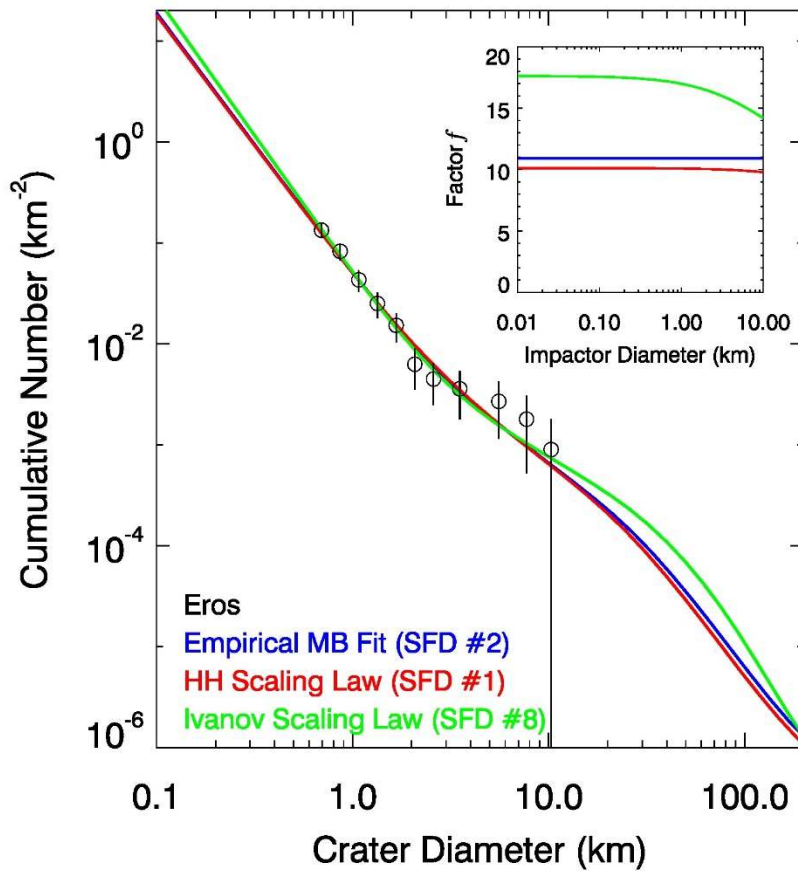


Figure 15. A comparison between the observed crater SFDs found on S-type asteroid Eros, a near-Earth asteroid, and in various crater models. The observed crater counts are from the database of P. Thomas and M. Robinson (Robinson et al. 2002). Craters that are in probable saturation (i.e., those with $D_{\text{crater}} < 0.6$ km) are not shown. Plot components are as in Fig. 4. The HH crater scaling law fit in red largely overlaps the main belt empirical fit in blue. The best fit model crater SFD here is the Ivanov scaling law fit, though all of the fits are fairly comparable (Table 3). See text for discussion of the crater retention age of Eros and possible source families.

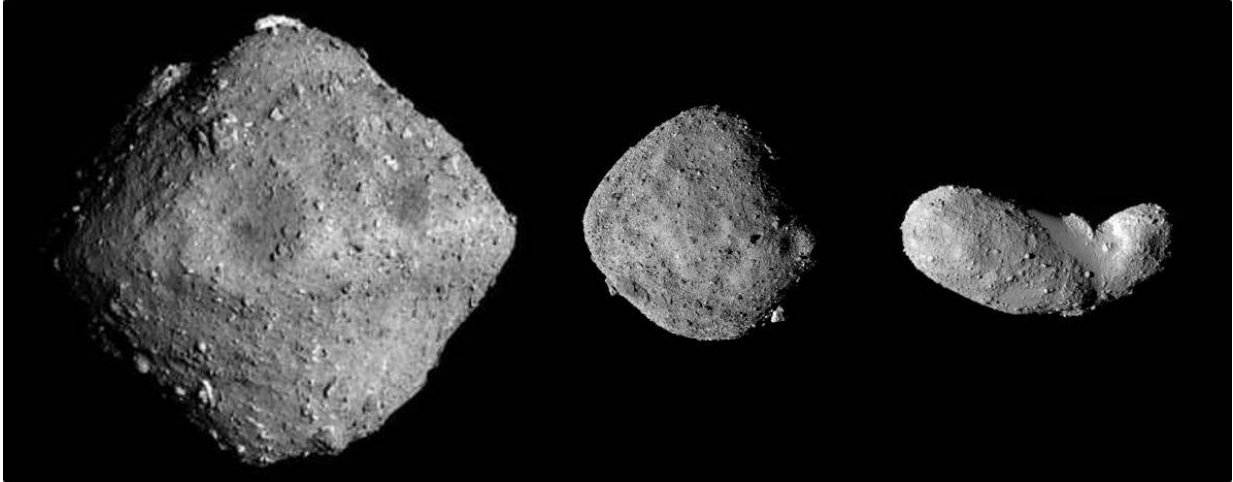


Figure 16. Three near-Earth asteroids observed by spacecraft that are smaller than 1 km. Ryugu (left) is a Cb-type asteroid with a mean diameter of 896 m and a bulk density of $1.19 \pm 0.02 \text{ g cm}^{-3}$ (Watanabe et al., 2019). Its spectral signatures are consistent with thermally and/or shock-metamorphosed carbonaceous chondrite meteorites (Kitazato et al., 2019). Benu (center) is a B-type asteroid with a mean diameter of 492 m and a bulk density of $1.190 \pm 0.013 \text{ g cm}^{-3}$ (Lauretta et al., 2019). Its composition is similar to aqueously altered CM-type carbonaceous chondrites. Itokawa (right) is an S-type asteroid with dimensions of $0.535 \text{ km} \times 0.294 \text{ km} \times 0.209 \text{ km}$ and an estimated bulk density of $1.9 \pm 0.13 \text{ g cm}^{-3}$ (Fujiwara et al., 2006). Grains from Itokawa indicate that it has the composition of an LL-type ordinary chondrite. Images courtesy of NASA/JAXA.

2981
2982
2983
2984

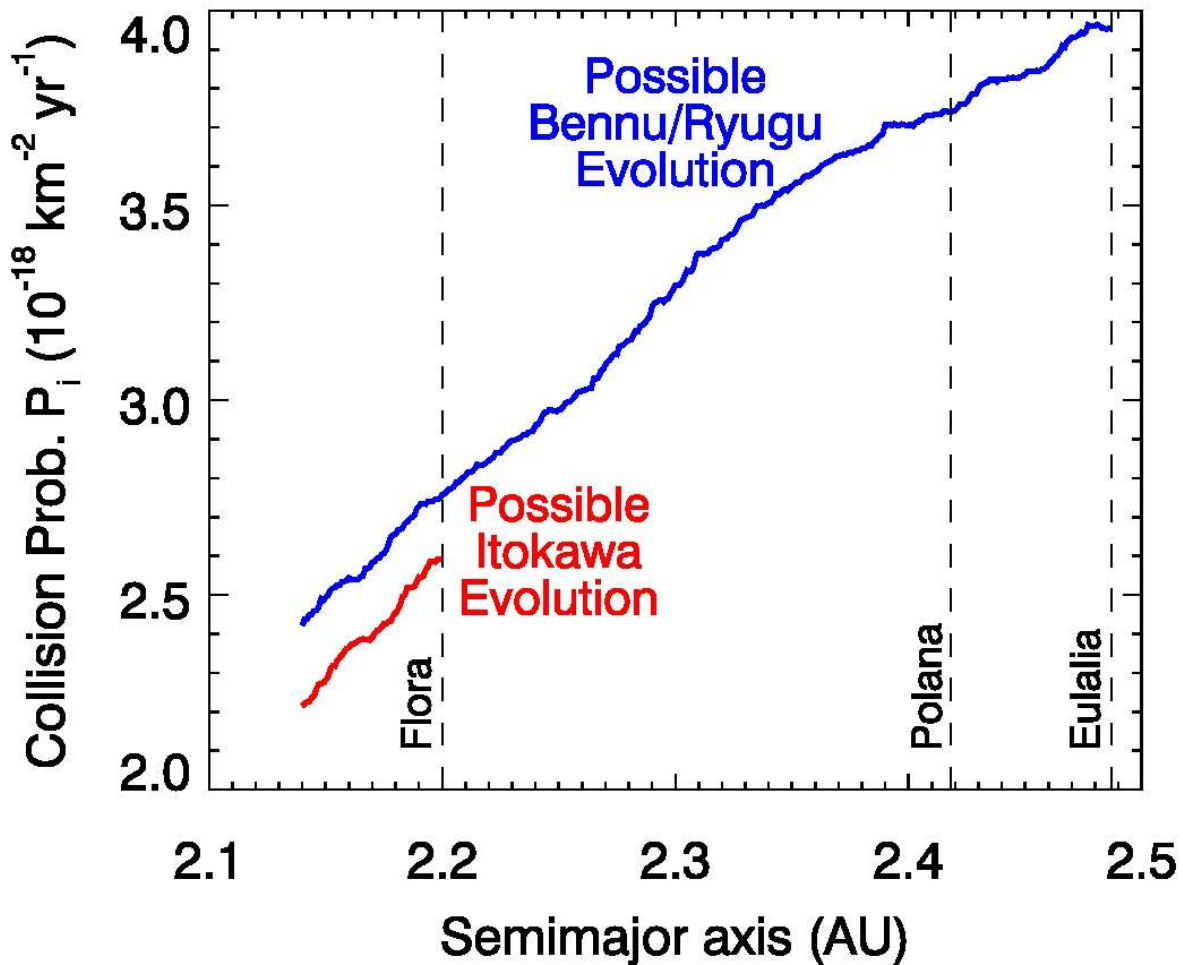


Figure 17. The model collision probabilities of Itokawa, Bennu, and Ryugu as they evolved inward toward the Sun across the main belt by the Yarkovsky effect. For Itokawa (red), we assumed that it started at 2.2 au, the center of the Flora family, and then migrated to 2.14 au where it escaped the main belt via the ν_6 secular resonance. Our Itokawa model asteroids were assigned proper eccentricity and inclination values similar to Gaspra (Table 2). The collision probabilities P_i were calculated with 682 main belt asteroids with $D_{\text{ast}} > 50$ km (Sec. 2.6). The mean values of all red points are $P_i = 2.401 (\pm 0.11) \times 10^{-18} \text{ km}^{-2} \text{ yr}^{-1}$ and $V_{\text{imp}} = 4.98 (\pm 0.04) \text{ km s}^{-1}$. For Bennu and Ryugu (blue), we assumed that they started at 2.487 au and 2.4 au, the centers of the Eulalia and New Polana families, respectively. The model asteroids were given eccentricities and inclinations of 0.1 and 3° , respectively. The rest of the method was same as with Itokawa. The mean P_i value for Bennu and Ryugu starting in the either Eulalia and New Polana families was $(3.3 \pm 0.46) \times 10^{-18} \text{ km}^{-2} \text{ yr}^{-1}$ and $(3.1 \pm 0.39) \times 10^{-18} \text{ km}^{-2} \text{ yr}^{-1}$, respectively, and their mean impact velocities V_{imp} were $4.72 (\pm 0.10) \text{ km s}^{-1}$ and $4.67 (\pm 0.12) \text{ km s}^{-1}$, respectively.

2985

2986

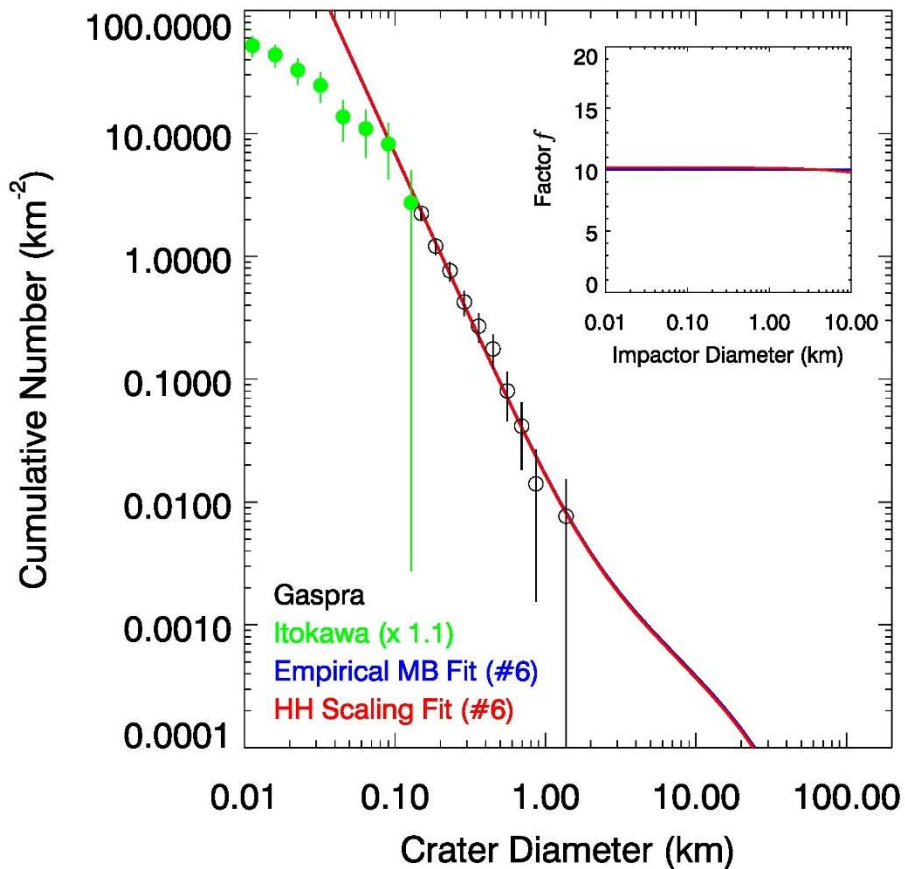


Figure 18. A comparison between craters found on Itokawa and Gaspra and various crater models. Plot components are as in Fig. 4. Gaspra is a member of the Flora family, and its crater counts are the black open circles (Fig. 13). Its estimated crater retention age is ~ 1.3 Ga. Itokawa is currently an NEO, but it was probably a member of the Flora family in the past. Itokawa's crater SFD (Hirata et al., 2009; green dots) has been multiplied by the ratio of the collisional probabilities between Gaspra and Itokawa (Fig. 17 and Sec. 4.1). Within errors, the crater spatial densities of Gaspra and the largest craters on Itokawa appear the same. If the largest craters on Itokawa were made with the same crater scaling law as Gaspra, they could represent the same crater retention age. The smaller craters on Itokawa have been strongly affected by a crater erasure mechanism (e.g., Richardson et al. 2004). The model crater SFDs are discussed in Fig. 13. Here the empirical main belt fit curve (blue line) represents a crater retention age of ~ 1.38 Ga, whereas the HH scaling fit is ~ 1.32 Ga (red line).

2987
 2988
 2989
 2990

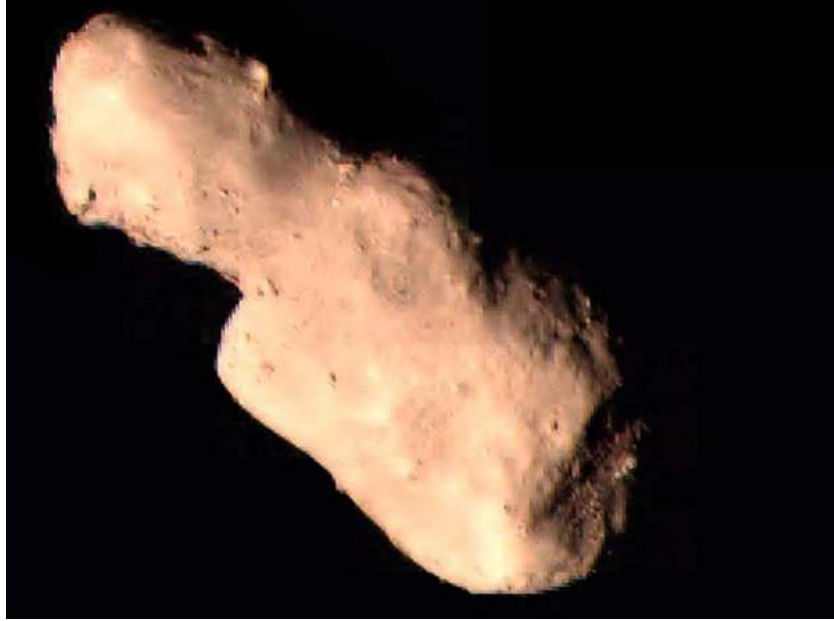


Figure 19. Toutatis is an S-type near-Earth asteroid with dimensions of $4.354 \text{ km} \times 1.835 \text{ km} \times 2.216 \text{ km}$ (Bu et al., 2015; see also Huang et al., 2013). It was imaged by the Chang'e-2 spacecraft during a flyby that had a closest approach distance of 770 ± 120 meters (Huang et al. 2013). Courtesy CNSA.

2991
2992
2993
2994
2995
2996
2997
2998
2999
3000
3001

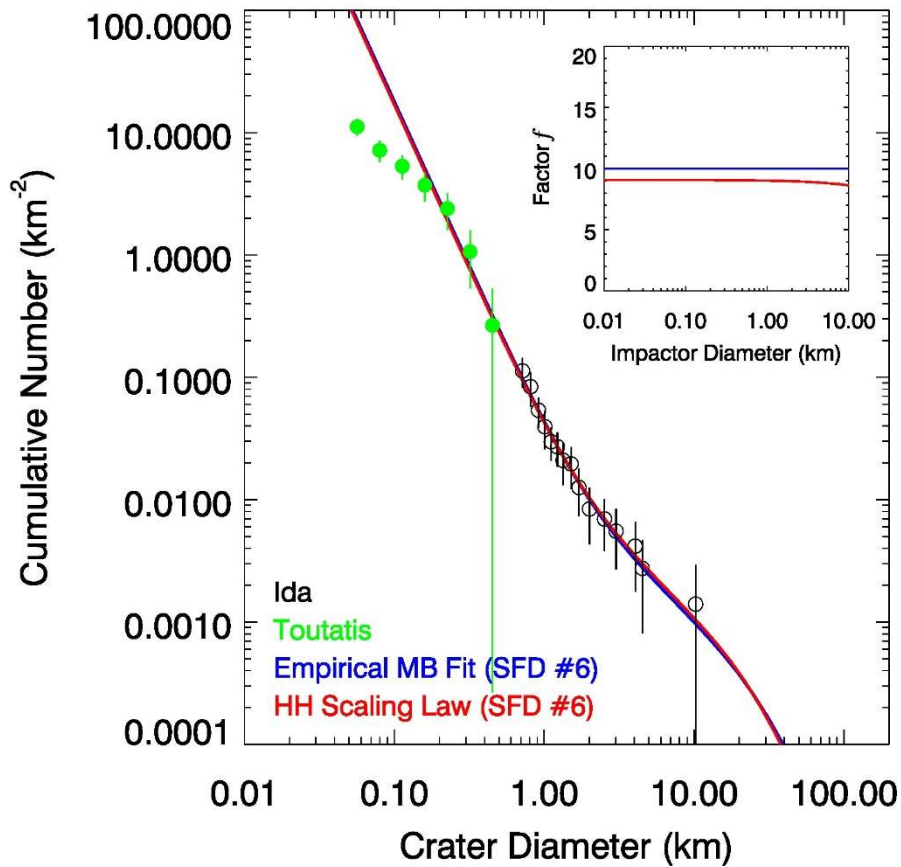


Figure 20. A comparison between craters found on Toutatis and Ida and various crater models. Plot components are as in Fig. 4. Ida is a member of the Koronis family, and its crater counts are the black open circles (Fig. 12). Its estimated crater retention age is ~ 2.5 Ga. Toutatis is currently a NEO, but its orbit and spectral signature can be plausibly linked to the Koronis asteroid family. The largest craters on Toutatis (Huang et al., 2013; Jiang et al., 2015; green circles) are aligned with those of Ida's crater SFD. If the largest craters on Toutatis were made with the same crater scaling law as Ida, they could represent the same crater retention age. The smaller craters on Itokawa have been strongly affected by a crater erasure mechanism (e.g., Marchi et al. 2015). The empirical main belt fit curve (blue line) represents a mean crater retention age of ~ 2.4 Ga, whereas the HH scaling fit is ~ 2.9 Ga (red line).

3002
 3003
 3004
 3005
 3006
 3007
 3008

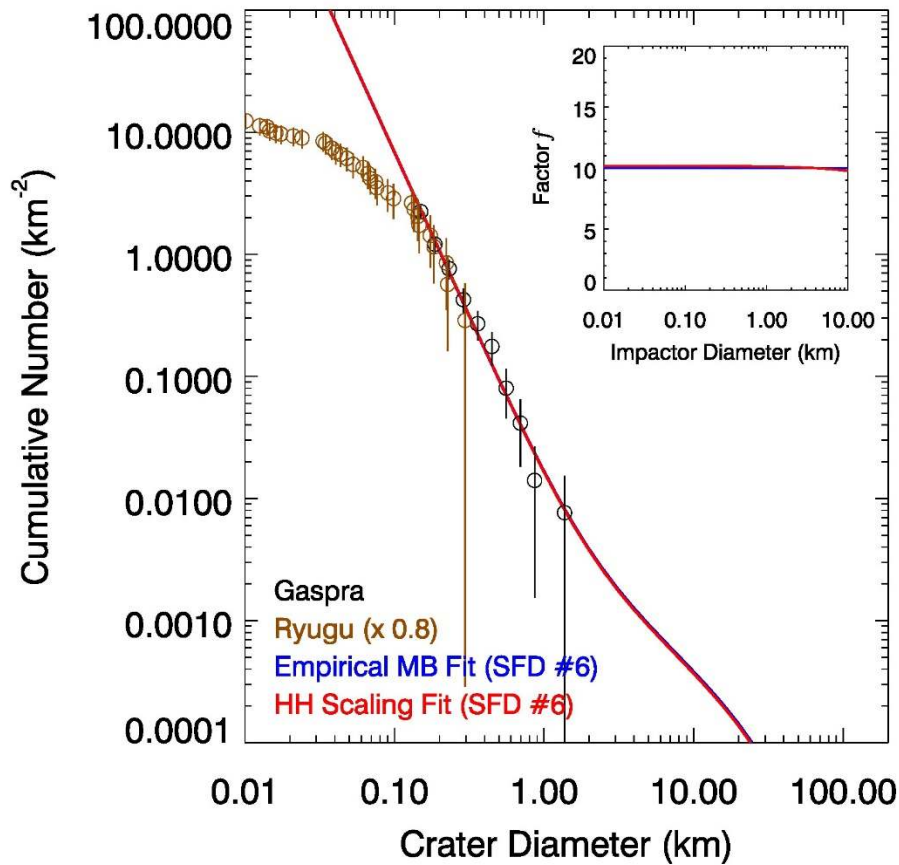


Figure 21. A comparison between craters found on Ryugu and Gaspra and various crater models. Plot components are as in Fig. 4. Gaspra is a member of the Flora family, and its crater counts are the black open circles (Fig. 13). Its estimated crater retention age is ~ 1.3 Ga. Ryugu is currently an NEO, but it is thought to have come from either the New Polana or Eulalia families, with an estimated age of $1.4 [+0.15, -0.15]$ Ga or $0.83 [+0.37, -0.10]$ Ga, respectively (Bottke et al. 2015b). Ryugu’s crater SFD (Sugita et al. 2019) has been multiplied by the ratio of the collisional probabilities between Gaspra and Ryugu (Fig. 17 and Sec. 4.3). Within errors, the crater spatial densities of Gaspra and the largest craters on Ryugu are similar. If the largest craters on Ryugu were made with the same crater scaling law as Gaspra, they could represent a crater retention age near ~ 1.3 Ga. The smaller craters on Ryugu have been strongly affected by a crater erasure mechanism (e.g., Marchi et al. 2015). The model crater SFDs are discussed in Fig. 13 and 18.

3009
3010

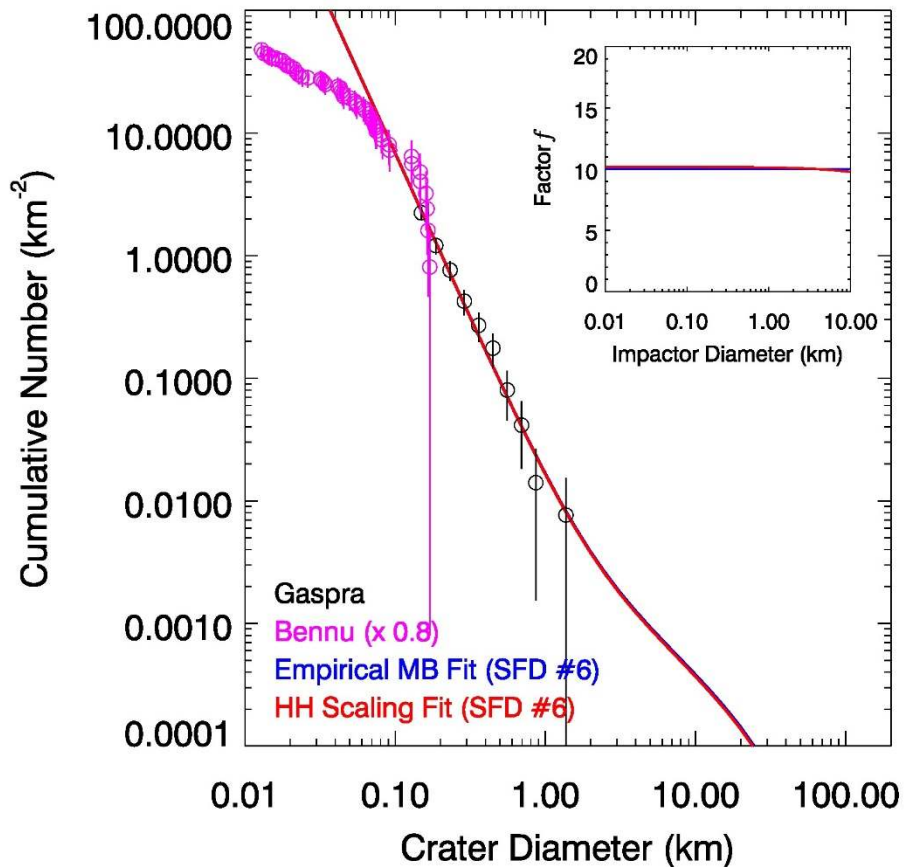


Figure 22. A comparison between craters found on Benu and Gaspra and various crater models. Plot components are as in Fig. 4. Gaspra is a member of the Flora family, and its crater counts are the black open circles (Fig. 13). Its estimated crater retention age is ~ 1.3 Ga. Benu is currently an NEO, but it is thought to have come from the New Polana and Eulalia families, with estimated ages of 1.4 [+0.15, -0.15] Ga and 0.83 [+0.37, -0.10] Ga, respectively (Bottke et al. 2015b). Benu’s crater SFD (Sugita et al. 2019) has been multiplied by the ratio of the collisional probabilities between Gaspra and Benu (Fig. 17 and Sec. 4.3). Within errors, the crater spatial densities of Gaspra and the largest craters on Benu are similar. If the largest craters on Benu were made with the same crater scaling law as Gaspra, they could represent a crater retention age near ~ 1.3 Ga. The smaller craters on Benu have been strongly affected by a crater erasure mechanism (e.g., Marchi et al. 2015). The model crater SFDs are discussed in Fig. 13 and 18.

3011
 3012
 3013
 3014
 3015